Numerical modelling of rigid inclusions foundations subjected to seismic loading

Ramon Alcala-Ochoa

COLLEGE SCIENCES
DOCTORAL DE L'INGENIERIE
PAYS DE LA LOIRE ET DES SYSTEMES

CENTRALE NANTES

MEMOIRE DE DOCTORAT

L'ÉCOLE CENTRALE DE NANTES

ÉCOLE DOCTORALE N° 602
Sciences de l'Ingénierie et des systèmes
Spécialité : *Génie Civil*

Par
Ramon ALCALA-OCHOA

Numerical modelling of rigid inclusions foundations subjected to seismic loading

Projet de recherche doctoral présenté et soutenu à l'École Centrale de Nantes le 5 décembre 2023
Unité de recherche : UMR 6183, Institut de Recherche en Génie Civil et Mécanique (GeM)

Rapporteurs avant soutenance :

Pascal VILLARD	Professeur des Universités - Université Grenoble Alpes
Luc DAVENNE	Professeur des Universités - Université Paris Nanterre

Composition du Jury :

Présidente :	Cristina JOMMI	Full professor	Delft University of Technology / Politecnico Milano
Examinateurs :	Pascal VILLARD	Professeur des Universités	Université Grenoble Alpes
	Luc DAVENNE	Professeur des Universités	Université Paris Nanterre
	Luc THOREL	Directeur de recherche	Université Gustave Eiffel, Campus de Nantes
	Stéphane GRANGE	Professeur des Universités	INSA Lyon
Directeur de recherches doctorales :	Panagiotis KOTRONIS	Professeur des Universités	École Centrale de Nantes
Co-dir de recherches doctorales :	Giulio SCIARRA	Professeur des Universités	École Centrale de Nantes
Co-enc. de recherches doctorales :	Zheng LI	Chargé de recherche	Université Gustave Eiffel, Campus de Nantes

This page intentionally left blank

"And once the storm is over, you won't remember how you made it through, how you managed to survive. You won't even be sure whether the storm is really over. But one thing is certain. When you come out of the storm, you won't be the same person who walked in. That's what this storm's all about."

Haruki Murakami, Kafka on the Shore

This page intentionally left blank

ACKNOWLEDGEMENT

Firstly, I would like to express my gratitude to my thesis director, Panagiotis Kotronis, for agreeing to lead and supervise my PhD. Thank you for your patience and your dedicated passion for the work. I gained invaluable insights from you and hold dear the memories of our meetings over these years. My gratitude extends to Giulio Sciarra for accepting the co-supervision of this thesis. I appreciate your ability to pose challenging questions, contributing significantly to my work. To Zheng Li, thank you for your teachings and kindness. Thanks to you three for all your support, especially during the manuscript redaction.

I would also like to express my sincere appreciation to Cristina Jommi for being the president of the jury. Your kind words at the end of my defence are deeply cherished. I extend my gratitude to Pascal Villard and Luc Davenne for reviewing this thesis and the jury members Luc Thorel and Stephane Grange, who also guided the CSI meetings. Thank you all five for your valuable time, comments and discussions that enhanced the quality of my work.

Thanks to the ANR ASIRIplus_SDS project for funding my thesis. I appreciate the contributions of all project members during our numerous meetings. Special thanks to Amar, Yuxiang, Jesus, Fahd, Jerôme, Cyril, Anne, and Natalie for their thoughtful conversations that offered valuable feedback on my work.

I am also thankful to the CG laboratory at UGE. The validation of the numerical model in this thesis was made possible through the collaboration with the team coordinated by Luc Thorel and Sandra Escoffier. Thanks also to Charbel, Cristian, and the technical staff for allowing me to attend the tests and for providing the data.

To my colleagues and friends at the École Centrale Nantes, I express my sincere gratitude. A special acknowledgement goes to Sid, Alex, Dania, and Ahmad. Andrianna, I am particularly grateful for your help during the initial stages of my thesis. Special mention to Diego, Jinane, and Julieta for welcoming me into their home and allowing me to share precious moments. Thanks to my office friends, Abdallah, Imane and Ranna, for the laughter and shared experiences. I also extend my thanks to the technical support teams of GLiCID and GeM. Particular appreciation goes to Katia for her assistance in administrative matters.

I extend my gratitude to my colleagues at CentraleSupelec and members of the LMPS. I would like to thank Fernando Lopez-Caballero for allowing me to work in the lab for a significant part of my thesis. Thank you for your friendship, support and the meaningful moments we shared. My sincere thanks also go to my friends Filippo (the man), Michalis, Andrea, David, Martin, Denis, Juan Camilo, Julian, Exneyder, Yilun, Cristian, Fanny, and Jacquet. Without you, my doctoral years would not have been as rich and fulfilling.

I express my appreciation to my close friends in Mexico for being a constant source of support despite the distance. Thanks are extended to my Chilean and French family for their support. Thanks to my family in Mexico, who have played a significant role in shaping my character. I am particularly grateful to my parents, Ramon and Sagrario, who have always believed in me, encouraged my academic pursuits, and prioritised my happiness over their own by allowing me to leave home from a young age. Thank you for always waiting for my return and for taking care of Watson. Finally, I would like to thank Valeria, my best friend and life partner, who has been my most important pillar of support since the beginning of my thesis. For a long time in my life, I experienced a sense of homesickness, but I now know that home is wherever we are together. This accomplishment is also yours; thank you for all your love over these years.

Table of Contents

Introduction **21**

1 Literature review on RI foundations **23**
1.1 Introduction . . . 23
1.2 Load transfer mechanisms . . . 26
1.3 Vertical bearing capacity . . . 29
1.4 Soil structure interactions . . . 33
1.5 Seismic performance . . . 35
1.6 Macroelement approach . . . 36
1.7 Failure envelopes . . . 38
1.7.1 Shallow foundations . . . 39
1.7.2 RI foundations . . . 41
1.8 Conclusions . . . 43

2 Validation of the 3D FEM model **45**
2.1 Introduction . . . 45
2.2 Experimental campaign . . . 45
2.2.1 Centrifuge model configuration . . . 45
2.2.2 Soil characteristics . . . 47
2.2.3 Stress state variables in the soil profile . . . 50
2.2.4 Synopsis of the values adopted . . . 53
2.2.5 Quasi-static vertical loading . . . 54
2.2.6 Experimental results . . . 54
2.3 3D FEM model . . . 55
2.3.1 Spatial discretisation and boundary conditions . . . 55
2.3.2 Constitutive models and material parameters . . . 56
2.3.3 Loading procedure . . . 59
2.4 Numerical vs experimental results . . . 59
2.4.1 Footing . . . 59
2.4.2 Rigid inclusions . . . 62
2.5 Conclusions . . . 64

3 Failure envelope of a RI foundation **65**
3.1 Introduction . . . 65
3.2 Numerical procedure to determine the 3D failure envelope . . . 66
3.2.1 Swipe tests . . . 66
3.2.2 Validation of the numerical procedure . . . 67
3.3 Numerical 3D failure envelope . . . 70
3.4 Analytical 3D failure envelope . . . 71
3.5 Comparison with the Eurocode . . . 74
3.6 Failure envelopes for a foundation with and without RI . . . 75
3.7 Influence of the geometry and of the LTP material properties . . . 79
3.8 Synopsis of the proposed analytical formulas . . . 85
3.9 Conclusions . . . 86

4 A macroelement for a RI foundation **87**
4.1 Introduction . . . 87
4.2 Elastic behaviour . . . 89
4.3 Plastic behaviour . . . 90
4.3.1 Failure envelope . . . 90
4.3.2 Loading surfaces . . . 91
4.3.3 Evolution of internal variables . . . 91
4.4 Extension to dynamics . . . 98
4.5 Synopsis . . . 100
4.6 Calibration . . . 101

5 Validation of the macroelement **103**
5.1 Dynamic centrifuge tests . . . 103
5.2 Numerical model . . . 106
5.3 Numerical vs Experimental results . . . 108
5.4 Conclusions . . . 113

Conclusion **115**

Appendices **119**

A Research report, project ASIRIplus, Benchmark No 1 "*Vertical bearing capacity under static loading*" **120**
A.1 Introduction . . . 120

A.2 Methodology . . . 120
A.2.1 Description . . . 120
A.2.2 Geometrical characteristics . . . 121
A.2.3 Spatial discretisation . . . 122
A.2.4 Boundary conditions . . . 123
A.2.5 Loading procedure . . . 123
A.2.6 Material parameters . . . 124
A.3 Results . . . 126
A.3.1 Calibration . . . 126
A.3.2 Configuration A . . . 127
A.3.3 Configuration B . . . 128

B Research report, project ASIRIplus, Benchmark No 2 "*Response*" 130
B.1 Introduction . . . 130
B.2 Loading procedure . . . 130
B.3 Results . . . 131
B.3.1 Phase 1: Vertical loading . . . 131
B.3.2 Phase 2: horizontal loading . . . 132

C Vertical bearing capacity 133

D Settlement efficiency 136

Bibliography 139

List of figures

1.1 Different foundation concepts, based on the ASIRI French national program (IREX, 2012) . . . 24
1.2 Schematic description and components of a rigid inclusions foundation, based on IREX (2012) . . . 25
1.3 Load transfer mechanisms in a RI foundation . . . 27
1.4 Settlements along the depth of a RI foundation, based on Fioravante and Giretti (2010) . . . 28
1.5 Typical configurations of (a) a shallow foundation; (b) a RI foundation; and (c) a pile group foundation, based on IREX (2012) . . . 29
1.6 The MV1 simplified model foundation configurations IREX (2012) . . . 32
1.7 Substructuring as a three-step solution a) Total solution; b) Calculation of the massless foundation's motion; c) Determination of the frequency-dependent stiffness matrix; d) Calculation of the response of the structure supported on the springs. Adopted from Kausel et al. (1978) . . . 35
1.8 Representation of the ME approach . . . 37
1.9 Failure envelope of a shallow foundation in a cohesive soil, adapted from EC8 (EN1998-5, 2004) . . . 40
1.10 Failure envelope of a shallow foundation in cohesionless soil, adapted from EC8 (EN1998-5, 2004) . . . 41
1.11 Cross-section of the failure envelope for a RI foundation, adapted from Pecker (2023) . . . 43

2.1 Centrifuge model of two identical circular shallow foundations without (left) and with RI (right), prototype scale: plane view (a) from the front and (b) from above, (Escoffier et al., 2022) . . . 46
2.2 Particle size distribution curve of Hostun sand and Hostun sand mix used for the centrifuge tests from Baudouin et al. (2008) . . . 48
2.3 Experimental oedometric test results: stress vertical load increment, σ_1, versus void ratio, e, from Escoffier et al. (2022) . . . 49

2.4 Soil profiles (from left to right): water content, w, soil density, γ, effective stress, σ', overconsolidation ratio, OCR, undrained shear strength, s_{u}, and shear wave velocity, V_s . . . 53
2.5 Applied displacement loading histories for shallow foundations with and without RIs . . . 54
2.6 Vertical force vs vertical displacement at the footing: experimental results for the foundation with (blue) and without (red) RI . . . 54
2.7 Finite element mesh and geometry for the foundation (a) without and (b) with RI . . . 55
2.8 Experimental triaxial compression results (dots) and numerical calibration (red lines) (a) deviatoric stress, q, versus axial strain, ε_1 (b) volumetric strain, ε_v, versus axial strain, ε_1. Hostun mix sand with a relative density $I_{\mathrm{d}} = 0.9$, from Baudouin (2010) . . . 56
2.9 Experimental results (dots) and numerical calibration (red lines) of clay. Experimental oedometric test results to stress vertical load increment, σ_a, versus void ratio, e, from Escoffier et al. (2022) . . . 57
2.10 V_s soil profile - comparison of theoretical and numerically adopted values in the FEM model. . . . 58
2.11 Vertical force vs vertical displacement at the footing: experimental and numerical results for the foundation with (blue) and without (red) RI . . . 60
2.12 Vertical displacement field below the RI foundation for a vertical displacement 0.09 m of the footing (1.5% w/B) . . . 60
2.13 Vertical displacement profiles for the inclusion (section 'a−a') and the soil within two RI (section 'b−b') . . . 61
2.14 Vertical stresses in the soil . . . 62
2.15 Vertical stress distribution in the footing (blue) and at the top of the RI (orange) . . . 63
2.16 Numerical (blue) and experimental (orange) axial forces at the top of the central RI versus vertical displacement of the footing . . . 63

3.1 Swipe tests: sign conventions, vertical and horizontal applied displacements, adapted from Butterfield et al. (1997) . . . 66
3.2 The different stages adopted to numerically perform the swipe tests, from Butterfield et al. (1997) . . . 67
3.3 3D FEM model of a shallow circular foundation (without RI) . . . 68

3.4 Normalised failure envelope of a shallow foundation (without RI): comparison between the results of numerically reproduced swipe tests and existing solutions in the literature (a) $v-h$ (b) $v-m$ and (c) $m-h$ loading planes 69

3.5 (a) Vertical displacement-load curve (blue line). Calculation of the maximal bearing capacity, V_0 (red dot), by the tangent intersection method (black lines) Hirany and Kulhawy (1988). (b) Failure mechanism in the normalised $v-h$ plane at (I) maximum vertical bearing capacity, (II) maximum horizontal normalised force and (III) end of the swipe test. The three figures at the top show the distribution of the equivalent strain ε_{eq} (max value showed at 0.03) 70

3.6 Failure envelope of a RI foundation obtained from sixty-two numerical swipe tests. The representation of a cut in the $m-h$ plane is shown in yellow for $v=0.5$ 71

3.7 Representation of the 'Rugby ball shape' in the different normalised planes 72

3.8 Curve fitting of the numerical data using the direct least square fitting of ellipses (Fitzgibbon et al., 1999; Chernov, 2023). Failure envelope obtained from sixty-two numerical swipe tests. The representation of a cut in the $m-h$ plane is shown in yellow for $v=0.5$ 73

3.9 Normalized failure envelope of a RI foundation in $v-m-h$ space. Proposed analytical formula (yellow) and numerical swipe test results (grey dots) . . 73

3.10 comparison between the Eurocode 8 EN1998-5 (2004) existing solutions for a shallow foundation on a cohesionless and cohesive soil, the numerical swipe tests (Eq. 3.3), and Eq. 3.4 for a RI foundation. Results are shown in the normalised failure envelope in the (a) $v-h$ and (b) $v-m$ plane and at $v=0.5$ for the (c) $m-h$ plane 75

3.11 Normalised failure envelopes for a foundation with (grey) and without RI (yellow) 76

3.12 Unnormalised failure envelopes for a foundation with (grey) and without RI (yellow) 77

3.13 Eleven displacement-probe test combinations to describe the $M/B-H$ positive plane for a fixed $V=1000$ kN. Grey and yellow colours represent the foundation with and without RI, respectively. In bold and thin lines, the failure envelope is described by means of swipe tests and displacement-probe tests, respectively. 77

3.14 Failure mechanisms under combined loadings are shown in grey and yellow frames, representing the foundation with and without RI, respectively. They are presented through the equivalent strain, ε_{eq}, with a maximum value of 0.003. 78
3.15 Parametrical numerical study: variation of the coverage area α (red dots), the LTP thickness H_{LTP} (blue dots), the LTP friction angle φ_{LTP} (yellow dots) and combined effects (grey dots) in the (a) H_{LTP} - φ_{LTP} - α; (b) φ_{LTP} - α; (c) H_{LTP} - φ_{LTP}, and (d) H_{LTP} - α planes 81
3.16 Normalised failure envelopes shapes in the $h-m$ plane at v=0.5 varying the (a) coverage area, α, (b) the LTP thickness, H_{LTP}, (c) the LTP friction angle φ_{LTP} and (d) considering combined effects 82
3.17 Unnormalised failure envelope shapes at v=0.5 varying the (a) LTP thickness H_{LTP} and (b) the LTP friction angle φ_{LTP} 83
3.18 Comparison between Eq. 3.5 and the numerical simulations results for: (a) h_0, (b) m_0 and (c) a_0 84

4.1 Generalised forces and generalised displacements at the footing of a RI foundation 88
4.2 Eq. 4.10(exponential relation) and FE results for different normalised vertical forces for a circular RI foundation 92
4.3 Relation between the isotropic and kinematic hardening laws in the $u-h$ and $m-h$ planes for an increasing cyclic horizontal loading (points F_i) (no inclination is considered), modified from Cremer (2001) 94
4.4 Illustration of the tangent rule, modified from Crémer et al. (2001) 96
4.5 Plastic potential g, the loading surface f_c, and the associated normal vectors for a specific loading point F in the $v-h$ plane, modified from Cremer (2001) 97
4.6 The real components of the impedance functions for a circular (diameter B = 6 m) shallow foundation on a homogeneous soil (V_s = 200 m/s and v=0.3) with (continuous lines) and without (non-continuous lines) RI: (a) vertical and (b) horizontal and (c) rotational stiffness. Results are also compared with analytical formulas for shallow foundations (Gazetas, 1983). Calculations are made with the FEM of section 2.3 99

5.1 Schematic representation of the centrifuge model, (Escoffier et al., 2023) . . 103
5.2 Centrifuge model of the dynamic test of RI foundation, prototype scale: plane and front view, adopted from Escoffier et al. (2023) 104

5.3 Experimental results, Landers 0.15g: acceleration (a) at the ground surface, (b) at the top of the structure, (c) settlement vs. moment and (d) moment vs. rotation, (Escoffier et al., 2023) . . . 106

5.4 Illustration of the numerical model . . . 106

5.5 Dynamic stifnesses . . . 107

5.6 Comparison between the ME numerical (blue line) and the experimental results (grey line) from Escoffier et al. (2023). Landers 0.05g (a) horizontal displacement at the top of the structure, (b) rotation vs settlement and (c) rotation vs moment . . . 109

5.7 Comparison between the ME numerical (blue line) and the experimental results (grey line) from Escoffier et al. (2023). Landers 0.15g (a) horizontal displacement at the top of the structure, (b) rotation vs settlement and (c) rotation vs moment . . . 109

5.8 Comparison between the ME numerical (blue line) and the experimental results (grey line) from Escoffier et al. (2023). Landers 0.3g (a) horizontal displacement at the top of the structure, (b) rotation vs settlement and (c) rotation vs moment . . . 110

5.9 Comparison between the ME numerical (blue line) and the experimental results (grey line) from Escoffier et al. (2023). Northridge 0.05g (a) horizontal displacement at the top of the structure, (b) rotation vs settlement and (c) rotation vs moment . . . 110

5.10 Comparison between the ME numerical (blue line) and the experimental results (grey line) from Escoffier et al. (2023). Northridge 0.15g (a) horizontal displacement at the top of the structure, (b) rotation vs settlement and (c) rotation vs moment . . . 111

5.11 Comparison between the ME numerical (blue line) and the experimental results (grey line) from Escoffier et al. (2023). Northridge 0.3g (a) horizontal displacement at the top of the structure, (b) rotation vs settlement and (c) rotation vs moment . . . 111

5.12 Comparison between the ME numerical (blue line) and the experimental results (grey line) from Escoffier et al. (2023) with c_2 and c_3 variation. Rotation vs settlement curves (a) Landers 0.05g (b) Landers 0.15g and (c) Landers 0.3g . . . 112

5.13 Comparison between the ME numerical (blue line) and the experimental results (grey line) from Escoffier et al. (2023) with c_2 and c_3 variation. Rotation vs settlement curves (a) Northridge 0.05g (b) Northridge 0.15g and (c) Northridge 0.3g 112

A.1 Finite element model 121
A.2 Boundary conditions applied to the FE model 123
A.3 Finite element model: loading procedure 123
A.4 Left: Su obtained with correlation Su/Qc=18.5. Right: shear strength to cone resistance correlation for two types of kaolinite - sand mix at 20% and 30% (source ASIRI report 2.07.3.08) 125
A.5 Force on the footing function of the imposed displacement (no RI, footing 2.53 m x 2.53 m). Experimental vs. numerical results 127
A.6 Force on the footing function of the imposed displacement (case A, footing 2.53 m x 2.53 m; a centre-to-centre distance of RI 1.70 m) 127
A.7 Vertical force at the head of the RI function of the imposed displacement (case A, footing 2.53 m x 2.53 m, centre-to-centre distance of RI 1.70 m) . 128
A.8 Force on the footing function of the imposed displacement (case B, footing 2.21 m x 2.21 m, a centre-to-centre distance of RI 1.36 m) 128
A.9 Vertical force at the head of the RI function of the imposed displacement (case B, footing 2.21 m x 2.21 m, a centre-to-centre distance of RI 1.36 m) 129

B.1 Numerical model: loading procedure 130
B.2 Force on the footing function of the imposed displacement. 131
B.3 Vertical force at the head of the RI function of the imposed displacement . 131
B.4 Horizontal force at the head of the RI function of the imposed horizontal displacement 132
B.5 Vertical displacement at the centre of the footing function of the horizontal displacement 132

C.1 Vertical displacement vs vertical force for a foundation with (grey) and without (yellow) RI. The maximal bearing capacity, V_0 (red dots), is calculated using the tangent intersection method Hirany and Kulhawy (1988) (black lines) 133

D.1 Influence of (a) coverage area, φ_{LTP}; (b) LTP thickness,H_{LTP}, and (c) LTP friction angle, φ_{LTP}, on the settlement efficiency, η_s, in the force plane normalised by the maximal vertical force of the model without RI 137

List of Tables

1.1 Shape factors for the bearing capacity of circular, square and strip foundations Van Baars (2014) . . . 30
1.2 Parameters used in Eq. 1.9 . . . 39

2.1 HN5-sand mix main characteristics from Baudouin et al. (2008) . . . 47
2.2 Properties of Speswhite kaolin clay (Khemakhem, 2012) . . . 49
2.3 Properties of Hostun HN31 sand (Benahmed, 2001) . . . 50
2.4 Physical parameters for the different soil layers . . . 53
2.5 Geotechnical parameters for the different soil layers of the finite element model . . . 58

3.1 Parameters of the failure envelopes for a foundation with and without RI . 76
3.2 Parameters and their variations . . . 80
3.3 Fitting parameters of h_0, m_0 and a_0 . . . 85

4.1 Summary of the ME parameters . . . 101
4.2 Calibration of the ME parameters . . . 102

5.1 Signal type and PGA of the sequence's input motions (Escoffier et al., 2023) 105
5.2 Parameters of the macroelement . . . 108

A.1 Parameters used for the elastic materials . . . 124
A.2 Parameters used for the soil elastic materials . . . 126

C.1 Parametric study of the settlement efficiency . . . 137

Notations

A_{RI}	Total surface area of the rigid inclusion's cap
A_{slab}	Total surface area of the foundation
α	Coverage area
B	Diameter of the foundation
β	Kinematic hardening variable
c, d and e, f	Shape in the $v-h$ and $v-m$ plane of the failure envelope
c_{1-3}	Constants related to isotropic vertical variable γ
C_c	Compression index
C_s	Recompression index
C_u	Coefficient of uniformity
C_x	Horizontal damping
C_z	Vertical damping
C_θ	Rotational damping
d	Diameter of the rigid inclusion
δ	Kinematic hardening variable
e	Void ratio
$e_{\max}$	Maximum void ratio
$e_{\min}$	Minimum void ratio
η_s	Settlement (vertical displacement) efficiency
$\underline{\mathbf{F}}$	Generalised force vector
f_c	Loading surface
f_∞	Failure envelope
g	Plastic potential
G	Shear modulus
γ	Isotropic hardening variable
γ_s	Density of the grains
γ_w	Density of water
$\mathrm{H}_{\mathrm{LTP}}$	Load transfer platform thickness
$\mathrm{H}_{\mathrm{slab}}$	Thickness of the foundation
$\underline{\underline{\mathbf{K}}}$	Stiffness matrix
k_x^{el}	Stiffness horizontal
k_θ^{el}	Stiffness rotational
k_z^{el}	Stiffness vertical

κ and ξ	Constants controlling the flow rule
N	Gravity level
λ	Normal consolidation line
ψ	Shape inclination in the $h-m$ plane
q_c	Cone penetration resistance
ρ	Isotropic hardening variable
$\rho_{\mathrm{d,min}}$	Minimum dry density
s_u	Undrained shear strength
$\mathrm{s}_{\mathrm{u_{th}}}$	Theoretical undrained shear strength
σ	Total vertical stress
$\underline{\tau}$	Vector containing the two kinematic variables β and δ
$\underline{\mathbf{u}}$	Generalised displacement vector
V_0	Vertical bearing capacity
w	Water content
w_{L}	Liquid limit
w_{RI}	Vertical displacement of the rigid inclusion
w_{un}	Vertical displacement of the foundation without rigid inclusions

Acronyms

AFNOR	Association Française de Normalisation
ANR	Agence nationale de la recherche
ASIRI	Amélioration des Sols par Inclusions Rigides
CEA	Commissariat à l'énergie atomique et aux énergies alternatives
CPT	Cone Penetration Test
DP	Drucker-Prager
EC	Eurocode
EL	Linear elastic
FEM	Finite Element Method
LHS	Latin Hypercube Sampling
LTP	Load Transfer Platform
MC	Mohr-Coulomb
MCC	Modified Cam-Clay
ME	Macroelement
OCR	Overconsolidation ratio
PRF	Piled-Raft Foundations
RI	Rigid inclusions
SSI	Soil Structure Interaction
UGE	Université Gustave Eiffel

This page intentionally left blank

INTRODUCTION

Background and context

With the increasing demand for structures, it is often necessary to construct on soft ground and, therefore, carefully design a reinforced foundation system. Rigid inclusions (RI) are one of the available soil improvement techniques for structures founded on compressible soils. Apart from the obvious advantages of reducing settlement and improving soil-bearing capacity, proper integration of RI foundations in the design can help reduce the risk of collapse, enhancing the reinforced foundation's overall stability and structural response performance (*i.e.*, under seismic loadings).

This thesis is part of the ANR ASIRIplus-SDS (ANR, 2020), a French national project funded by the ANR[1] and complementing the ASIRI+ National Project[2] (Briançon et al., 2019). Given the seismic context of France, where low to moderate seismic risk exists in different zones of the country, the objectives of the ANR ASIRIplus-SDS are, among others, the development of robust numerical tools for engineers and to provide valuable insights into soil reinforcement by RI in seismic zones through a combination of physical experimentation and advanced numerical analysis in collaboration with academic and industry partners.

In that context, several approaches exist for the dynamic analyses of structures considering soil-structure interaction (SSI) under seismic loadings. Actual practice generally relies on the assumption of linear-elastic behaviour in the soil, overlooking the complex nonlinear interactions developed in a RI foundation. This oversimplification is due to the significant human work (*e.g.,* in terms of mesh preparation and data analysis complexity) and the computational costs of the implementation of a complete SSI model. Hence, until recently, comprehensive analyses of SSI on RI foundations were not frequent. Modern practice, however, in zones prone to seismic loadings, often demands simplified tools accounting for the nonlinear SSI.

1. fr: Agence Nationale de la Recherche, en: National Agency for Research
2. The project is created as the continuation of the ASIRI (2012) project, whose final product was the *Recommendations for the design, construction and control of rigid inclusions ground improvements* (IREX, 2012).

Objective and methodology

The main objective of this thesis is to address these limitations by developing a simplified and fast tool to model RI foundations subjected to static and seismic loadings. For this, a 3D FEM model is first constructed and validated against novel experimental data. Then, the FEM model is used to identify a novel failure envelope for RI foundations. This latter defines the allowable safe space, *i.e.*, the limit forces a foundation can endure under combined loadings. The failure envelope is described using a closed-form analytical formula, and then a novel plasticity-based macroelement (ME) is proposed. In the ME approach, the global behaviour of the foundation and surrounding soil is lumped into a single constitutive equation relating the evolution of generalised forces to displacements. Validation of the new numerical tool is provided, comparing its performance with novel experimental dynamic centrifuge tests.

Outline of the manuscript

Chapter 1 presents an overview of the fundamental concepts - such as load transfer mechanisms, stress distribution, and stiffness modifications - that underpin the behaviour of RI foundations under static and dynamic loadings. The ME concept is introduced, as well as the failure envelope, an essential component for the ME's formulation. Chapter 2 presents a validation of a 3D FEM model against experimental results, used in Chapter 3 to identify the 3D failure envelope of a RI foundation. A parametric study is presented in order to understand the influence of the foundation's geometry and of the material properties, and analytical formulas are introduced. Chapter 4 gives the details of the macroelement formulation and Chapter 5 its validation against novel experimental results of a structure over a soil reinforced by RI.

Chapitre 1

Literature review on RI foundations

This Chapter aims to provide an overview of the state-of-the-art research on the fundamental principles governing the behaviour of rigid inclusion foundations, such as load transfer mechanisms, stress distribution, and stiffness modifications. These aspects are explored to elucidate the inclusions' benefits in reducing the foundation's settlement and improving its bearing capacity. The failure envelopes, also called bearing capacity diagrams, are finally presented as the key ingredient for the development of a macroelement in the subsequent Chapters.

1.1 Introduction

Every human-made structure relies on a *foundation* for its support and structural integrity. The primary role of the foundation is to distribute the supported load while limiting the movements (*e.g.*, horizontal displacements, vertical displacement (settlement) and rotations) to acceptable levels. In addition, the dynamic response of foundations and structural systems under seismic loading is fundamental in geotechnical engineering, as severe ground motions can lead to damage and structural failure.

It is common practice in foundation design to consider using a shallow foundation as a preliminary option (Poulos, 2001). However, designing shallow foundations on soft soils is not always possible. If this approach fails to meet the safety requirements, deep foundations are often adopted that transfer building loads to the earth farther down from the surface using piles.

Recent research has, however, put forth a practical and economically viable alternative approach. Columns are employed within the soft ground while a granular cushion layer is interposed between the columns and the shallow foundation to facilitate the transfer of loads and enhance the foundation's bearing capacity (Briançon et al., 2004; Chevalier et al., 2010; Blanc et al., 2014; Dias and Simon, 2015; Burtin and Racinais, 2016; Briancon et al., 2020; Zhang et al., 2022). This novel foundation concept leading to ground improvement is called *Rigid Inclusions foundation* in the context of the "Amélioration

des Sols par Inclusions Rigides"[1] (ASIRI) national project in France (IREX, 2012).

Rigid inclusions (RI) are stiff elements, often in the form of columns or piles, introduced into the soft soil to improve its mechanical behaviour. Apart from the obvious advantages of reduced settlement, properly integrating RI foundations into the design can help reduce the risk of collapse, enhancing the reinforced shallow foundation's overall stability and the structural seismic response performance. In numerous scenarios, RI foundations have emerged as a more efficient and cost-effective alternative to traditional connected pile foundations (Mayoral et al., 2006; Hatem, 2009; Diaz-Guzman et al., 2021; López-Jiménez, 2019).

With the increasing demand for structures, it is often necessary to construct on soft ground and, therefore, to use soil-reinforcement techniques that aim to improve the soil's mechanical properties and the overall site response. The site response can be analysed by assessing the stability of the soil-foundation system under different loading conditions, its bearing capacity and the corresponding settlement.

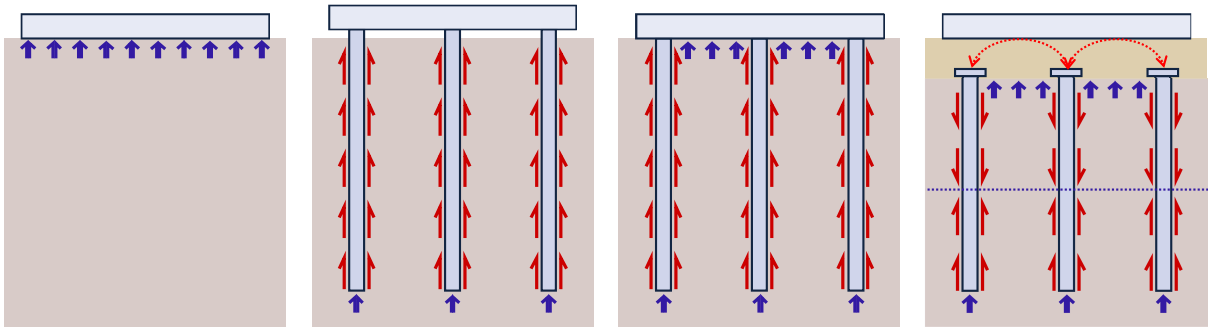

FIGURE 1.1 : Different foundation concepts, based on the ASIRI French national program (IREX, 2012)

One of the available solutions to increase the foundation's bearing capacity and to decrease its settlement is to use piles beneath the shallow foundation (*Piled-Raft Foundations* (PRF), see Fig. 1.1). In this case, the piles contribute as structural elements to transfer the imposed load from the structure to the surrounding soil. However, PRF develops high shear forces and moments at the connection of the piles with the shallow foundation (the pile head), large strains for vertical loading (Sawwaf, 2010; Malekkhani and Bazaz, 2021, among others), and the situation can be aggravated where lateral loads are expected, like seismic loading (López-Jiménez, 2019).

An alternative system that avoids the problem above is to consider the piles disconnected to the foundation (Chevalier et al., 2010; Okyay et al., 2014; Briancon et al., 2020).

1. Soil improvement by rigid inclusions

In the case of RI foundations, the piles are mainly used for soil reinforcement and not as structural members that transfer the building loads, see Fig. 1.1. In that way, piles act as stiffeners of the composite soil mass, consequently reducing the settlement (Cao et al., 2004). While the raft can rest directly on the top of the piles, a soil cushion is usually introduced between the piles and the shallow foundation.

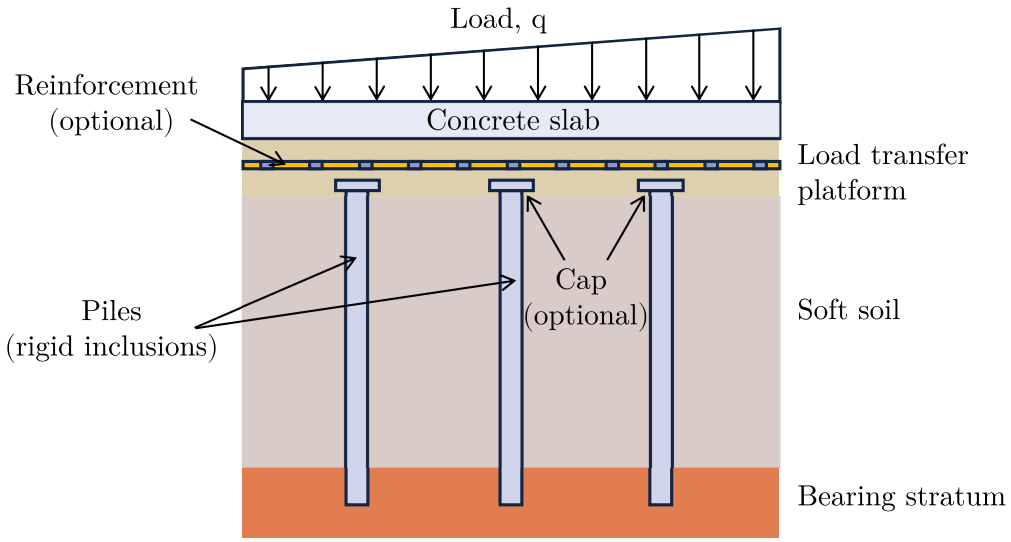

FIGURE 1.2 : Schematic description and components of a rigid inclusions foundation, based on IREX (2012)

RI foundations can be divided into several main components (IREX, 2012; Larisch et al., 2015), Fig. 1.2:

(i) a concrete slab (footing) employed to transmit the structural loads onto the load transfer platform, similar to the concept of shallow foundations;

(ii) a Load Transfer Platform (LTP), disposed over the soft soil and the rigid inclusions. It is a layer composed of granular materials, usually sand or gravel.It plays an essential role in mobilising the soil-bearing capacity and modifying the load transfer mechanism (Liang et al., 2003). This layer can be reinforced by geosynthetic materials such as geogrid or geo-synthetic sheet (Chevalier et al., 2010). Besides allowing the disconnection between the footing and the RI, the LTP layer serves as a dissipation energy zone and changes the load-settlement behaviour due to different constraint conditions at the foundation-soil interface (Fioravante and Giretti, 2010);

(iii) rigid inclusions (piles, with the possibility of having caps at the top) that stiffen the soil and transfer the vertical loads to deeper, more stable soil layers. Their presence

reduces the foundation settlement, ensuring stability in areas with compressible soil (Briançon et al., 2004). While they can be made by metal (steel or aluminium) or timber (Wang et al., 2019; Ikbarieh et al., 2023), they are often constructed using reinforced or unreinforced concrete (Jenck et al., 2005; Le Hello and Villard, 2009; Briançon et al., 2015; Tradigo et al., 2015; Pham et al., 2019; Acar and Mollamahmutoglu, 2023, among others);

(iv) a soft soil layer that experiences settlement;

(v) a bearing stratum that ensures the load transfer into the firmer ground through the column base and shaft friction, specifically below the point where settlements are equal.

Since the RI are not connected to the footing, RI foundations present environmental (*e.g.*, compared to excavation solutions), economical (*e.g.*, compared to bearing and friction piles, pile-raft foundations) and time-saving (*e.g.*, compared to draining piles, preloading) advantages. The technique has been used worldwide for embankments, wind turbine foundations (Neagoe, 2013), bridges piles (Combault et al., 2005; Fok et al., 2012), high-speed lines (Burtin and Racinais, 2016), tanks (Buschmeier et al., 2012; Hamidi et al., 2016; Bernuy et al., 2018) and coastal structures (Le Cor et al., 2022; Jawad et al., 2022), among others.

1.2 Load transfer mechanisms

The load transfer mechanisms in a RI foundation are schematically represented in Fig. 1.3. The vertical load from the structure is transmitted to the footing and distributed along the LTP to both the head of the inclusions and the soft ground layer to stiffer soil layers. The transmission is achieved by the combination of two mechanisms: (i) arching in the LTP and (ii) frictional interaction between the inclusions and the soil (Filz et al., 2019).

Typically, when the concrete slab (footing) transmits vertical loads to the LTP, the weight is initially evenly distributed. With increasing loading, however, the soil particles rearrange themselves, leading to a stress redistribution. The soil directly beneath the footing experiences higher compressive stresses, while the soil around the RI experiences lower stresses. This redistribution occurs because soil particles reposition themselves, filling the voids between the piles and effectively redistributing the load from the piles to the adjacent soil layers (Low et al., 1994; Lai et al., 2018).

Since the inclusions and the soil have different stiffnesses, a differential settlement happens, leading to the so-called *arching effect*. This pressure transfer, introduced by Terzaghi (1943a), generates a state of stresses in the zone of arching as a combination of vertical stresses and lateral arching forces. In the case of a RI foundation, the arching effect is mainly developed in the LTP layer, as represented in Fig. 1.3.

The arching effect concentrates vertical stresses beneath and around each RI, forming the *zone of influence* or *arching zone*. This phenomenon redistributes part of the load to horizontal stresses, reducing the vertical stress transferred through the piles (Wang et al., 2019). As a result, RI provide lateral confinement to the soil (see also Tradigo et al., 2015; Amalu and Jayalekshmi, 2022, among others). Consequently, these mechanisms allow for better resistance against lateral movements and promote stability in the RI foundation (Jenck et al., 2005; Filz et al., 2019).

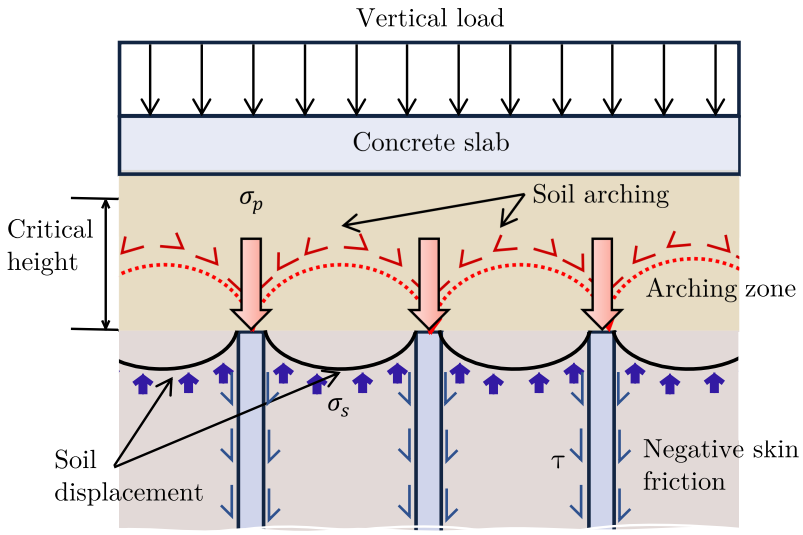

FIGURE 1.3 : Load transfer mechanisms in a RI foundation

Several authors agree on the definition of a *critical height*, above which the differential settlements along the ground surface are no longer measurable. If the LTP thickness exceeds this critical height, it allows for complete arching, ensuring efficient load distribution. The critical LTP height is dependent on the RI spacing and width (Jenck et al., 2005; Simon, 2012; Filz et al., 2012; da Fagundes et al., 2017; Lai et al., 2018, among others).

The shift from negative to positive skin friction marks the establishment of a *neutral plane* (equal settlement plane). This mechanism is primarily influenced by LTP thickness and stiffness, as well as the soft layer stiffness (Fioravante and Giretti, 2010; Tradigo

et al., 2015). The LTP enables downward soft soil-RI displacements, creating negative *skin friction* on the upper shaft of the RI.

In Fig. 1.4, the (positive) settlements are defined hereafter for the footing centre w_{RI}, of the RI (pile) w_{p} and of the soil along the RI-soil interface w_{s}. At the pile head, we can qualitatively observe that $w_{\mathrm{RI}} \geq w_{\mathrm{s}} > w_{\mathrm{p}}$, which explains the occurrence of the mentioned differential soil-RI displacements and, consequently, negative skin friction effects. Conversely, along the lower section of the pile, we have $w_{\mathrm{p}} > w_{\mathrm{s}}$, resulting in the development of positive skin friction up to the pile base.

Positive and negative skin frictions influence the axial force distribution along the pile. The axial force distribution can be determined using the following equilibrium considerations:

$$N(z_2) - N(z_1) = \pi D \int_{z_1}^{z_2} \tau(z)\, dz \tag{1.1}$$

where τ is the average shear stress on the pile perimeter at a given depth z. Usually, the maximum axial force N_{max} is reached at the neutral plane.

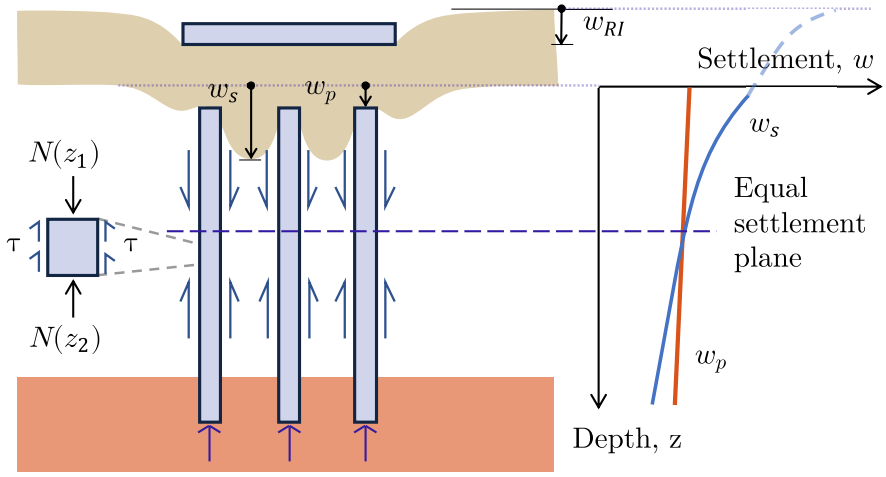

FIGURE 1.4 : Settlements along the depth of a RI foundation, based on Fioravante and Giretti (2010)

The aforementioned transfer mechanisms involve the vertical stress distribution to stiffer soil layers through the LTP and inclusions. Besides, these mechanisms facilitate the redistribution of vertical to horizontal stresses, reducing the vertical stress transferred through the piles. The differential soil-RI displacement in the space between RI also shows the apparition of negative and positive skin friction around the RI shaft. As a consequence, the soil load-bearing capacity is significantly increased. Therefore, in the initial design step of RI foundations, understanding these transfer mechanisms is essential as they play a

key role in estimating the vertical bearing capacity.

1.3 Vertical bearing capacity

Typical configurations of a shallow, a RI and a pile group foundation are shown in Fig. 1.5.

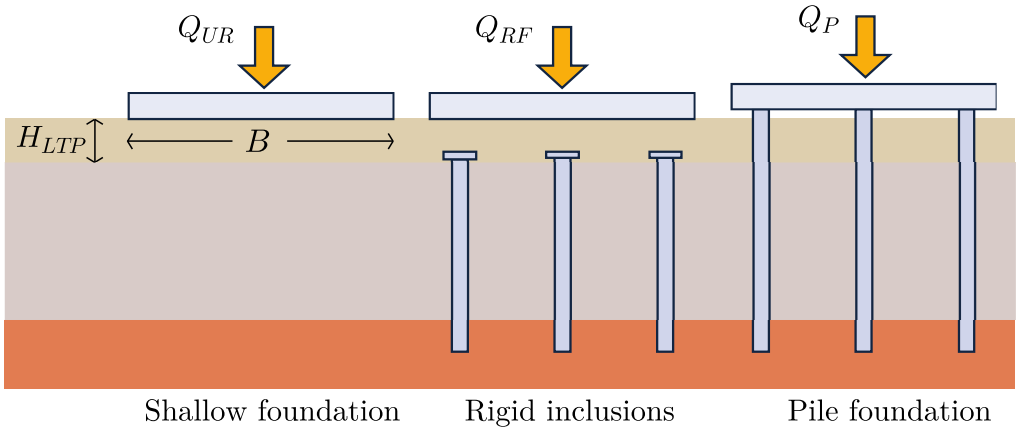

FIGURE 1.5 : Typical configurations of (a) a shallow foundation; (b) a RI foundation; and (c) a pile group foundation, based on IREX (2012)

The contribution Q_{RF} to the vertical bearing capacity of the (reinforced[2]) RI foundation is defined hereafter. Q_{UR} the vertical bearing capacity of the (un-reinforced) shallow foundation and Q_{P} the vertical bearing capacity of the pile foundation. Following the French ASIRI recommendations (IREX, 2012), the RI foundation bearing capacity under a centred vertical load is composed of the contribution of each component:

$$Q_{\mathrm{RF}} = Q_{\mathrm{UR}} + Q_{\mathrm{P}} \tag{1.2}$$

In terms of the load capacities of shallow foundations (Q_{SF}) and piles (Q_{SF}), Eq. 1.2 is modified as follows:

$$\begin{aligned} Q_{\mathrm{RF}} &= \beta_{\mathrm{SF}} \cdot Q_{\mathrm{SF}} + \beta_{\mathrm{P}} \cdot Q_{\mathrm{pg}} \\ &= \beta_{\mathrm{SF}} \cdot Q_{\mathrm{SF}} + \beta_{\mathrm{P}} \cdot (G_{\mathrm{e}} \cdot n \cdot Q_{\mathrm{sp}}) \end{aligned} \tag{1.3}$$

where β_{SF} and β_{P} are the efficiency factors for shallow foundations and piles; Q_{pg} is the pile group load capacity; G_{e} is the group efficiency, adopted from the conventional pile design (*e.g.*, NF P 94-262; AFNOR, 2013b); n is the number of piles; and Q_{sp} is a single

2. The term "reinforced" here is used to indicate ground improvement due to the use of inclusions; it does not refer to the existence or not of reinforcement steel bars in the concrete.

pile load capacity. In Eq. 1.3 the parameter β_{SF} varies within the interval of 0 to 1. It means the shift from the failure of a shallow foundation ($\beta_{\mathrm{SF}} = 1$ and $\beta_{\mathrm{P}} = 0$) to the failure of a reinforced foundation, primarily attributed to the pile's failure ($\beta_{\mathrm{SF}} = 0$ and $\beta_{\mathrm{P}} = 1$). Under the framework of soil mechanics, established by the works of Terzaghi (1943b), the vertical bearing capacity of the shallow foundation (Q_{SF}) relies on the soil's capacity to resist external forces. This resistance is characterised by its failure criterion, defined by the soil's cohesion parameters (c) and friction angle (φ). These values are determined by superimposing three limit loads, accounting for a purely frictional and cohesive weightless soil, as well as the surcharge term:

$$Q_{\mathrm{SF}} = \underbrace{\frac{s_\gamma}{2}\gamma B N_\gamma}_{\text{Density term}} + \underbrace{s_c c N_c}_{\text{Cohesion term}} + \underbrace{(q0 + \gamma D) N_q}_{\text{Surcharge term}} \tag{1.4}$$

where B is the footing width; s_γ and s_{c} are the shape factors given in Tab. 1.1; γ is the unit weight of the soil; N_γ, N_{c} and N_{q} are the bearing capacity factors depending on the internal friction angle φ of the soil; $q0$ is the surcharge lateral to the foundation and D is the height of the depth of embedment.

TABLE 1.1 : Shape factors for the bearing capacity of circular, square and strip foundations Van Baars (2014)

	Circular	Square	Strip
s_γ	0.6	0.8	1
s_{c}	1.3	1.2	1

- In cohesion-less soils, the long-term design is carried out using the drained strength parameters $c = c'$ and $\gamma = \gamma'$ corresponding to drained conditions in effective stresses. N_{q} and N_{c} capacity factors, defined by the Prandtl (1920) solution, have an exact analytical expression (Prandtl, 1920; Terzaghi, 1943b; Skempton, 1948; Meyerhof, 1953):

  As for the N_γ coefficient, it has no exact analytical expression (Taylor, 1948). Numerous approaches have been formulated to estimate it based on theories encompassing diverse variables to define a more accurate failure mechanism for the interaction between the footing and the soil system (Diaz-Segura, 2013). For example, solutions proposed in small-scale foundation experiments by (Terzaghi, 1943b; Meyerhof, 1953; Hansen, 1970; Vesic, 1973). French norm NF P 94-261 (AFNOR, 2013a) recommends the following expression:

$$N_\gamma = 2(N_q - 1)\tan\varphi \tag{1.5}$$

- In the case of undrained conditions with saturated purely cohesive soils, a short-term design approach is employed with $c = c_u$ and $\varphi = 0$. While the N_c coefficient is calculated as:

$$\begin{aligned} N_c &= \pi + 2 \quad \text{for a smooth foundation} \\ N_c &= 5.71 \quad \text{a rough foundation} \end{aligned} \tag{1.6}$$

  Experimental investigations conducted on square raft models situated on clay soils indicate that the bearing capacity of a shallow foundation can be established by the load level where settlement is equal to 10 % of the raft width (Cooke, 1986; Borel, 2001).

The vertical bearing capacity is estimated, for example, by analytical calculations (*e.g.*, MV1 method) as indicated in ASIRI recommendations (IREX, 2012). In the MV1 method, based on the studies of Combarieu (1990), β_{SF} and β_P in Eq. 1.3 can be determined as a function of H_{LTP}, the LTP thickness:

$$\begin{aligned} &\text{being} \quad \Omega = \frac{1}{4}(2 - \frac{2 \cdot H_{LTP}}{B})^2 \\ &\text{if} \qquad H_{LTP} < B, \qquad \beta_{SF} = (1 - \Omega) \quad \beta_P = \Omega \\ &\qquad\quad H_{LTP} > B, \qquad \beta_{SF} = 1 \qquad\quad \beta_P = 0 \end{aligned} \tag{1.7}$$

where Ω represents a platform factor that considers the height of the LTP, and B is the footing width. Expressions in Eq. 1.7 admit the assumption that the influence between the different components of the limit load is exclusively related to the efficiency developed by the LTP and controlled by its thickness H_{LTP}. The outcomes derived through this analytical approach align with experimental results (Plumelle, 1985; Bigot and Canepa, 1988).

According to Fig. 1.6, the value β_{SF} [3] varies in the range of 0 and 1, indicating the contribution of the RI to the maximal vertical load capacity. The β_{SF} factor decreases exponentially as H_{LTP} increases. As stated before, this assumption may be related to the loss of efficiency in the LTP layer (Combarieu, 1990).

When the thickness of the platform increases, becoming higher than the width of the footing B, the contribution of the piles is neglected. This case is not cost-effective.

3. Curves have been obtained by Eq. 1.7

Besides, the decision to reinforce the soil is often taken when it is impossible to justify the footing regarding soil-bearing capacity. Likewise, for small H_{LTP} values, the maximal bearing capacity calculation considers the shallow foundation's contribution but reduces the pile group's contribution.

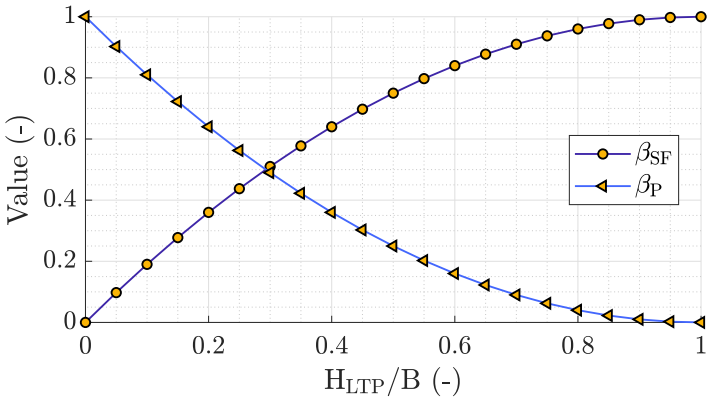

FIGURE 1.6 : The MV1 simplified model foundation configurations IREX (2012)

Furthermore, when no LTP is present, Eq. 1.7 considers that the failure load of a RI foundation is equivalent to that of a pile group alone, $\beta_{SF} = 0$ and $\beta_P = 1$. This assumption is overly conservative based on the experimental data collected by Mandolini et al. (2013). In this case, $H_{LTP} = 0$, the design of this foundation is similar to the PRF, as both systems recognise the combined behaviour of the shallow foundation and piles.

In PRF, load capacity factor may be considered $\beta_P = 1$ in undrained clays (Liu et al., 1985; Poulos, 2000; de Sanctis and Mandolini, 2006; Lee et al., 2014, among others). However, β_P may differ due to alterations in the soil's confining stress for a scenario involving sands or drained clays. These changes subsequently impact the shaft resistances of the piles and introduce an interaction effect between the raft and piles (Liu et al., 1985; Long, 1993; Katzenbach et al., 2000). While β_{SF} calculation in PRF for clayey soils can be established between the footing and pile geometry as follows (de Sanctis and Mandolini, 2006):

$$\beta_{SF} = 1 - 3\frac{d \cdot \alpha}{s} \tag{1.8}$$

where d is the pile diameter; α is the coverage area ratio, calculated as the total surface area of the piles' cap over the total foundation top surface, and s is the centre-to-centre pile distance.

In the MV1 method, it becomes evident that several behaviour mechanisms are unaccounted for. These mechanisms, comparable to those studied in PRF foundations, require

a more comprehensive exploration. More complex methodologies for designing RI foundations are presented in IREX (2012) for vertical loading (*e.g.*, MV2 et MV3), founded principally on the equilibrium of external loads imposed by the structure and the resistance offered by the RI within the ground. For more details, Larisch et al. (2015) presents the design methodologies for two case studies of RI projects using these approaches.

Design offices rely on the vertical bearing capacity to determine the permissible forces a RI foundation can withstand. Nevertheless, understanding the behaviour of such foundations to seismic loadings is essential for ensuring an efficient and secure design.

1.4 Soil structure interactions

Buildings and geo-structures have direct contact with the soil. When external dynamic forces like earthquakes act upon these structures, there is a mutual influence between the structural and ground responses. After the 1964 Niigata earthquake (Mw 7.5) in Japan, it became evident that the behaviour of the structure does not solely determine the extent of structural damage. Instead, the characteristics of the soil beneath the structures also played a crucial role, as pointed out by Ohsaki (1966). A similar scenario was observed during the 1985 Michoacan earthquake (Mw 8.1) in Mexico. The damaged structures were exposed to multiple cycles of large dynamic forces at periods near their fundamental frequencies due to Soil-Structure Interactions (SSI) effects (Sánchez-Sesma et al., 1988; Ohmachi et al., 1988).

When a structure is subjected to an earthquake motion on relatively soft soil, two phenomena have to be considered: *kinematic* and *inertial* interactions. In the case of a structure with a RI foundation, the first phenomenon arises due to the difference in stiffness between the RI and the soil. Compared to free field propagation, the waves are modified and scattered due to the presence of RI that acts as “reinforcement”, improving the ground behaviour. They can lead to a decrease in the average distortion within the reinforced soil volume (Javelaud and Serratrice, 2018). Inertia interactions occur because of the vibrating structure that can increase the base shear and overturning moment at the foundation level, causing additional deformation in the soil. This deformation in the underlying soil provides more flexibility to the system and further modifies the base motion (Kramer, 1996).

SSI characterises the interactions among the soil, the foundation, the structure and the applied ground motion. Traditionally, SSI has been perceived beneficial for the structural response (Veletsos and Verbic, 1974; Ghannad and Ahmadnia, 2006; Jeremić and Presig, 2005; Khosravikia et al., 2018) and thus often neglected in various seismic guidelines (Jie

et al., 2007). This tendency mainly arises from the observation that structures founded on soil have longer fundamental periods, which, following the typical form of the design codes spectra, leads to a reduction of the acceleration and inertia forces (Mylonakis and Gazetas, 2000; Pitilakis et al., 2008).

It is common in practice to design the structures considered fixed at the base. This assumption is, however, overly simplified as the spectra of real earthquakes do not have smooth shapes; an increase of the spectral acceleration and the inertial forces is therefore possible. Furthermore, SSI often results in higher structural displacements. SSI may, therefore, have a beneficial or detrimental effect on the structural response depending on the context (Mylonakis and Gazetas, 2000; Pitilakis et al., 2008). EC8 (EN1998-5, 2004) does not call for SSI analysis except when likely to cause detrimental effects (significant displacement increase, impact of the foundation on the input motion). For instance, in the case of structures where second-order effects are important, *i.e.*, structures with massive or deep-seated foundations, slender or tall structures, structures supported on very soft soils or structures with pile foundations.

The importance of SSI analyses increased as authorities aim to implement Performance Based Design (PBD) concepts within the engineering community (Anastasopoulos et al., 2012; Pecker et al., 2014; Correia and Pecker, 2021). A robust numerical SSI model can prevent structural damage or collapse and lead to cost savings by optimising the design to withstand seismic events. In the following, a general overview of the main approaches is presented:

- **Substructuring**
  Based on the superposition principle, the substructure approach considers the soil and structure as separate components (Kausel et al., 1978; Kramer, 1996), see Fig. 1.7. The kinematic and inertial interactions are first studied separately, using transfer functions and dynamic impedance matrices. The contributions of both phenomena are then combined to obtain the total displacements. By adopting this approach, the size of the problem and the computational time are significantly reduced, compared to the direct method (Hashemi et al., 2014). The main limitation of the substructure method lies in the linearity assumption, making it unsuitable for nonlinear problems (Pecker, 2023).

- **Direct numerical modelling**
  Direct methods consider the SSI system as a single integrated system; both the structure and the soil are discretised in the numerical model. This approach offers the highest level of generality, as it can account for all nonlinear behaviours of the

structure, soil, and their interface, including sliding and uplift (Jeremic et al., 2023).

- **Macroelement approach**
  The macroelement concept (Nova and Montrasio, 1991) can be seen as a 3D stress-resultant "constitutive law", linking the generalised forces with the generalised displacements (Li et al., 2015), reproducing the key characteristics at the *structural* level. This simplified approach is further developed in Sec. 1.6.

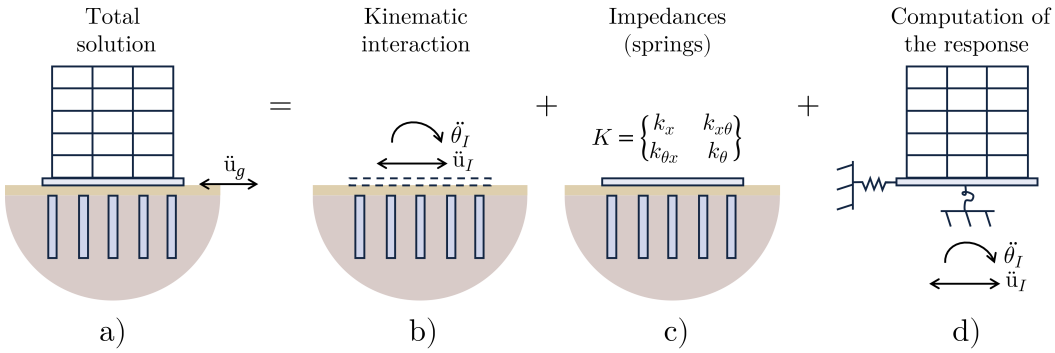

FIGURE 1.7 : Substructuring as a three-step solution a) Total solution; b) Calculation of the massless foundation's motion; c) Determination of the frequency-dependent stiffness matrix; d) Calculation of the response of the structure supported on the springs. Adopted from Kausel et al. (1978)

The actual practice employs the methods as mentioned above of different complexities to assess the effects of SSI on the seismic performance of RI foundations.

1.5 Seismic performance

Although the literature on the seismic performance of RI foundations is relatively limited, results showed that this solution can enhance the seismic resilience of structures, protecting against significant earthquakes. In this context, we mention the outstanding experimental and numerical research work on the design of the Rion Antirion bridge in Greece (Pecker and Teyssandier, 1998; Teyssandier et al., 2003; Combault and Teyssandier, 2005; Combault et al., 2005; Pecker, 2023)). The SSI analysis showed reduced seismic loads due to dissipation effects at the platform-raft interface and of the ultimate horizontal forces and moments at the foundation level.

Numerical simulations with the Finite Element Method (FEM) showed that the seismic response of a RI foundation without a structure exhibits a slight acceleration decrease (Mayoral et al., 2006; Rangel et al., 2008; Ángel Mánica Malcom et al., 2015). Recent parametric studies from Shen et al. (2022b) revealed that this reduction is more critical in

high frequencies, indicating that RI acts as a high-frequency filter. As a result, the signal that reaches a shallow foundation changes, with a beneficial effect on the structural response. This observation is consistent with what it is known for deep foundations (Kaynia and Kausel, 1982; Mylonakis and Gazetas, 2000).

Hatem (2009) compared the behaviour of a structure on a RI foundation and the same structure on a PRF. Solicitations are found to increase for the pile case, while displacements are found to be more important at the head of the RI and the ground surface. Similar conclusions were recently drawn by López-Jiménez and Dias (2022).

LTP has beneficial effects on the seismic performance of a RI foundation. It decreases the surface acceleration, dissipating energy through soil deformation and plasticity (Mayoral et al., 2006; López-Jiménez, 2019; Diaz-Guzman et al., 2021; López-Jiménez and Dias, 2022). The LTP also reduces the normal forces and moments within the inclusions Hatem (2009); Malcom (2013); Ángel Mánica Malcom et al. (2015) and elongates the period of the soil-foundation-structure system (Xu and Fatahi, 2018).

Finally, and although not within the scope of this study, RI foundations can be used for the seismic protection of structures against liquefaction (López-Jiménez et al. (2019a,b); López-Jiménez and Dias (2022)). Hamdan et al. (2023), for example, indicated that RI foundations diminish permanent liquefaction-induced horizontal and vertical deformations of coastal reclaimed backfill and foundation deposits, providing better performance for the subjected coastal structures.

Several approaches exist for the dynamic analyses of structures accounting for SSI under seismic loadings. Until recently, as presented in this Section, comprehensive analyses of SSI on RI foundations were infrequent, but modern applications (highlighting the positive contribution of the reinforcement technique) in zones prone to seismic loadings demand simplified tools accounting for the nonlinear SSI. In that context, this thesis aims to develop a simplified numerical tool based on the macroelement approach to simulate the non-linear behaviour of RI foundations subjected to static and seismic loadings.

1.6 Macroelement approach

The macroelement (ME) approach (Nova and Montrasio, 1991) involves the use of an upscaled 3D nonlinear constitutive relationship linking the generalised forces and the generalised displacements. The nonlinear behaviour of the foundation and surrounding soil is concentrated into a single element and placed at the base of the structure, as shown in Fig. 1.8 for a RI foundation. The 3D behaviour is numerically reproduced using the mathematical theory of plasticity, hypoplasticity, *etc.* Specific attributes of the local scale

are missing (*e.g.*, stresses and stains), except for those that play a critical role in the overall behaviour of the global model.

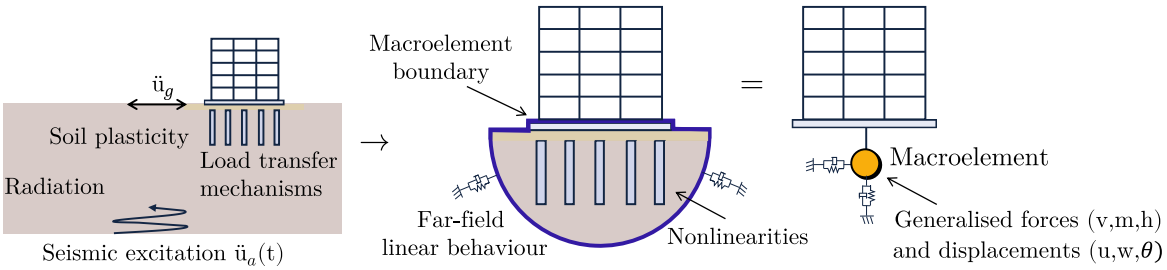

FIGURE 1.8 : Representation of the ME approach

ME modelling is derived from the concept of failure envelopes (Roscoe, 1956; Ticof, 1978; Schotman and Stork, 1987; Schotman, 1989; Gottardi, 1992; Gottardi and Butterfield, 1993). In their pioneering work, Nova and Montrasio (1991) postulated a relationship established between foundation displacements and external forces based on the theory of hardening plasticity, analogous to the constitutive law governing soils. Therefore, displacements were regarded as strains and forces as stresses and the complete foundation-soil system was considered as a ME. This work was the base of complete elastic-plastic ME formulations for strip and circular footings. It marked a significant paradigm shift in the study of nonlinear SSI, recognising that soil specimens and foundational systems share many characteristics at different scales, which can be modelled similarly.

Subsequently, other researchers adopted this concept and a wide array of ME models were developed within the plasticity framework, applied to diverse SSI problems, such as shallow foundations (Crémer et al., 2001, 2002; Chatzigogos et al., 2007; Grange, 2008; Chatzigogos et al., 2009), offshore plate-anchors and spud-can foundations (Wang, 2021; da Silva et al., 2019), buried pipelines, piled foundations (Correia, 2011; Correia et al., 2012; Correia and Pecker, 2021; Gorini and Callisto, 2023) but also structural elements (*e.g.*, reinforced concrete beam and column sections (Doulgeroglou et al., 2022)).

Plasticity-based ME are not the only approach available. For instance, Salciarini and Tamagnini (2009) used the generalised hypoplasticity theory (Niemunis and Herle, 1997) to develop a macro-element formulation for a shallow foundation to cyclic/dynamic conditions. Following the same approach, hypoplastic ME now exist for pile foundations (Li et al., 2015, 2018; Perez-Herreros, 2020), caisson foundations (Jin et al., 2019) and pipelines (Jin et al., 2021).

ME modelling maintains an adequate description of dynamic SSI while accounting for the nonlinear behaviour of soil mechanics. This approach accurately replicates foundations' behaviour under complex combined loading situations while demanding signi-

ficantly lower computational costs compared to direct nonlinear FEM simulations (Li, 2014). As a result, this approach offers an efficient and practical alternative to capture the essential aspects of SSI during seismic analysis (*i.e.*, the Rion Antirion bridge (Pecker and Teyssandier, 1998)).

A limitation of ME is its calibration procedure. It poses a significant barrier to the widespread adoption of this methodology in engineering practice. For instance, a fundamental component of the approach is the failure envelope. As it will be discussed in the next Section, its description relies on refined numerical simulations (or experimental data) and is specific to a foundation study case.

1.7 Failure envelopes

The (vertical) bearing capacity is used in design offices to define the admissible forces that a foundation system can support. However, due to the horizontal components of the earthquake, understanding the coupling of vertical forces, V, bending moments, M, and horizontal forces, H, is mandatory for an efficient and safe design against seismic loads. A way to overcome the modification factors for inclination and eccentricity of the classical bearing capacity approach (Terzaghi, 1943b; Meyerhof, 1953) is to use *failure envelopes*, *i.e.*, bearing capacity diagrams, represented as analytical equations providing the allowable states in the 3D $V - M - H$ space (Ticof, 1978; Butterfield, 1980).

In the case of a seismic event, reaching the allowable states in the bearing capacity diagram does not result in foundation failure (Cremer, 2001). However, it invariably aligns with the emergence of plastic deformations, such as permanent settlements, sliding, and rotations. These deformations can be significant and may present a threat to structural stability. Hence, incorporating failure envelopes is a significant advancement in seismic foundation design. For instance, they allow the quantification of the bearing capacity under complex loading and enable the development of simplified numerical methods to account for considering SSI through ME approaches.

Failure envelopes can be already found for different foundation types as shallow foundations (Tan, 1990; Nova and Montrasio, 1991; Bell, 1991; Gottardi and Butterfield, 1993; Sieffert et al., 2001; Houlsby and Cassidy, 2002; Vulpe et al., 2015; Shen et al., 2017; Suryasentana et al., 2020), skirted or caisson foundations (Bransby and Randolph, 1998; Bransby and Yun, 2009; Gourvenec and Barnett, 2011; Mehravar et al., 2016; Tian et al., 2016; Jin et al., 2019), piles (Fan and Meng, 2011; Correia, 2011; Correia et al., 2012; Li et al., 2014; Perez-Herreros, 2020; Correia and Pecker, 2021), piled-raft foundations (Chanda et al., 2021) but also structural elements (*e.g.*, reinforced concrete beam and

column sections (Doulgeroglou et al., 2022)).

The identification of a failure envelope is often made experimentally or/and numerically; see, for example, (Jin et al., 2019; Doulgeroglou et al., 2022). Design guidelines also provide empirically/analytically derived $V - M - H$ envelopes of the ultimate combined failure (Lesny, 2009) for shallow foundations (*e.g.*, ASCE/SEI, 2017; Paikowsky et al., 2010; Jeanjean et al., 2011; Eurocode 8, EN1998-5 (2004); french standards' application of Eurocode 8, AFNOR (2013a)).

1.7.1 Shallow foundations

Limit analysis (Paolucci and Pecker, 1997; Salençon et al., 1999), limit analysis coupled with FEM (Ukritchon et al., 1998) and experimental tests (Butterfield and Gottardi, 1994) were used to find the failure envelope of a shallow foundation. They all led to consistent results and were the basis of the following semi-empirical formulation adopted by the Eurocode 8 (EN1998-5, 2004) for a shallow foundation on a homogeneous soil:

$$g(v,h,m) = \frac{(\beta h)^{\mathrm{cT}}}{v^{\mathrm{a}}(1-v)^{\mathrm{b}}} + \frac{(\gamma m)^{\mathrm{cM}}}{v^{\mathrm{c}}(1-v)^{\mathrm{d}}} - 1 = 0 \tag{1.9}$$

where the parameters a, b, c, d, cT, cM, β and γ depend on whether the foundation ground is purely cohesionless or cohesive (see Tab. 1.2), while the forces $v := V/V_0$, $m := M/BV_0$ and $h := H/V_0$ are normalised with the maximal vertical force V_0.

TABLE 1.2 : Parameters used in Eq. 1.9

	Purely cohesive soil	Purely cohesionless soil
a	0.70	0.92
b	1.29	1.25
c	2.14	0.92
d	1.82	1.25
cT	2.00	1.14
cM	2.00	1.01
β	2.57	2.90
γ	1.85	2.80

The failure envelope (bearing capacity diagram) in the $v - m - h$ space for a shallow foundation on a cohesive and a cohesionless soil are shown in Fig. 1.9 and Fig. 1.10

respectively, (EN1998-5, 2004). Knowledge of these diagrams represents a significant improvement in the seismic design of foundations (Crémer et al., 2001) as the 3D couplings are explicitly taken into account.

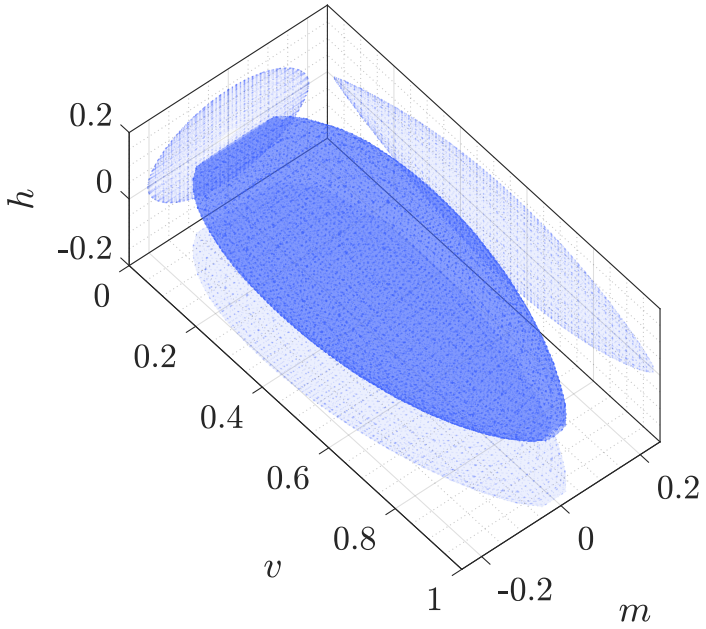

FIGURE 1.9 : Failure envelope of a shallow foundation in a cohesive soil, adapted from EC8 (EN1998-5, 2004)

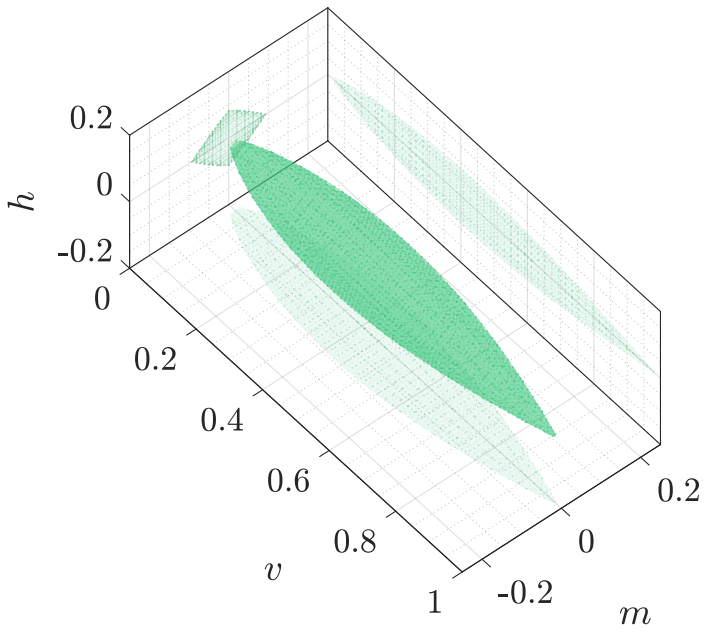

FIGURE 1.10 : Failure envelope of a shallow foundation in cohesionless soil, adapted from EC8 (EN1998-5, 2004)

1.7.2 RI foundations

Research concerning the simultaneous influence of vertical and lateral loads for the case of RI foundations is relatively scarce. Practical experience, as indicated by ASIRI recommendations IREX (2012), highlights that the additional benefits derived by adding shear forces of RI are limited. Consequently, neglecting the shear contribution, as suggested by ASIRI, does not significantly influence the overall stability analysis and remains a safe simplification. Nevertheless, it is important to quantify the various 3D couplings as lateral loads (*e.g.*, earthquakes) induce overturning moments, consequently diminishing the foundation load-bearing capacity (Zhu et al., 2018).

The ASIRI French national project introduced simplified models (named MV1-MV3 and MH1-MH3 for vertical and lateral loading) based on 3D numerical modelling results (IREX, 2012). However, no analytical formulation is proposed for cases where inclusions play a role in the bearing capacity of the foundation and where it is necessary to verify stability under complex load cases (Frattini et al., 2017). In ASIRI recommendations, the evaluation of stability in combined loadings is proposed using the *limit analysis*. This approach was used to construct the failure envelope (Salencon, 1990; Salençon et al., 1999; Paolucci and Pecker, 1997) for a given vertical force. This approach is similar to the

method employed for soil-nailed structures (Pecker, 2023). Pecker and Teyssandier (1998) applied this approach for the Rion-Antirion bridge to establish an upper bound on the foundation capacity.

A cross-section of the bearing capacity diagram using limit analysis is shown in Fig. 1.11, in the positive $M/B - H$ plane for a given V value[4]. It can be observed that the failure envelope for a RI foundation encompasses the failure envelope of a shallow foundation without RI. These results were consistent with numerical (FEM) and centrifuge experimental models.

Additionally, *Swipe tests* (Tan, 1990) can be used to determine the complete 3D failure locus; they are introduced in Chapter 3. Bransby and Randolph (1997) proposed the *displacement-probe* technique as a means to identify the yield point of a failure envelope. In the displacement probe test, the foundation is incrementally displaced in a specific direction from a fixed vertical load state until it reaches a steady-state load point, marking one spot on the failure envelope. To map the entire envelope, multiple tests with varied displacement directions are needed. While this method ensures convergence and identifies a clear failure load with adequate displacement, it is inefficient, providing just one data point per calculation. Moreover, its nonlinear load path makes it challenging to explore the entire failure envelope straightforwardly. For more information, see Suryasentana et al. (2020).

Although these methodologies have been used for different foundation types, to the best of the author's knowledge, neither numerical nor experimental 3D complete failure envelopes exist for RI foundations. Chapter 3 details the numerical procedure for identifying the complete 3D failure envelope for RI foundations, and a novel analytical equation is introduced.

4. Curves have been adapted from Pecker (2023), where $B = 90$ m and $V = 750$ MN

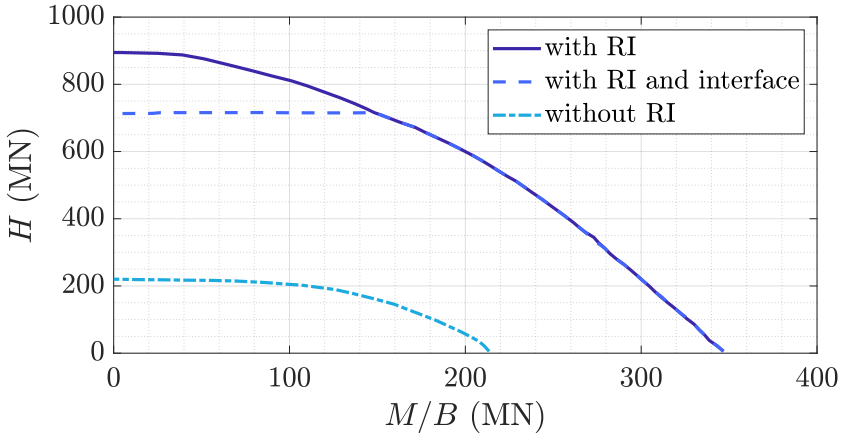

FIGURE 1.11 : Cross-section of the failure envelope for a RI foundation, adapted from Pecker (2023)

1.8 Conclusions

The literature review in this Chapter provides a comprehensive overview of the state-of-the-art research on RI foundations. It is found that they provide engineers with a practical and economical alternative approach to control settlement and enhance the foundation's vertical bearing capacity. The transfer mechanisms presented involve the transmission of loadings through the arching in the LTP and the frictional interaction between the inclusions and the soil. The vertical stress distribution to stiffer soil layers through the LTP and inclusions. Also, these mechanisms facilitate the redistribution of vertical to horizontal stresses, reducing the vertical stress transferred through the piles. As a consequence, the soil load-bearing capacity is significantly increased and enhances structural resilience, protecting against seismic loadings.

The approaches existing to account for the dynamic analyses of structures considering SSI under seismic loadings are presented. Although the seismic performance literature of RI foundations is relatively limited, results highlight the positive contribution of the reinforcement technique as it enhances the seismic resilience of structures, protecting against significant earthquakes. As a result, modern applications in zones prone to seismic loadings demand simplified tools accounting for the nonlinear SSI. The macroelement approach is introduced as the selected method developed in this work to simulate the non-linear behaviour of RI foundations subjected to static and seismic loadings.

Finally, numerous studies have been conducted on the behaviour of RI foundations under vertical loads. These studies mainly focus on the transfer mechanisms in the LTP and the RI. A noticeable gap in research is observed when it comes to the simultaneous

application of vertical and lateral loads or combined vertical-lateral-moment loads in RI-reinforced systems. Besides, the conventional design of RI foundations does not include the system's capacity under combined loadings. As a consequence, the investigation of the failure envelope of RI foundations using the available existing methodologies becomes evident. Also, as described in this Chapter, it is a fundamental concept when studying the nonlinear behaviour of foundations, serving as the cornerstone for the development of the simplified macroelement approach to account for SSI and study the seismic performance of RI foundations.

Chapitre 2

Validation of the 3D FEM model

This chapter presents a nonlinear 3D FEM model of a foundation with and without RI validated against recent centrifuge experimental data. A comparison between the experimental and numerical results and a comprehensive discussion of the behaviour of the two foundations is given in detail. The 3D FEM will be used in Chapter 3 to develop a novel failure envelope for RI foundations.

2.1 Introduction

This Chapter focuses on the validation of a nonlinear 3D FEM model of a foundation with and without RI using the recent centrifuge experimental campaign of Escoffier et al. (2022). The model incorporates the insights from two benchmarks conducted under the ASIRI PN project (ANR, 2020). These benchmarks, detailed in Appx. A and Appx. B, of RI foundation subjected to vertical and combined (vertical-horizontal) loading, respectively, provided foundational support for our validation efforts.

The subsequent Sections include (i) the centrifuge model configuration and soil characteristics, (ii) the 3D FEM model, (iii) a comprehensive discussion that entails a comparison between the experimental and numerical results, with a specific focus on the mechanical interpretation of the behaviour exhibited in the RI foundation.

2.2 Experimental campaign

2.2.1 Centrifuge model configuration

A schematic view of the centrifuge model in the prototype scale[1] is shown in Fig. 2.1, according to Escoffier et al. (2022). The centrifuge test is conducted at a gravity level, noted N, of 50 g. Two identical circular foundations, with and without RI, were tested. The shallow footings have a diameter of B =6.0 m, a thickness of H_{slab}=1.0 m, a weight of 150 tonnes and are directly placed on the LTP surface.

1. The centrifuge model is reduced by a factor of 50 compared to the dimensions in the real-world prototype.

Three distinct soil layers are positioned from the top to the bottom, as outlined below:

i) LTP (Upper layer): Dry Hostun sand mix (HN5-sand mix) consisting of five Hostun sand fractions with a 1 m thickness;

ii) Soft Soil (Intermediate Layer): situated beneath the LTP with a thickness of 9.5 m, this layer is a mixture of 80% Speswhite kaolin clay and 20% Fontainebleau sand;

iii) Stiff Soil (Lower Layer): saturated dense Hostun HN31 sand with a 4 m thickness.

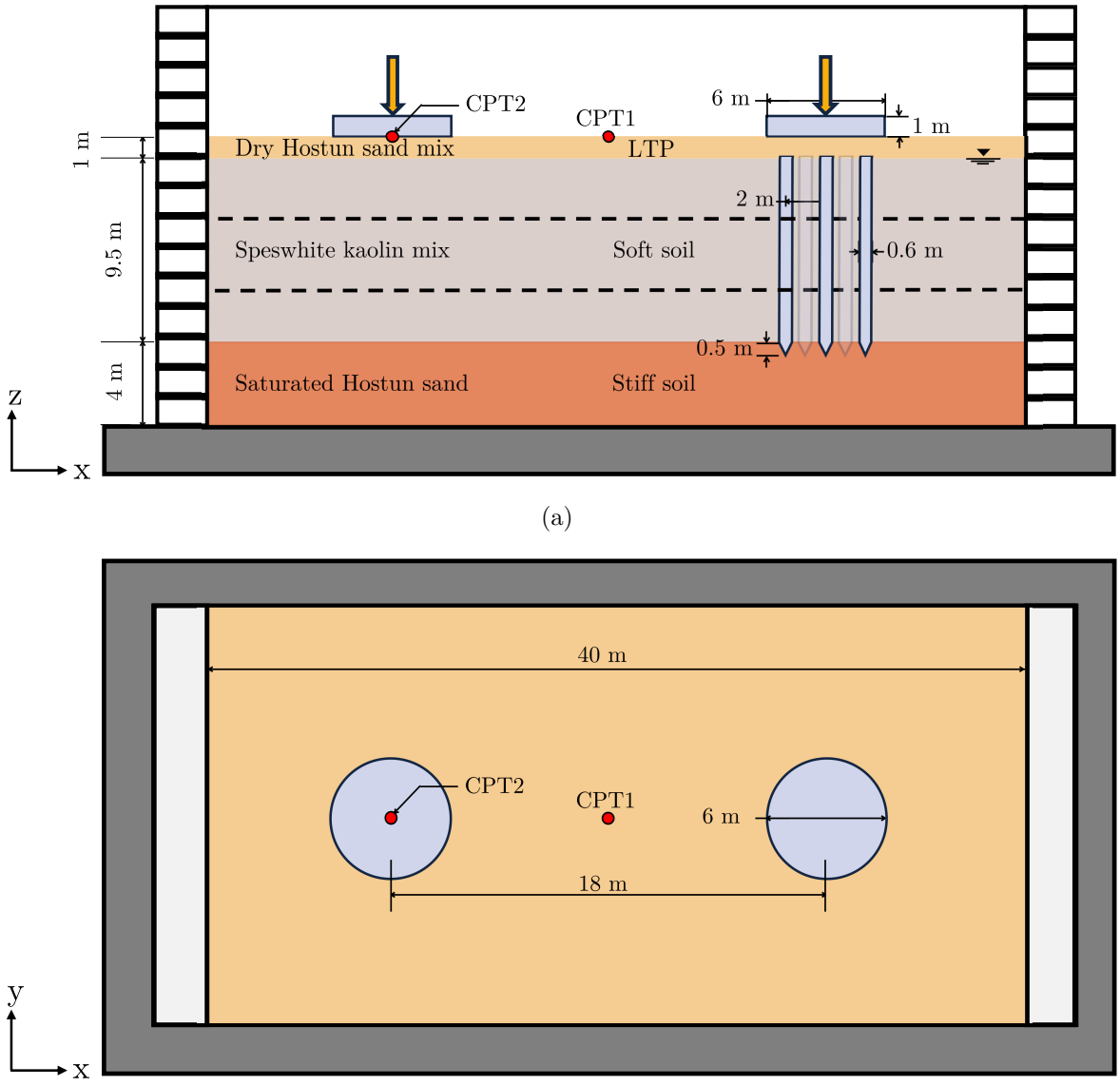

FIGURE 2.1 : Centrifuge model of two identical circular shallow foundations without (left) and with RI (right), prototype scale: plane view (a) from the front and (b) from above, (Escoffier et al., 2022)

The groundwater level is below the LTP at −1 m. The shallow foundation on the right is reinforced with seven circular vertical RI that belong to class 3, category 8 according to Annex A of the French norm AFNOR (AFNOR, 2013b).

The RI are placed under the LTP. They have a length of 10 m, covering the soft soil and embedded with a 0.5 m penetration in the stiff soil. They have a diameter d = 0.60, a centre-to-centre 2.0 m and a weight of 4.75 tonnes. The coverage area α is defined as the total surface area of the RI cap (A_{RI}) over the total foundation top surface (A_{slab}), and it is given (in percentage) as:

$$\alpha = N_{RI} \cdot \frac{A_{RI}}{A_{slab}} = N_{RI} \cdot \frac{d^2}{B^2} \tag{2.1}$$

where N_{RI} is the number of RI. The models' geometric characteristics allow estimating a coverage area $\alpha = 7.0\%$ for the RI foundation.

2.2.2 Soil characteristics

LTP layer-HN5 sand mix

The LTP layer is composed of unbound gravel materials with very angular grains, employed to achieve a significant load transfer in the RI and subsequently to enhance shear strength development in the mattress (Baudouin et al., 2008; Blanc et al., 2013; Girout et al., 2014; Blanc et al., 2014). The centrifuge model employs a mix of five Hostun sand fractions (HN38, HN34, HN31, HN04/08, HN06/1), according to Baudouin et al. (2008); Baudouin (2010); Okyay et al. (2014). The key characteristics of the sand mix are outlined in Tab. 2.1.

Table 2.1 : HN5-sand mix main characteristics from Baudouin et al. (2008)

Characteristic	Symbol	Value	Unit
Diameter at 0.1 passing	d_{10}	0.125	mm
Diameter at 0.5 passing	d_{50}	0.32	mm
Diameter at 0.9 passing	d_{90}	0.88	mm
Coefficient of uniformity	C_U	3.52	-
Coefficient of curvature	C_C	0.88	-
Minimum dry density	$\rho_{d,min}$	1.4	g/cm^3
Maximum dry density	$\rho_{d,max}$	1.73	g/cm^3
Minimum void ratio	e_{min}	0.532	-
Maximum void ratio	e_{max}	0.893	-
Density of sand	G_s	2.65	g/cm^3

The components of varying grades are blended within a container. The soil has a broad range of particle sizes, with the largest diameter being 1 mm. Fig. 2.2 illustrates the particle size distribution curves for the different Hostun sand employed (dots) and the final Hostun sand mix curve (red line), as described in Baudouin et al. (2008). The density of the sand mix varies between a minimum of $\rho_{d,\min} = 1.4$ g/cm^3 and a maximum of $\rho_{d,\max} = 1.73$ g/cm^3 resulting in a void ratio range of $e_{\min} = 0.532$ and $e_{\max} = 0.893$. Referring to the work of Ovesen (1979), the influence of particle size is disregarded when the ratio of the inclusion's diameter in the model scale, $d_{\text{model}} = 12$ mm, to the average soil particle diameter, $d_{50} = 0.32$ mm, exceeds 30. According to Tab. 2.1, d/d_{50} equals to 37.5, so the soil particle size effects are neglected (see Nadimi et al. (2016) for more information).

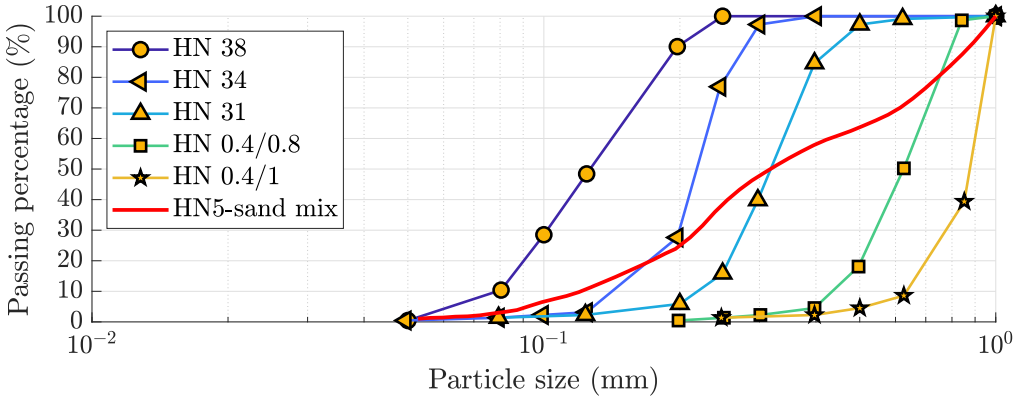

FIGURE 2.2 : Particle size distribution curve of Hostun sand and Hostun sand mix used for the centrifuge tests from Baudouin et al. (2008)

Soft soil layer-Speswhite kaolin clay

The soft soil layer, a compressible soil, is a mixture of 80% Speswhite kaolin clay and 20% Fontainebleau sand. Clays typically exhibit low permeability, resulting in prolonged consolidation times during model preparation. Speswhite kaolin clay stands out due to its relatively higher permeability, accelerating the consolidation process (Perez-Herreros, 2020). This advantageous quality makes it a prevalent choice for crafting laboratory setups, particularly in centrifuge tests involving cohesive soil compositions (Garnier, 2001). Khemakhem (2012) performed a comprehensive physical and mechanical analysis of the Speswhite kaolin clay. Its fundamental properties are outlined in Tab. 2.2.

The Université Gustave Eiffel[2] centrifuge facility has extensively employed Speswhite kaolin clay in prior experimental investigations (*e.g.*, Akou, 1995; Baudouin, 2010; Okyay

2. Gustave Eiffel University (*ex.* IFSTTAR)

et al., 2014; Perez-Herreros, 2020). However, supplementary geotechnical tests were performed before in-flight tests to identify some soil material characteristics of the mix. For instance, Fig. 2.3 illustrates the experimental oedometric test (S01, S02, S03) from (Escoffier et al., 2022) results in the $e - \sigma_1$ plane. Mean values from those tests (Escoffier et al., 2022) allow us to calculate the compression, $C_c = 0.269$, and rebound, $C_s = 0.048$, indices.

TABLE 2.2 : Properties of Speswhite kaolin clay (Khemakhem, 2012)

Characteristic	Symbol	Value	Unit
Plasticity index	w_P	30	%
Liquid limit	w_L	55	%
Compression index	C_c	0.33	-
Recompression index	C_s	0.06	-
Plasticity index	I_P	25	%
Density of grains	Gs	2.65	g/cm^3

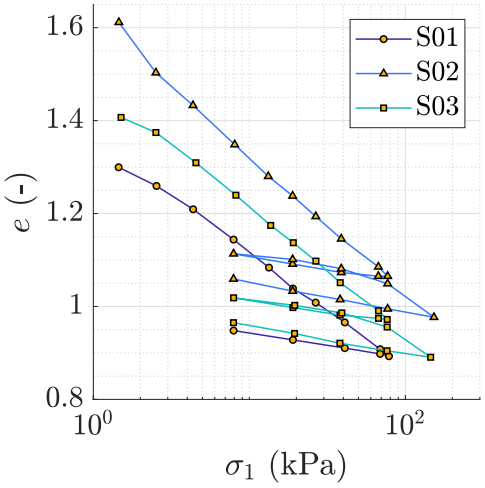

FIGURE 2.3 : Experimental oedometric test results: stress vertical load increment, σ_1, versus void ratio, e, from Escoffier et al. (2022)

Stiff soil-Hostun sand HN31

The model's base stiff soil layer is composed of Hostun sand HN31; see Tab. 2.3. It was installed by air pluviation in order to achieve a relative density of 80%. Air pluviation was performed using a sand pluviator featuring a 4 mm slot opening, and a falling height of 750 mm Escoffier et al. (2022).

HN31 sand is a widely recognised reference material in numerous research studies (Perez-Herreros, 2020). It is a finely textured and consistently graded sand exhibiting an angular to sub-angular grain shape. This sand has a medium diameter of $d_{50} = 0.35$ mm and a uniformity coefficient, $C_U = 1.57$, as detailed in Benahmed (2001). Fig. 2.2 provides a grain size distribution curve of the HN31, confirming its uniformity within the medium sand category.

TABLE 2.3 : Properties of Hostun HN31 sand (Benahmed, 2001)

Characteristic	Symbol	Value	Unit
Diameter at 0.5 passing	d_{50}	0.35	mm
Coefficient of uniformity	C_U	1.57	-
Minimum void ratio	e_{min}	0.656	-
Maximum void ratio	e_{max}	1	-
Density of the grains	$\rho_s = 1.4$	2.6	g/cm^3
Minimum dry density	$\rho_{d,min}$	1.305	g/cm^3
Maximum dry density	$\rho_{d,min}$	1.57	g/cm^3

2.2.3 Stress state variables in the soil profile

Water content ratio

The water content, w, is determined as the ratio of the mass of water in the soil to the total mass of the soil sample. The profile in the soft soil is measured for two samples, S01 and S02 (Escoffier et al., 2022). In the stiff layer, the water content, $w = 16\%$, is estimated from Perez-Herreros (2020), which used the same saturated dense sand in similar test conditions. The water content profile is shown in Fig. 2.4.

Soil density

The soil density, γ, is calculated using the relation for saturated soils:

$$\gamma = \frac{\gamma_s + \gamma_w e_0}{1 + e_0} \tag{2.2}$$

where γ_s is the density of the grains, taken equal to 26.5 kN/m^3, according to Khemakhem (2012), and γ_w the specific weight of water, considered equal to 10 kN/m^3. The void ratio, e_0, after consolidation is calculated as:

$$e_0 = w\frac{\gamma_s}{\gamma_w} \tag{2.3}$$

Vertical effective stress

The vertical effective stress profile is calculated using the Terzaghi relation:

$$\sigma' = \sigma - u \tag{2.4}$$

where σ is the total vertical stress, calculated as $\sigma = \gamma \cdot z$, z is the soil depth and u is the pore water pressure, considering the water level at -1 m, as shown in Fig. 2.1 (a).

Overconsolidation ratio

The overconsolidation ratio (OCR) is defined as the ratio of the current effective stress to the past maximum effective stress experienced by the soil deposit. This characteristic of compressible soils provides valuable information about the history of stress and loading conditions the soil has endured.

The soft soil is installed in three consistent layers, with a total thickness of 9.5 m. This compressible soil is exposed to a preloading pressure of 120 kPa under a $N = 1$ g gravitational force. The number and thickness of clay layers are determined by considering the applied consolidation pressure, container size, and the overall duration required for effective consolidation (Perez-Herreros, 2020). The OCR is then computed by comparing the pre-consolidation stress σ'_c applied under 1g conditions with the resultant effective stress σ'_N experienced under 50 g conditions, given by:

$$OCR = \frac{\sigma'_c}{\sigma'_N} \tag{2.5}$$

defined as the ratio between the pre-consolidation stress applied at 1 g, $\sigma'_c = 120$ kPa, and the effective vertical stress, σ'_N, at the gravity level N= 50 g.

Undrained shear strength

After the experimental tests, in-flight Cone Penetration Test (CPT) investigations are performed at the free field area between the footing locations (CPT1) and the middle of one footing (CPT2), see Fig. 2.1, to measure the cone penetration resistance, q_c. To calculate the experimental undrained shear strength $s_{u_{exp}}$ profile in the kaolin clay mix, the well-known correlation between the undrained strength, $s_{u_{exp}}$, and q_c, is employed (Garnier, 2001):

$$s_{u_{exp}} = \frac{q_c}{18.5} \tag{2.6}$$

Position CPT1 was strategically chosen to be significantly distant from the two shallow foundations, ensuring the soil remained undisturbed in that area. Consequently, the s_{u} value derived from CPT1 served as the reference value. Notably in Fig. 2.4, between depths of -2 m and -5 m, the recorded results were higher than expected, a discrepancy attributed to the precision limitations of the CPT test. In the centrifuge model, CPT results are more reliable when the penetration depth exceeds ten times the diameter of the CPT tip cone (Guo et al., 2022). Given the 12 mm diameter of the CPT used in the model's measurements, accuracy was achieved if the prototype depth exceeded 6 m (10 times the diameter, under 50 g, converting mm to m by dividing by 1000). Observations indicated that beyond approximately -5 m, the experimental CPT results closely aligned with the theoretical values $s_{\mathrm{u_{th}}}$.

To estimate the theoretical undrained shear strength $s_{\mathrm{u_{th}}}$ profile, the stress history relation from Ladd and Foott (1974) is given by:

$$s_{\mathrm{u_{th}}} = \mathrm{S}\sigma'_v(\mathrm{OCR})^{\mathrm{m}} \tag{2.7}$$

with S = 0.18 and m = 0.8 approximated values from (Lau, 2015) for a similar clay. The calculated profile (in a continuous line) is displayed in Fig. 2.4.

From the theoretical profile, the calculated average $s_{\mathrm{u,avg}} = 17.15$ kPa corroborates the target $s_{\mathrm{u}} = 20$ kPa profile of the design pre-experimental setup Escoffier et al. (2022).

Shear wave velocity

As proposed by Hardin and Drnevich (1972), the shear modulus, G, is calculated as:

$$G = 625\frac{\mathrm{OCR}^k}{0.3 + 0.7e_0^2}\sqrt{p_a\sigma'_{\mathrm{m}}} \tag{2.8}$$

where OCR is variable in depth, $\sigma'_m = (\sigma'_1 + \sigma'_2 + \sigma'_3)/3$ is the effective mean normal stress, p_a is the atmospheric pressure ($\approx$ 100 kPa) and e_0 is the initial void ratio. k is related to the plasticity index, I_{p}, and it is taken 0 and 0.21 for the sand and clay, respectively. Finally, the shear wave velocity is calculated from

$$V_{\mathrm{s}} = \sqrt{\frac{G}{\rho}} \tag{2.9}$$

A specific measurement of the shear wave velocity profile ($V_{\mathrm{s}} = 98.0$ m/s, at z=-2.0 m) was provided by Escoffier et al. (2022) using bender-elements, marked as BE in Fig. 2.4, corroborating the calculation of the V_{s} profile using Eq. 2.9.

2.2.4 Synopsis of the values adopted

Fig. 2.4 presents (in continuous lines) the evolution of the water content, w; the soil density, γ; the effective stress, σ'; the overconsolidation ratio, OCR; the undrained shear strength, s_u; and the shear wave velocity, V_s with depth. More details are given hereafter:

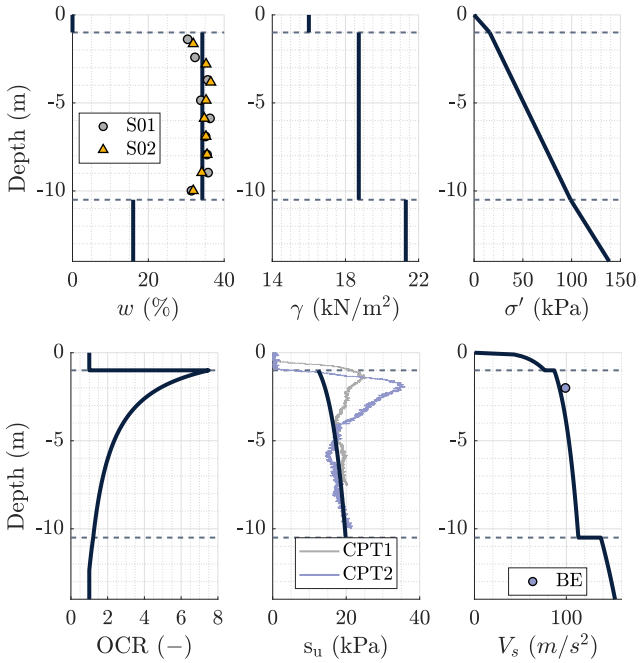

FIGURE 2.4 : Soil profiles (from left to right): water content, w, soil density, γ, effective stress, σ', overconsolidation ratio, OCR, undrained shear strength, s_u, and shear wave velocity, V_s

The different physical parameters of the soil layers obtained from the experimental data of the centrifuge test are presented in the Tab. 2.4. The table presents the three layers' depth; the water content, w; the soil density, γ; the overconsolidation ratio (OCR); the void ratio e_0, the shear wave velocity V_s, the average undrained shear strength, $s_{u_{avg}}$; and the compression, C_c, and rebound, C_s, indices.

TABLE 2.4 : Physical parameters for the different soil layers

Layer	Depth (m)	w (%)	γ kN/m^2	OCR (−)	e_0 (−)	V_s (m/s^2)	$s_{u,avg}$ (kPa)	C_s (−)	C_c (−)
LTP	$0-1.0$	-	16.0	1	0.721	calculated	-	-	-
Soft soil	$1.0-10.5$	34	18.7	$7-1$	0.890	by Eq. 2.8	17.15	0.048	0.27
Stiff soil	$10.5-14.5$	16	21.3	1	0.416	and Eq. 2.9	-	-	-

2.2.5 Quasi-static vertical loading

The quasi-static loading was applied in the vertical direction at the centre of the foundations with and without RI by a displacement-controlled actuator. Fig. 2.5 shows the applied displacement loading history.

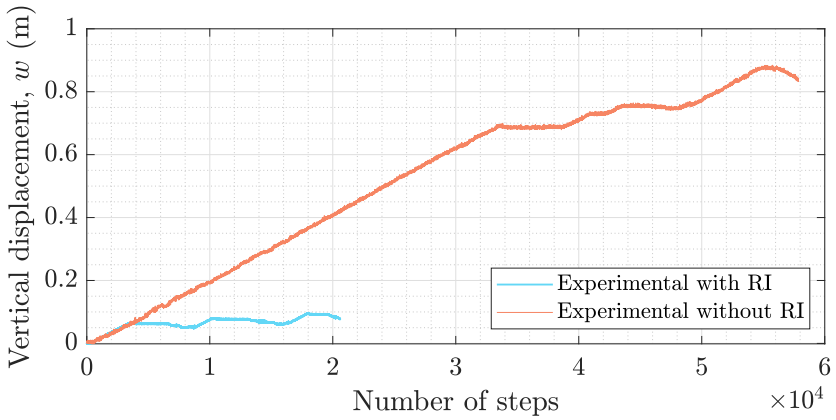

FIGURE 2.5 : Applied displacement loading histories for shallow foundations with and without RIs

2.2.6 Experimental results

The experimental results are shown in Fig. 2.6. The figure displays the vertical displacement vs the vertical force at the footing's centre. Three loading/unloading cycles were performed to provide information on the soil-foundation system's elastic stiffness. For the case of the shallow foundation without rigid inclusions, the maximal penetration value is close to 0.85 m. The maximum imposed vertical displacement is 0.1 m for the RI foundation; this is done to protect the RI and avoid buckling.

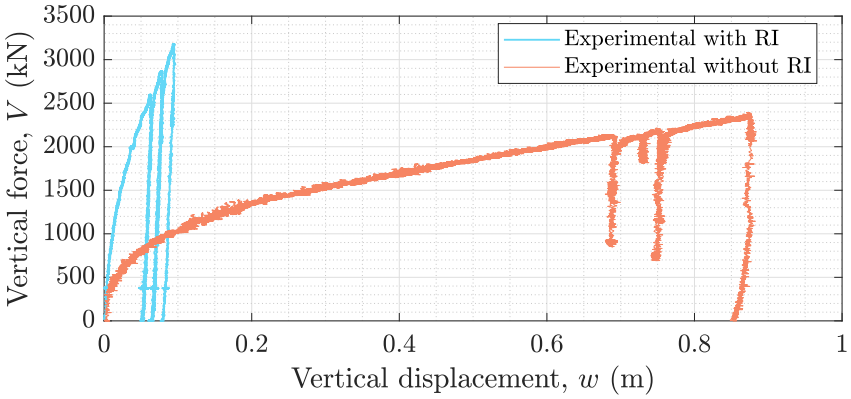

FIGURE 2.6 : Vertical force vs vertical displacement at the footing: experimental results for the foundation with (blue) and without (red) RI

2.3 3D FEM model

2.3.1 Spatial discretisation and boundary conditions

The centrifuge tests are simulated hereafter using the general purpose finite element code Cast3M (CEA, 2001), developed by the Commissariat à l'énergie atomique et aux énergies alternatives[3] (CEA) in France. The mesh of the models is depicted in Fig. 2.7. Due to symmetry considerations, only half of the domain is taken into account. Two 3D finite element models are created, one for the shallow foundation without RI and another for the RI foundation. Both models have identical dimensions, measuring $8B \times 4B \times 2.5B$, with B the foundation diameter being equal to 6.0 m.

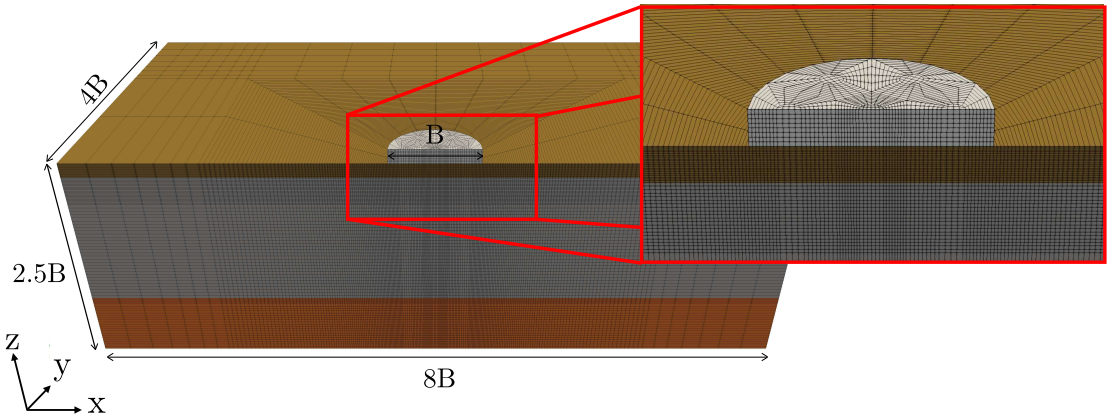

(a)

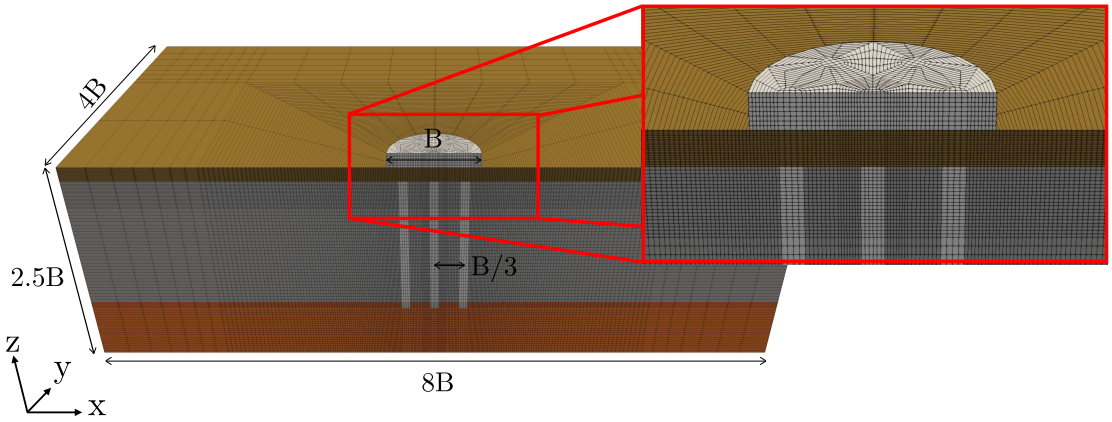

(b)

FIGURE 2.7 : Finite element mesh and geometry for the foundation (a) without and (b) with RI

3. French Alternative Energies and Atomic Energy Commission

The same discretisation is employed for both models consisting of 148775 8-node hexahedral elements (referred to as CUB8 in (CEA, 2001)). Preliminary numerical analyses have revealed regions with significant plastic strains, necessitating a local mesh refinement near the RI and the edges of the footing, as shown in Fig. 2.7. The minimum element size is set at 0.0707 m × 0.0707 m.

As boundary conditions, nodal displacements are fixed in the x, y and z directions at the base of the FEM models. In the symmetry plan $x - z$ at $y = 0$, the imposed *symmetry conditions* imply that the normal displacements to the plane are constrained to be zero (Demkowicz, 1991). Displacements at the other lateral boundaries are blocked in normal directions. No slippage is allowed between the soil and the RI because of the overconsolidation ratio OCR>1, which leads to significant adhesion between the soil and the RI.

2.3.2 Constitutive models and material parameters

A linear elastic (EL) behaviour is adopted for the footing and the RI. Because soil nonlinearities need to be accounted for in the LTP and the stiff soil layer, it was decided to consider a perfect elastoplastic Drucker-Prager (DP) constitutive model with a non-associated flow rule ($\psi \neq \varphi$). The parameters from the DP model are calibrated to reproduce the classical Mohr-Coulomb (MC) model (see, Appx. A).

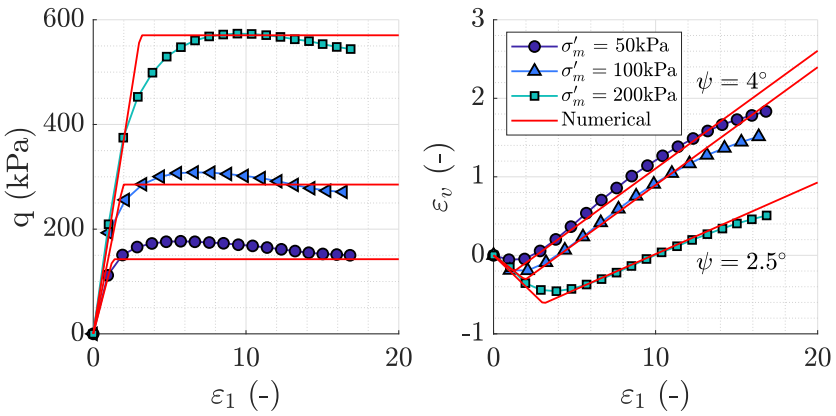

FIGURE 2.8 : Experimental triaxial compression results (dots) and numerical calibration (red lines) (a) deviatoric stress, q, versus axial strain, ε_1 (b) volumetric strain, ε_v, versus axial strain, ε_1. Hostun mix sand with a relative density $I_d = 0.9$, from Baudouin (2010)

A comparison between triaxial experimental results (Baudouin, 2010) and the calibrated DP model are presented in Fig. 2.8.

More specifically, the experimental triaxial compression tests of Hostun mix sand with a relative density I_d=0.9 (Baudouin, 2010), for different confining pressures, σ'_m, of 50, 100, and 200 kPa are presented in Fig. 2.8. They are employed to identify the friction angle $\varphi = 36°$ employed in the numerical model. Two dilatancy angles $\psi \in (2.5, 4)°$ are calibrated from the same experimental tests. This variation is related to the confining pressure in the triaxial tests. Results in Fig. 2.8 show a good agreement between the experimental and numerical results.

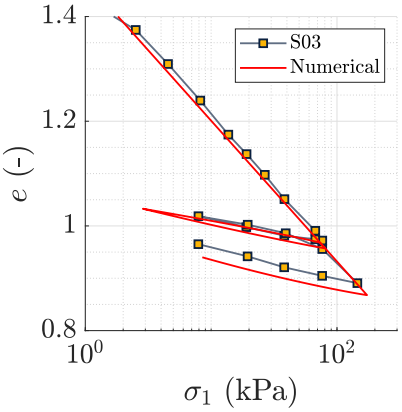

FIGURE 2.9 : Experimental results (dots) and numerical calibration (red lines) of clay. Experimental oedometric test results to stress vertical load increment, σ_a, versus void ratio, e, from Escoffier et al. (2022)

Moreover, for the soft soil the elastoplastic strain hardening Modified Cam-Clay model (MCC) is adopted. The frictional constant, M, defined as the ratio q'/p' at the critical state line, is related to the critical state friction angle φ_c by the relation:

$$M = \frac{6 \sin \varphi_c}{(3 - \sin \varphi_c)} \tag{2.10}$$

where the critical state friction angle φ_c is 18° estimated from Muhammed (2015) experimental results for a similar clay in low confining pressures. From Eq. 2.10, M is found equal to 0.689. The numerical parameters λ and κ are determined from the compression, C_c, and rebound, C_s, indices of the oedometer test (Escoffier et al., 2022), see Fig. 2.9 and Tab. 2.2. The normal consolidation line λ is defined by:

$$\lambda = \frac{C_c}{\ln(10)} = 0.117 \tag{2.11}$$

and the swelling line κ as:

$$\kappa = \frac{C_s}{\ln(10)} = 0.021 \tag{2.12}$$

The comparison of the experimental S03 sample from Escoffier et al. (2022) with the numerical results is shown in Fig. 2.9, where a good agreement can be observed.

Poisson's ratio $\nu = K_0/(1 - K_0)$ is adopted for the numerical model where K_0 is the lateral earth pressure coefficient at rest, determined as $K_0 = (1-\sin\varphi)\mathrm{OCR}^{\sin\varphi}$. Given the overconsolidated soil levels, ν is set equal to a maximal 0.45 to avoid numerical problems. The model considers the variation of the parameters in depth. For instance, the variation of the adopted V_s soil profile with depth is given in Fig. 2.10. The same is considered for all the stress state variables in the soils.

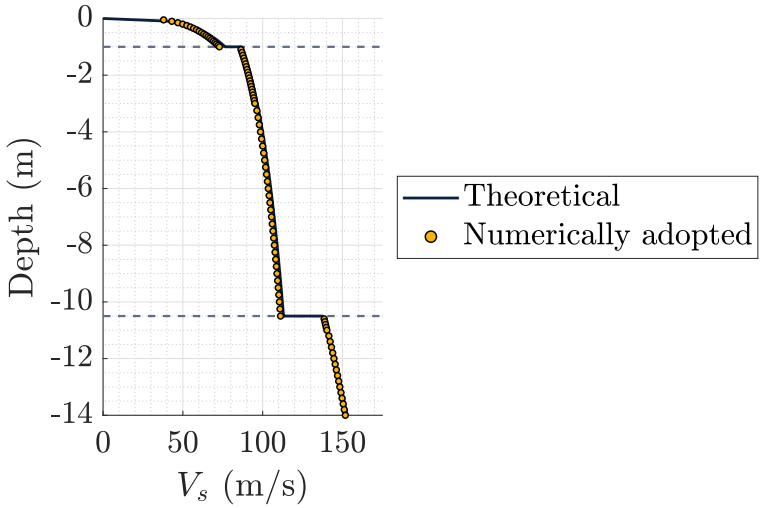

FIGURE 2.10 : V_s soil profile - comparison of theoretical and numerically adopted values in the FEM model.

The main properties used for the soils, footing and RI in the numerical model are presented in Tab. 2.5.

TABLE 2.5 : Geotechnical parameters for the different soil layers of the finite element model

Material	Model	ρ (kg/m^3)	φ (°)	ψ (°)	ν (-)	V_s m/s	E (MPa)	λ (-)	κ (-)
Footing	EL	5305	–	–	0.2	–	2.E10		
RI	EL	1680	–	–	0.2	–	20.E3		
LTP	DP	1600	36	2.5	0.3	0 – 72	7-26		
Soft soil	MCC	870	18	–	0.45 – 0.4	84 – 115	39-65	0.117	0.021
Stiff soil	DP	1130	36	2.5	0.3	146 – 160	93-117		

2.3.3 Loading procedure

The numerical loading procedure is composed of four stages detailed hereafter:

- Stage 1: Initialisation of the geostatic stresses considering a pre-consolidation pressure of 120 kPa; there is no RI at this stage.
- Stage 2: assignment of properties to the mesh groups corresponding to the inclusions (the RI installation phase is not simulated);
- Stage 3: activation of footing's self-weight;
- Stage 4: application of the prescribed loading at the top of the footing. More specifically, a monotonically increasing vertical displacement is first applied to find the vertical force versus vertical displacement curve. Then, force-controlled tests are performed to reproduce the loading/unloading cycles of the experimental results, see Fig. 2.11.

Remark: According to di Prisco and Pisanò (2014), after soil excavation, and when the RI are grouted, the borehole is often supported to prevent significant alterations in the soil stress state. When RI are directly driven into the soil, the surrounding material is compacted; in this case, ignoring the installation process is probably a conservative approach. In the centrifuge tests studied here, RI were installed before the in-flight test at 1 g. RI installation is, therefore, not expected to have significant effects, and it is not considered in the FEM model analysis.

2.4 Numerical vs experimental results

2.4.1 Footing

A good agreement between the experimental and numerical results for the foundations with and without RI can be observed in Fig. 2.11 in terms of initial stiffness, hardening behaviour, residual vertical displacements, unloading and reloading responses at the footing.

From an engineering perspective, the settlement (vertical displacement) efficiency, η_s, of a RI foundation is defined as

$$\eta_s = \frac{w_{\text{un}} - w_{\text{RI}}}{w_{\text{un}}} \tag{2.13}$$

with w_{RI} the RI foundation vertical displacement and w_{un} the vertical displacement of the foundation without RI for the same loading conditions, (Fioravante and Giretti, 2010; Tradigo et al., 2015; Zhang et al., 2022). For a fixed vertical force $w_{\mathrm{un}} > w_{\mathrm{RI}}$ and $0 \leq \eta_s \leq 1$. Hence, a greater η_s indicates a higher efficiency of the RI foundation. Results in Fig. 2.11 illustrate a significant vertical displacement reduction, as η_s varies from 0.86 to 0.95, for a vertical load of 1000 kN and 2000 kN, respectively.

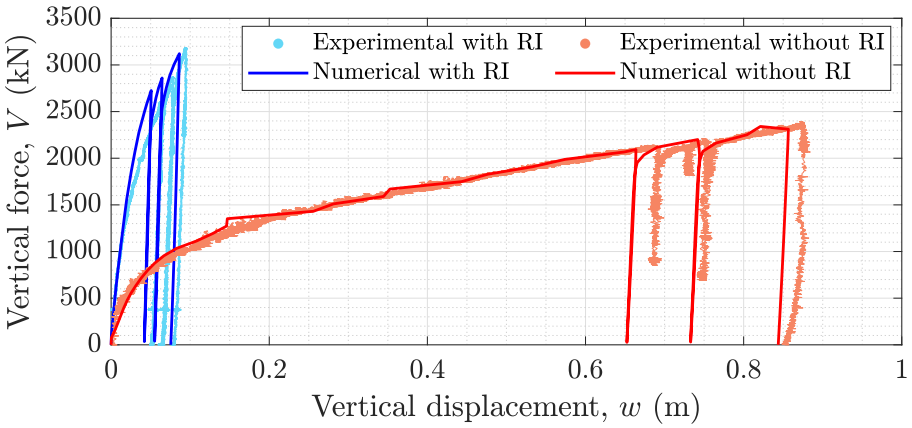

FIGURE 2.11 : Vertical force vs vertical displacement at the footing: experimental and numerical results for the foundation with (blue) and without (red) RI

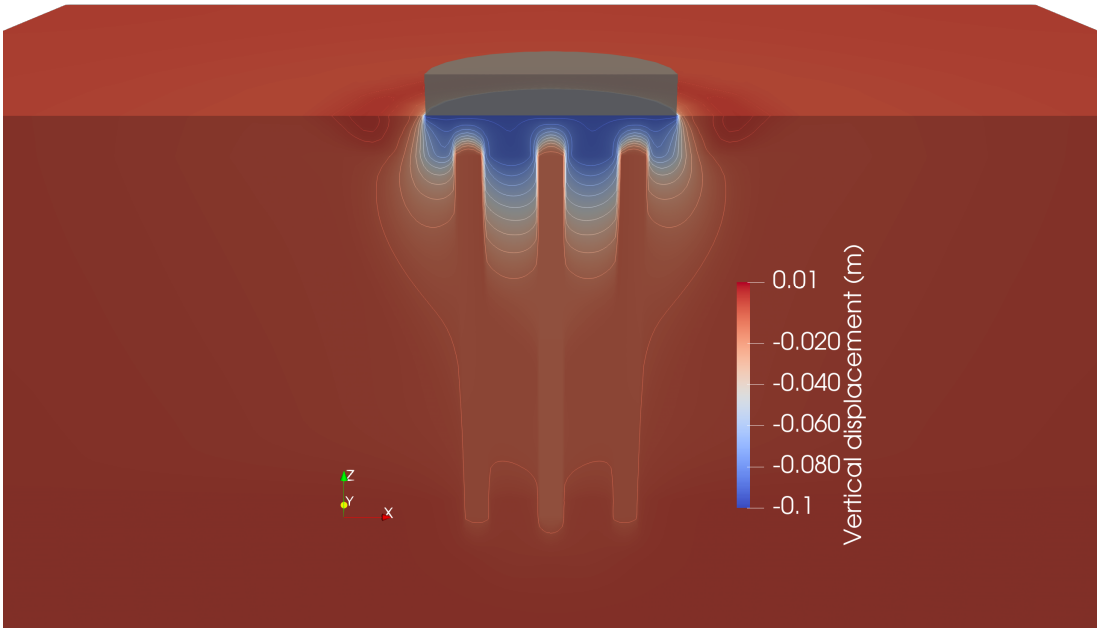

FIGURE 2.12 : Vertical displacement field below the RI foundation for a vertical displacement 0.09 m of the footing (1.5% w/B)

From numerical results, it is possible to obtain further insights into the distinct soil-foundation interaction mechanisms of the RI foundation by examining the vertical displacement profile field in Fig. 2.12 at a vertical displacement 0.09 m of the footing (*i.e.*, 1.5% w/B). A uniform distribution of the vertical displacements beneath the footing is observed, with minimal deviations from the mean value. This uniformity plays a vital role in the mitigation of punching effects and differential settlements, thereby ensuring a stable structural response. Fig. 2.12 also demonstrates that the absence of a continuous connection between the RI and the footing leads to variations in the vertical displacement between the RI and the closely surrounding soil.

The soil-RI interaction mechanism is elucidated in Fig. 2.13, which compares the vertical displacements of the inclusion (section 'a-a' in red line) and the soil within two RI (section 'b-b' in blue line). The soil vertical displacements w_s are more significant than the RI vertical displacements w_p at the upper portion of the inclusion shaft. With increasing depth, w_p remains relatively constant, while w_s exhibits a notable decrease. This transition leads to a shift in the variation of vertical displacements from positive to negative values, ultimately resulting in the emergence of a *neutral plane* at a certain depth. These findings align with earlier experimental observations (see, for instance, Fioravante and Giretti, 2010; Tradigo et al., 2015; Acar and Mollamahmutoglu, 2023), indicating the potential of the numerical model to simulate realistically the behaviour of a foundation with RI.

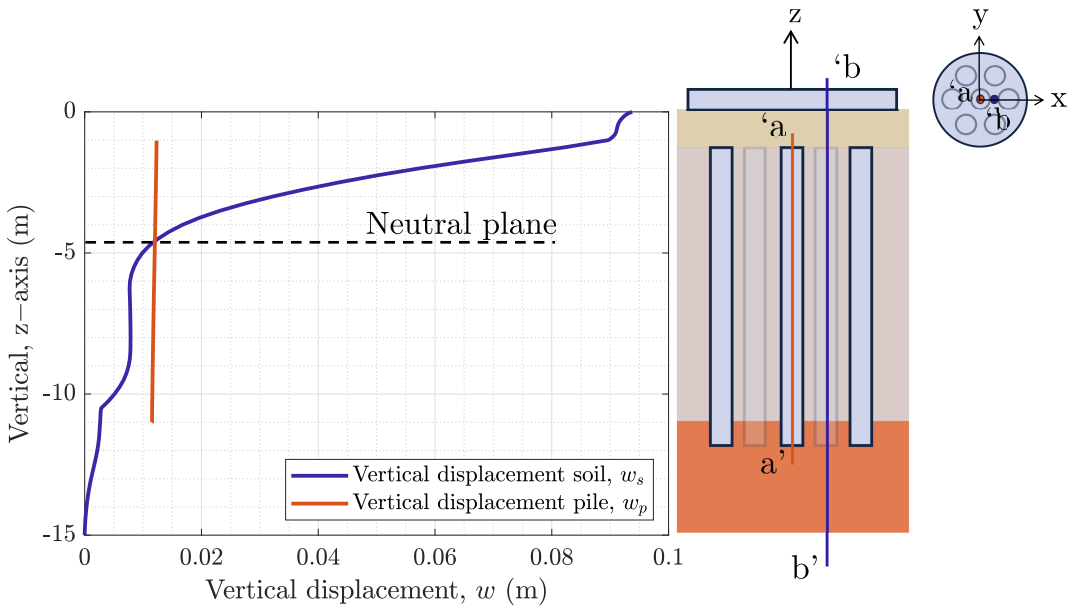

FIGURE 2.13 : Vertical displacement profiles for the inclusion (section 'a−a') and the soil within two RI (section 'b−b')

Theoretically, the maximum axial force is located in the neutral plane (Tradigo et al., 2015). This *equal settlement plane*, as defined in (IREX, 2012), is a distinctive feature of ground improvements involving RI (Simon, 2012). It is worth noting that it depends on various geometrical and material factors and has implications for the spatial distribution of the axial force within the inclusion, as discussed in Chapter 1.

Fig. 2.14 presents the vertical stress distribution within the soil (the stresses in the RI are not shown). One can observe the *arching effect* (Terzaghi, 1943a), triggered by the contrast in stiffness between the RI, the surrounding soil and the LTP (see also Sec. 1.2).

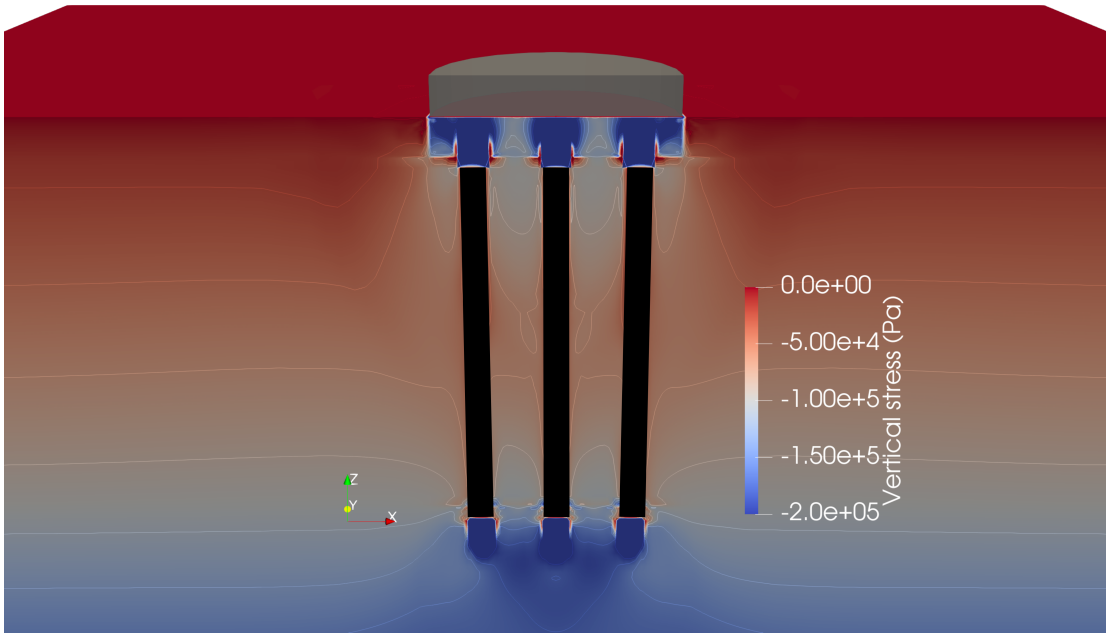

FIGURE 2.14 : Vertical stresses in the soil

Due to the low capacity of the soft soil, the vertical stress is concentrated at the LTP and transferred predominantly to the stiff soil layer by the RI, as observed in blue colors in the figure. However, some vertical load is also shared with the soft soil, not only through the RI, generating a soil pressure bulb beneath the footing. Consequently, an evaluation of the influence of various geometric and material characteristics on settlement efficiency is carried out in Appx. D through a parametric study.

2.4.2 Rigid inclusions

The vertical stresses at the footing (z= 0.0 m) and the top of the RI (z=-1.0 m) are shown in Fig. 2.15. It can be observed that the stress distribution increases near the inclusion's

edges. Furthermore, the central inclusion experiences the highest stress, of value 1690 kPa.

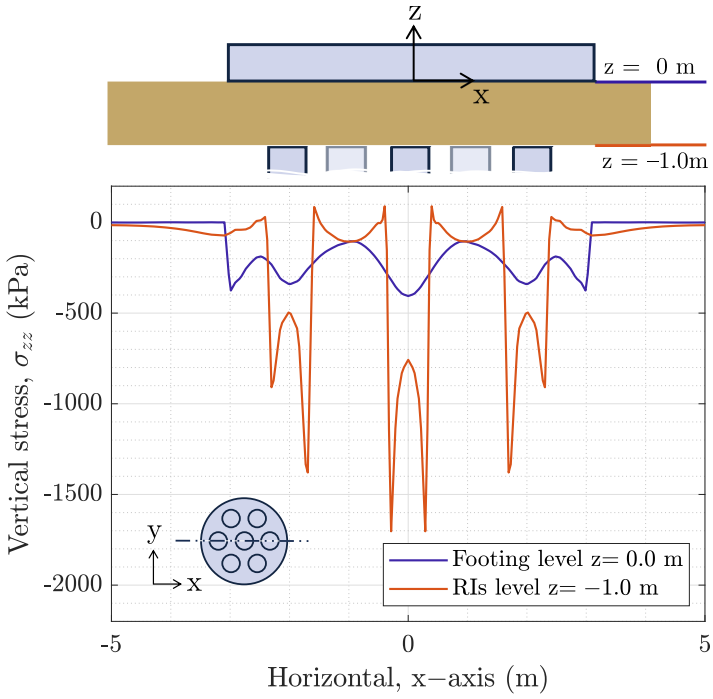

FIGURE 2.15 : Vertical stress distribution in the footing (blue) and at the top of the RI (orange)

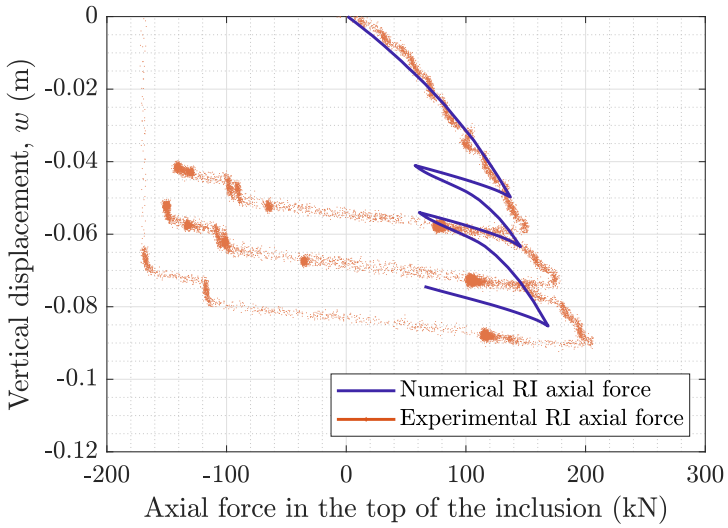

FIGURE 2.16 : Numerical (blue) and experimental (orange) axial forces at the top of the central RI versus vertical displacement of the footing

The determination of the vertical force at the top of the RI needs the integration of stresses from all Gauss points in the whole section. Fig. 2.16 shows the comparison

of the vertical forces at the top of the central RI between the numerical model and the experimental data. The numerical model successfully replicates the monotonic behaviour. Differences appear, however, when loading and reloading are involved; see also Fig. 2.11. This discrepancy can be attributed to the use of force-controlled numerical tests or the absence of a proper interface representation between the RI and their surrounding soil. The introduction of an interface at the soil/RI boundary may capture the reduction in effective radial stress, which in turn results in the loss of shaft friction (Isorna et al., 2017).

2.5 Conclusions

This Chapter introduced a 3D FEM model for foundations with and without RI, validated against recent centrifuge experiments. The accuracy and reliability of the model were rigorously assessed through comparison with the experimental data. Also, discrepancies were examined, guiding refinements in our model.

The soil-RI interaction mechanisms were elucidated, showing different transfer mechanisms involving the transmission of loadings through the arching in the LTP and the frictional interaction between the inclusions and the soil. Significant soil vertical displacements compared to RI vertical displacements at the upper portion of the inclusion shaft. This transition led to the emergence of a neutral plane at a certain depth, aligning with previous experimental observations. Also, the vertical stress distribution to stiffer soil layers through the LTP and inclusions was observed in the model; as a consequence, the soil load-bearing capacity is significantly increased. The results demonstrate the capability of the FEM model to simulate the complex nonlinear mechanisms of a RI foundation accurately.

By extrapolating the insights acquired in this Chapter and the two benchmarks (Appx. A and Appx. B), a robust framework for predicting the behaviour of RI foundation under varying load scenarios is established. Consequently, this 3D FEM model will be used in the next Chapter to develop a novel failure envelope of a RI foundation.

Chapitre 3

Failure envelope of a RI foundation

This Chapter presents the procedure for identifying the 3D failure envelope of a RI foundation by means of swipe tests and FEM models. A parametric study of the influence of geometry and material properties on the failure envelope is carried out, and analytical formulas are proposed, ready to use for engineering practitioners.

3.1 Introduction

Understanding the bearing capacity of foundation-soil systems under various loading conditions has significantly improved in recent decades. Actually, there has been an increasing trend of describing the capacity under vertical (V), horizontal (H), and moment (M) using failure envelopes (*i.e.*, bearing capacity diagrams) that delimit a locus of admissible forces in the 3D $V-M-H$ load space (Butterfield, 1980; Gourvenec and Randolph, 2003). Experimental and numerical solutions of bearing capacity diagrams have been developed for different foundations. See, for example, Sec. 1.7.

Finite Element Method (FEM) models are often used to investigate the ultimate capacity of shallow foundations under combined loading (*e.g.*, Taiebat and Carter, 2000; Loukidis and Salgado, 2009; Tistel et al., 2020; Suryasentana et al., 2020; Ko et al., 2022). In the present Chapter, we extend the approach to the limit states of a RI foundation under combined $V-M-H$ loading with the final objective to introduce a novel analytical formula, ready to use for engineering practitioners.

The Chapter includes the following Sections (i) a presentation of the numerical procedure to determine the 3D failure envelope by means of swipe tests, (ii) validation of the methodology for a foundation on cohesionless soil, (iii) investigation of the failure envelope for a RI foundation, (iv) description of the bearing capacity diagram by a novel analytical formula, (v) investigation on the failure mechanism under combined loading of a foundation with and without RI, (vi) a parametric study of the failure envelope for different material and geometrical characteristics.

3.2 Numerical procedure to determine the 3D failure envelope

3.2.1 Swipe tests

Swipe tests are often applied to construct the failure envelope of a foundation system. The procedure is based on experimental or numerical *displacement-controlled tests* and allows direct investigation of the shape and size of the failure surface for a given foundation. They were first introduced experimentally using centrifuge tests by Tan (1990) to investigate the $V - H$ failure envelope of a shallow foundation and subsequently adopted for other experimental studies, for example, Gottardi and Butterfield (1993); Martin (1994); Gottardi et al. (1999); Byrne (2000) and Martin and Houlsby (2000).

Analogies between swipe tests and hardening plasticity theory applied in critical state soil-mechanics (Schofield and Wroth, 1968) are identified. In swipe tests, the response of foundations under various loads by displacement-controlled tests is explored. The load path effectively traces along the contours of the failure envelope, just as materials undergoing plastic deformation in hardening plasticity theory exhibit similar characteristic stress-strain paths, see Tan (1990); Gottardi and Butterfield (1993); Grange (2008) or Sakellariadis (2021).

In the following, the sign conventions for the loads (V, M, H) and the vertical displacements, the rotations and the horizontal displacements (w, θ and u, respectively) are presented in Fig. 3.1, based on Butterfield et al. (1997).

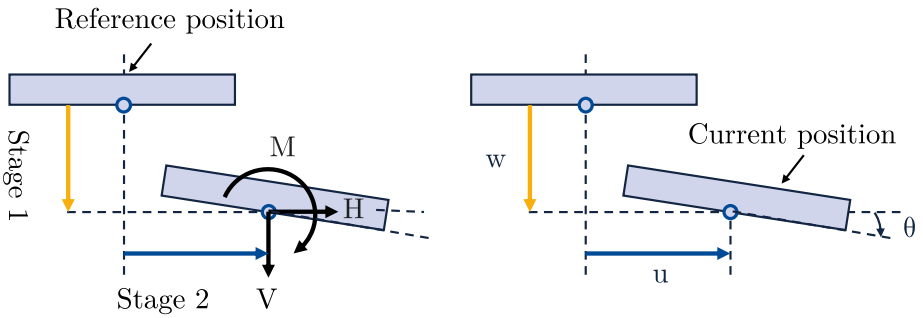

FIGURE 3.1 : Swipe tests: sign conventions, vertical and horizontal applied displacements, adapted from Butterfield et al. (1997)

The vertical component acting downward as compressive force, the clockwise bending moment and the horizontal component acting to the right are all considered positive. The load reference point is located at the centre of the base of the foundation, as shown in Fig. 3.1.

With few simulations, numerical swipe test analyses allow establishing the footing failure locus in the $V - M - H$ space. The different stages adopted to perform the swipe tests numerically are described hereafter:

- Stage 1: an initial vertical displacement w_0 is applied until the foundation reaches a vertical loading level V_0 (where V is positive and M and H are zero). The vertical displacement is then stopped (see stage 1 represented in yellow in Fig. 3.1);
- Stage 2: a monotonically increasing horizontal displacement and/or rotation is imposed on the foundation. For example, the foundation can be driven purely horizontally. A horizontal load then develops, and usually, some moments. As the horizontal load increases, the vertical load decreases, so the load sweeps a path in the $V - H$ space along with the failure envelope (stage 2 represented in blue in Fig. 3.2).
- By assuming the same maximum vertical displacement w_0 and tracking the load paths generated by multiple combinations of horizontal displacements, u, and rotations, θ, the final 3D failure envelope (for the given w_0) can be obtained.

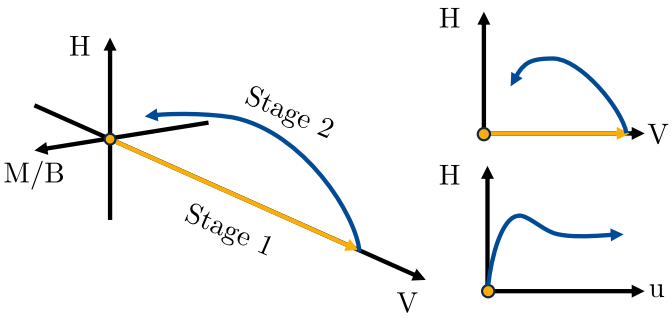

FIGURE 3.2 : The different stages adopted to numerically perform the swipe tests, from Butterfield et al. (1997)

3.2.2 Validation of the numerical procedure

To validate our use of the procedure described in Sec. 3.2, swipe tests are conducted hereafter using a 3D FEM model of a shallow foundation on a homogeneous cohesionless soil and the general-purpose, open-source FEM code Cast3M (CEA, 2001). These initial simulations are important, not only to validate the reliability and accuracy of the adopted procedure, but also to understand the effects and improvements brought by the incorporation of RI on a foundation (see Section Sec. 3.6).

Model description

The adopted finite element mesh is the one presented in Sec. 2.3.1. A schematic representation of the 3D FEM model is given in Fig. 3.3, where due to symmetry, only half of the domain is considered.

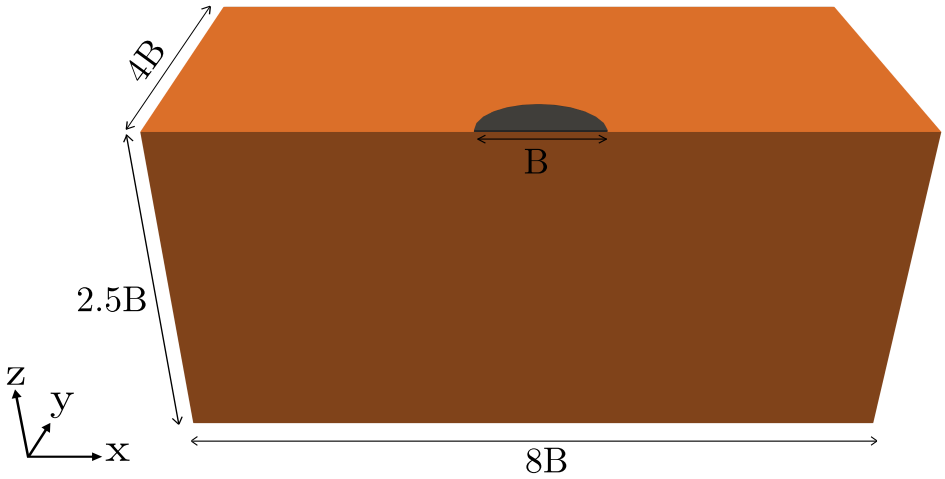

FIGURE 3.3 : 3D FEM model of a shallow circular foundation (without RI)

The model's size is $8B \times 4B \times 2.5B$, with B being equal to 6.0 m to avoid boundary effects. 8-node hexahedral elements (referred to as CUB8 in Cast3M (CEA, 2001)) are employed.

Nodal displacements are fixed in all directions at the base of the FEM model. In the symmetry plan $x - z$ at $y = 0$, the imposed symmetry conditions imply that the normal displacements to the plane are constrained to be zero (Demkowicz, 1991). Displacements at the other lateral boundaries are blocked in normal directions. No slippage is allowed between the foundation and the soil. This condition translates the realistic hypothesis that the concrete and the soil interface is rough enough to create some degree of bonding (Loukidis et al., 2008).

The footing is supposed to be weightless and rigid, with a higher elastic modulus than the soil modulus. The soil is homogeneous and cohesionless ($c = 0$) with a friction angle $\varphi = 30°$, a dilatancy angle $\psi = 2.5°$, a Poisson's ratio $\nu = 0.3$, a Young's modulus $E = 100$ MPa and a density $\rho = 1920$ kg/m^3. These parameters were chosen to match the calibrated experimental results of the sand, as shown in Fig. 2.8. A Drucker-Prager criterion is adopted with a non-associated flow rule, carefully calibrated to match the classical Mohr-Coulomb model (Alejano and Bobet, 2012).

Comparison between literature and numerical results

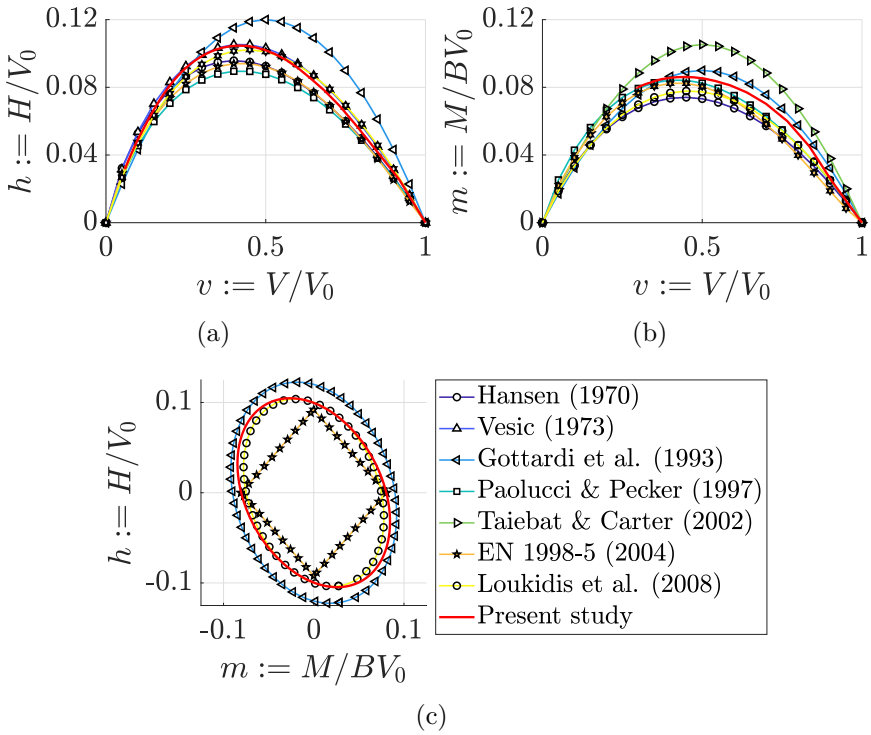

FIGURE 3.4 : Normalised failure envelope of a shallow foundation (without RI): comparison between the results of numerically reproduced swipe tests and existing solutions in the literature (a) $v-h$ (b) $v-m$ and (c) $m-h$ loading planes

Results are presented using non-dimensional variables. The non-dimensional forces are scaled by the bearing capacity corresponding to a purely vertical load, denoted as V_0, as follows:

$$v := \frac{V}{V_0} \qquad m := \frac{M}{B \cdot V_0} \quad \text{and} \quad h := \frac{H}{V_0} \tag{3.1}$$

The normalised $v-h$, $v-m$ and $m-h$ failure envelope planes of the numerically reproduced swipe tests and existing solutions in the literature for a shallow foundation (without RI) are compared in Fig. 3.4. The $m-h$ envelope plane is presented for a normalised vertical load $v = 0.5$. Numerical results agree with existing solutions in the literature for circular shallow foundations (Gottardi and Butterfield, 1993; Taiebat and Carter, 2002) and strip foundations (Hansen, 1970; Vesic, 1973; Paolucci and Pecker, 1997; EN1998-5, 2004; Loukidis et al., 2008). It is therefore concluded that the 3D FEM model and the numerical swipe test procedure are validated. Sec. 3.3 adopts the same approach to identify the 3D failure envelope of a RI foundation.

3.3 Numerical 3D failure envelope

The swipe test methodology described and validated numerically in Sec. 3.2 is employed hereafter to numerically construct the 3D failure envelope of a RI foundation. The validated 3D FEM model from Sec. 2.3.1 is adopted, and the model parameters are given in Tab. 2.5.

First, a monotonic vertical displacement controlled test is done to the foundation to identify the maximal vertical force V_0 and the corresponding vertical displacement w_0. Fig. 3.5 (a) shows the results in a vertical displacement-force graph (blue line). As the displacement-force graph does not show a visible failure, the maximal vertical bearing capacity is approximated employing the tangent intersection method (Hirany and Kulhawy, 1988). This value is calculated as the intersection of two tangents, represented in black lines, corresponding to the initial and steepest portion of the first and second part of the curve, respectively. V_0 is shown as a red dot, and it is found equal to 4593 kN. For more information about V_0, please refer to Appx. C.

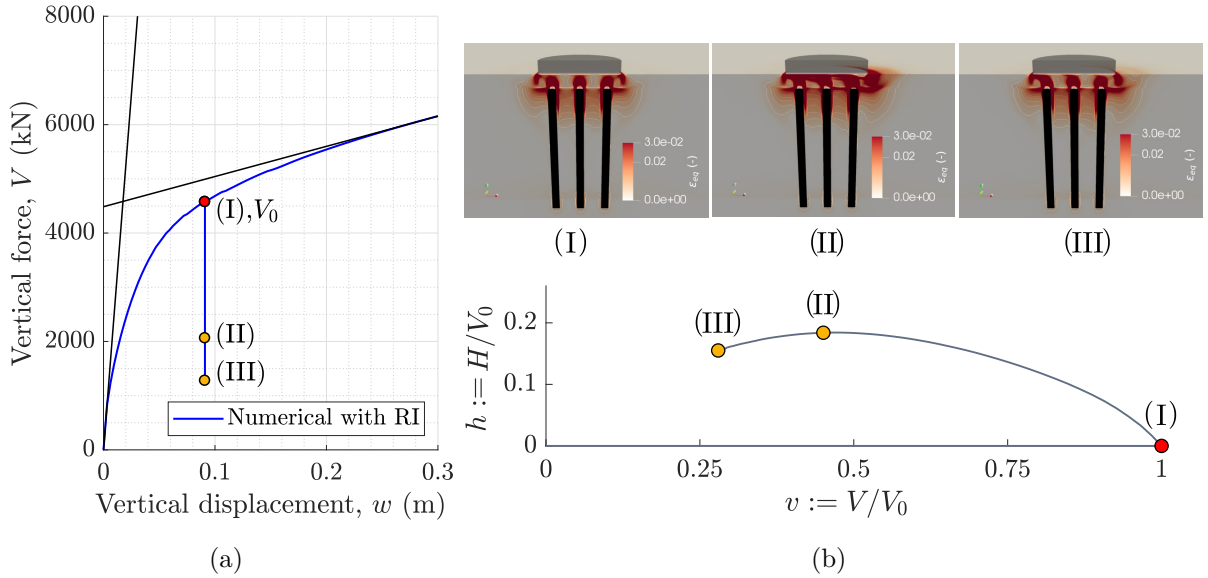

FIGURE 3.5 : (a) Vertical displacement-load curve (blue line). Calculation of the maximal bearing capacity, V_0 (red dot), by the tangent intersection method (black lines) Hirany and Kulhawy (1988). (b) Failure mechanism in the normalised $v-h$ plane at (I) maximum vertical bearing capacity, (II) maximum horizontal normalised force and (III) end of the swipe test. The three figures at the top show the distribution of the equivalent strain ε_{eq} (max value showed at 0.03)

An example of a purely horizontally driven swipe test and the evolution of the corres-

ponding failure mechanism can be visualised by plotting the equivalent strain, ε_{eq} [1], at specific load steps. ε_{eq} is illustrated in Fig. 3.5 (b), for three steps zones in the normalised $v-h$ plane: (I) at maximum vertical bearing capacity, (II) at maximum horizontal normalised force and (III) at the end of the swipe test.

In Fig. 3.5 (b), it can be observed that the vertical load is transferred to the RI through the LTP, and simultaneously, the vertical force applied to the RI is transferred to the stiff soil layer. The principal failure mechanisms are presented in the LTP. The RI are not solicited for a purely horizontal swipe test.

The 3D failure envelope, resulting from the combination of sixty-two independent numerical swipe tests, is shown (in grey dots) in the $v-h-m$ normalised space in Fig. 3.6. The elliptical shape in the $m-h$ plane is shown in yellow dots for a normalised vertical force $v=0.5$.

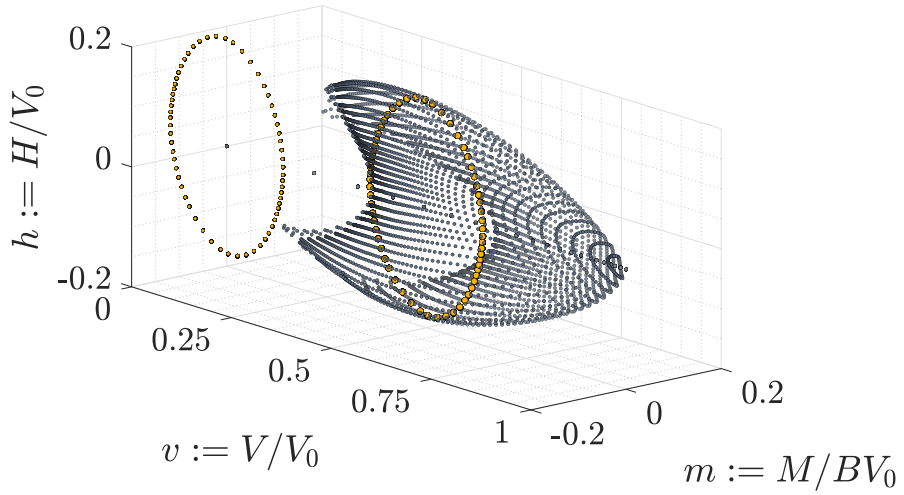

FIGURE 3.6 : Failure envelope of a RI foundation obtained from sixty-two numerical swipe tests. The representation of a cut in the $m-h$ plane is shown in yellow for $v=0.5$

3.4 Analytical 3D failure envelope

This section aims to approximate the numerically reproduced failure envelope of a RI foundation presented in Sec. 3.3 with an appropriate closed-form mathematical formulation in the $V-M-H$ space. Using the normalised notations, it can be concluded from Fig. 3.6 that in the:

- moment-horizontal force plane $m-h$: results have the form of an inclined ellipse centred at the origin;

1. $\varepsilon_{\text{eq}} = \sqrt{\frac{1}{2}[(\varepsilon_x-\varepsilon_y)^2+(\varepsilon_y-\varepsilon_z)^2+(\varepsilon_z-\varepsilon_x)^2+6(\gamma_{xy}^2+\gamma_{yz}^2+\gamma_{xz}^2)]}$

- vertical-horizontal force plane $v - h$: the failure envelope has a parabolic form; its size increases with the vertical force up to a critical point close to $v = 0.45 - 0.5$, also seen in Fig. 3.5 (b), while a decreasing trend is observed afterwards.

From the observations above, the main idea is

(i) to use the inclined ellipse general equation in the $m - h$ plane and to calibrate the three parameters (a, b, c) :

$$ay^2 + bz^2 + cyz - a^2b^2 = 0 \tag{3.2}$$

with the numerical results corresponding to the critical point of the vertical force, taken hereafter equal to $v = 0.5$;

(ii) to use the parabola of the form:

$$y = 4x(1 - x) \tag{3.3}$$

with a peak value equal to 1 at 0.5 and being 0 at 0 and 1, to automatically control the different ellipses' size in the planes $v - h$ and $v - m$.

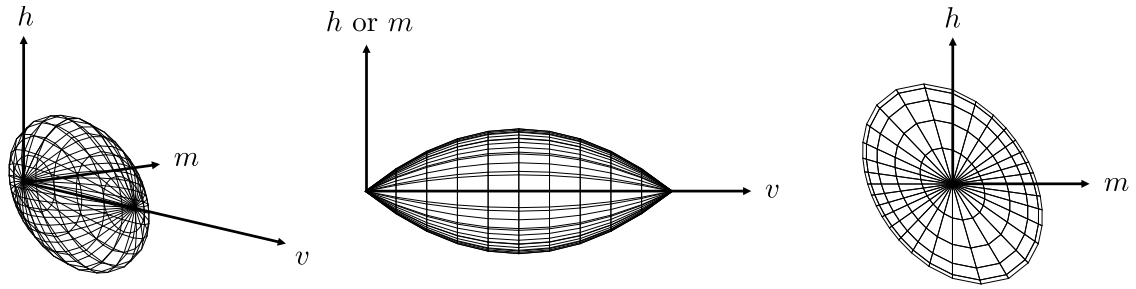

FIGURE 3.7 : Representation of the 'Rugby ball shape' in the different normalised planes

The 'Rugby ball shape', used in the literature for shallow foundations on sand (Nova and Montrasio, 1991; Gottardi and Butterfield, 1993; Cassidy, 1999; Gottardi et al., 1999; among others), is therefore adopted hereafter. The complete expression, in terms of normalised loads, becomes:

$$f(v, m, h) = \frac{m^2}{m_0^2} + \frac{h^2}{h_0^2} - 2a_0\frac{mh}{m_0h_0} - [4v(1 - v)]^2 = 0 \tag{3.4}$$

where m_0 and h_0 determine the failure envelope shape and size and represent the intersection of each ellipse in the normalised $v - m$ and $v - h$ planes, respectively and a_0

represents the cross-section tilt angle in the $m-h$ plane, measured from the h axis. The representation of Eq. 3.4 is given by Fig. 3.7 in the different normalised planes.

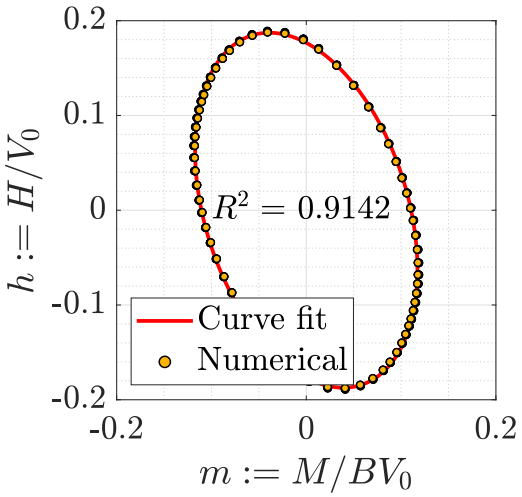

FIGURE 3.8 : Curve fitting of the numerical data using the direct least square fitting of ellipses (Fitzgibbon et al., 1999; Chernov, 2023). Failure envelope obtained from sixty-two numerical swipe tests. The representation of a cut in the $m-h$ plane is shown in yellow for $v = 0.5$

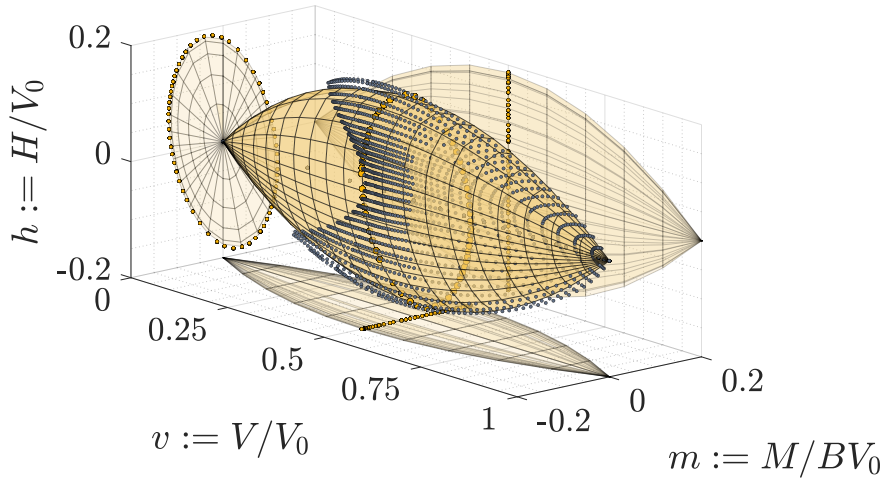

FIGURE 3.9 : Normalized failure envelope of a RI foundation in $v-m-h$ space. Proposed analytical formula (yellow) and numerical swipe test results (grey dots)

In Fig. 3.8, the representation of a cut in the $m-h$ plane from the sixty-two numerical swipe tests is shown in yellow dots for $v = 0.5$. The direct method for least square fitting of ellipses (Fitzgibbon et al., 1999; Chernov, 2023) is employed to calibrate the ellipse in the $m-h$ plane at $v = 0.5$, shown in a red curve. The three parameters $h_0 = 0.1766$,

$m_0 = 0.1105$ and $a_0 = -0.3325$ are estimated. A correlation factor of $R^2 = 0.9142$ is calculated.

The shape of the analytical expression of Eq. 3.4 using the obtained parameters is represented in Fig. 3.9 as a yellow surface, together with the numerical swipe test results as grey dots. A good agreement can be observed, evidencing that the suggested simplified formula is suitable for design purposes and the development of simplified modelling strategies, such as novel macroelements.

3.5 Comparison with the Eurocode

No simplified method exists to calculate the bearing capacity of a RI foundation under complex coupled loads (Frattini et al., 2017). Current engineering practice often circumvents this problem by adopting the bearing capacity formulas of an unreinforced shallow foundation. To check the validity of this assumption, the 3D failure envelope of Eq. 3.4 is compared with the semi-empirical formula (EN1998-5, 2004) for a shallow foundation (without RI) on a homogeneous soil of Eq. 1.9, Fig. 3.10. The parameters a, b, c, d, cT, cM, β and γ depend on whether the foundation ground is purely cohesionless or cohesive and can be found in Tab. 1.2.

In Fig. 3.10, the green and blue curves represent the normalised bearing capacity of a shallow foundation without RI in the $v-h$ and $v-m$ plane, and at $v = 0.5$ for the $m-h$ plane for a cohesionless and a cohesive soil respectively. The red curves represent the normalised bearing capacity of a RI foundation using numerical swipe tests, and the yellow curves represent the analytical equation Eq. 3.4. The following observations can be made for foundations with or without RI:

(i) for all load combinations, the bearing capacity of a shallow foundation without RI is higher when resting on a cohesive than a cohesionless soil, Fig. 3.10;

(ii) in the $v-h$ plane, the bearing capacity of a shallow foundation without RI on a cohesive soil is significant even for low vertical forces, Fig. 3.10 (a);

(iii) in the $v-m$ plane, the bearing capacity of a shallow foundation without RI resting on a cohesive soil is almost 2 times bigger than on a cohesionless soil, Fig. 3.10 (b);

(iv) for almost all load combinations, the bearing capacity of a RI foundation is between the bearing capacity of a shallow foundation without RI resting on a cohesive and a cohesionless soil, Fig. 3.10;

(v) in the $v-m$ plane, for $v < 0.3$, the bearing capacity of a foundation with or without RI is similar, Fig. 3.10 (b);

(vi) As observed in Fig. 3.10, for $0.5 < v$ values, the foundation without RI in cohesive soil presents a more important size. Hence, relying on the bearing capacity envelope of a shallow foundation to design a foundation with RI can be unsafe.

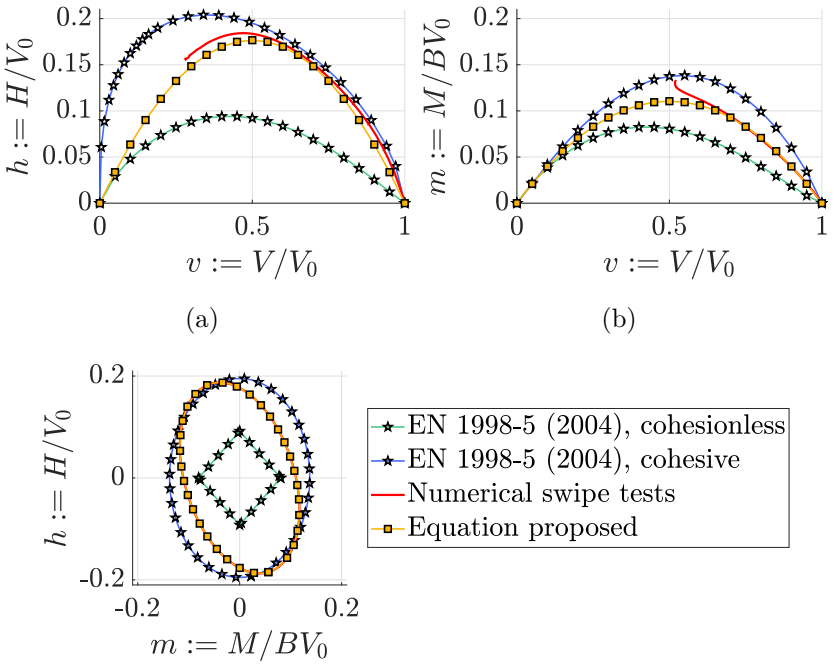

FIGURE 3.10 : comparison between the Eurocode 8 EN1998-5 (2004) existing solutions for a shallow foundation on a cohesionless and cohesive soil, the numerical swipe tests (Eq. 3.3), and Eq. 3.4 for a RI foundation. Results are shown in the normalised failure envelope in the (a) $v-h$ and (b) $v-m$ plane and at $v = 0.5$ for the (c) $m-h$ plane

The existing solutions on unreinforced shallow foundations involve multiple simplifications, to get a better insight into the behaviour of a foundation with or without RI, a FEM numerical study on the different failure envelopes is presented in the next Section.

3.6 Failure envelopes for a foundation with and without RI

This Section compares the failure envelopes for a foundation with and without RI using FEM calculations. It aims to observe the influence of the RI on the failure envelopes in

the $V-M-H$ space. The validated models from Chapter 2 are used. The same boundary conditions and finite element meshes are used for the two foundations, the only difference being the presence of RI, as shown in Fig. 2.7. The material properties and the constitutive models are summarised in Tab. 2.5.

The procedure described in Sec. 3.2 is again employed to construct the failure envelopes. The maximal bearing capacity for each case is calculated in Appx. C. By normalising the results with the V_0 of each case, the failure envelopes parameters (described in Eq. 3.4) are found and summarized in Tab. 3.1.

TABLE 3.1 : Parameters of the failure envelopes for a foundation with and without RI

Case	V_0 (kN)	h_0	m_0	a_0
with RI	4593	0.1766	0.1105	-0.3325
without RI	2399	0.2604	0.1435	-0.2536

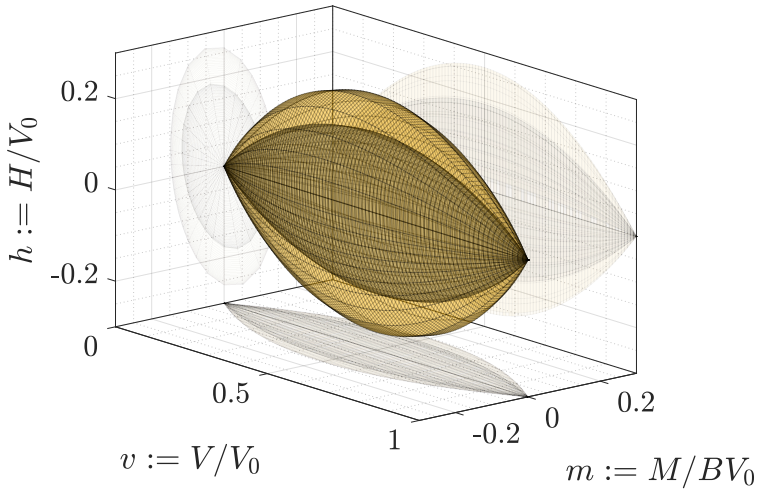

FIGURE 3.11 : Normalised failure envelopes for a foundation with (grey) and without RI (yellow)

The normalised failure envelopes are shown in Fig. 3.11 for the foundation with (grey) and without RI (yellow). From these normalised representations, it is noticed that the unreinforced foundation performs better than the RI foundation for all the v values.

In the case of the unreinforced foundation, the LTP is sufficiently small compared to the soft soil. So, it can be seen as a shallow foundation on cohesive soil. So the results illustrated in Fig. 3.11 are expected as they agree with what is observed in existing solutions for cohesive soils; see Fig. 3.10.

To clearly observe the influence of the RI on the failure envelopes, the unnormalised failure envelopes in the $V-M/B-H$ space are presented in Fig. 3.12. In this unnormalised representation, the previously observed tendency is only present for small values of vertical forces $V \leq 1150$ kN.

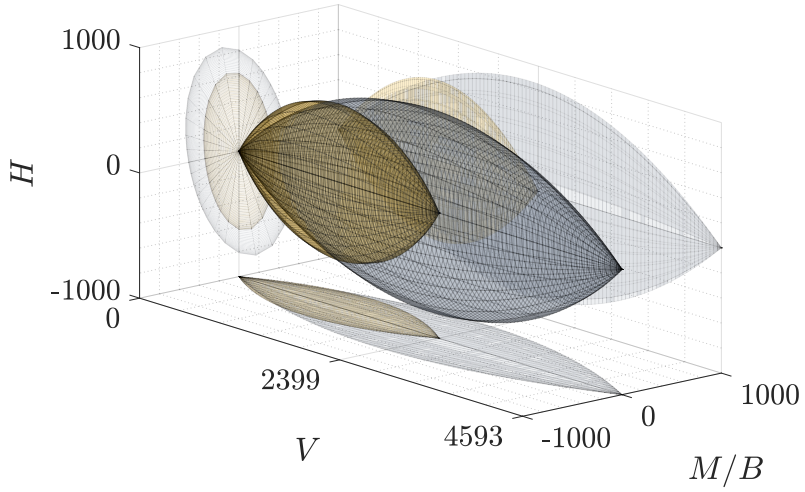

FIGURE 3.12 : Unnormalised failure envelopes for a foundation with (grey) and without RI (yellow)

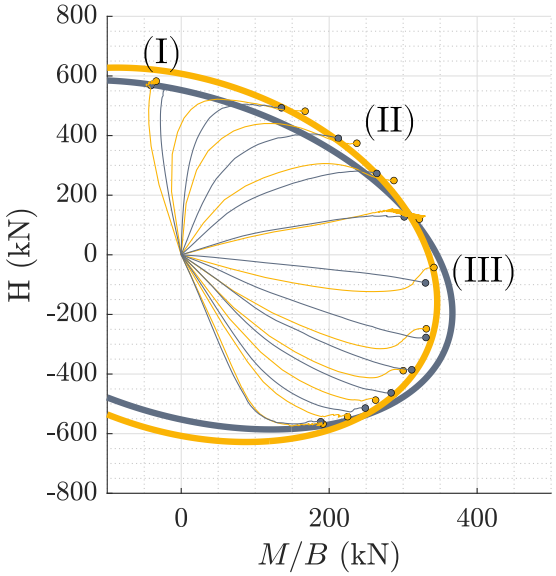

FIGURE 3.13 : Eleven displacement-probe test combinations to describe the $M/B-H$ positive plane for a fixed $V = 1000$ kN. Grey and yellow colours represent the foundation with and without RI, respectively. In bold and thin lines, the failure envelope is described by means of swipe tests and displacement-probe tests, respectively.

The results showed in Fig. 3.12 might appear counterintuitive as we expect the RI foundation resist better to loadings. To get a better insight into the behaviour of the foundation with and without RI, we use the *displacement-probe* test (Bransby and Randolph, 1997) to identify some yield points in the failure envelope, see Sec. 1.7.2 for more information.

Fig. 3.13 illustrates eleven combinations of displacement-probe tests representing the $M/B - H$ positive plane for a constant vertical load of $V = 1000$ kN. Similar to previous figures, grey and yellow colours indicate the foundation with and without RI, respectively. The bold lines depict the failure envelope determined through swipe tests, while the results from the displacement-probe tests are shown in thin lines, concluding with a final yield point marked by a dot.

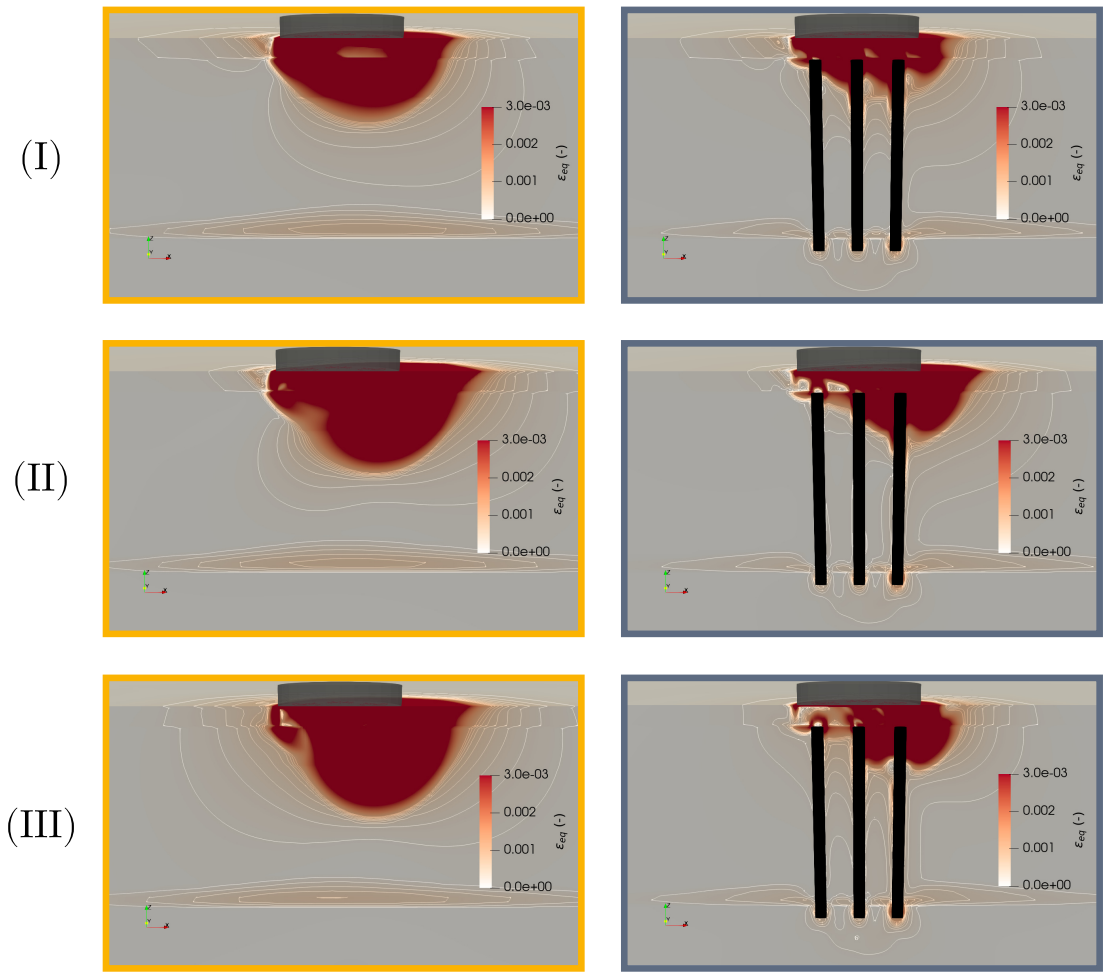

FIGURE 3.14 : Failure mechanisms under combined loadings are shown in grey and yellow frames, representing the foundation with and without RI, respectively. They are presented through the equivalent strain, ε_{eq}, with a maximum value of 0.003.

From Fig. 3.13, it becomes evident that the probe tests yield results comparable to the swipe tests. The figure supports the observation that the foundation without RI performs the same way under different loading conditions, at low V values, compared to the RI foundation. To further analyse these outcomes, three specific yield points, denoted as (I), (II), and (III) in the figure, are examined to understand the underlying failure mechanism.

The failure mechanisms are depicted through contour plots of equivalent strain, ε_{eq}, in Fig. 3.14, where the maximum value is indicated at 0.003. In the case of an unreinforced foundation, the failure pattern is characterized by a semicircular "scoop" shape, as described by Gourvenec (2007). This scoop surface penetrates the soft layer because the LTP transfers a significant portion of the horizontal/moment load into the soft layer before the LTP's collapse load is fully mobilised. Similar findings in stiff soil over soft clay are reported in Ko et al. (2022).

In the case of a RI foundation, Fig. 3.14 shows that the scoop surface predominantly lies within the LTP. This occurs because the presence of RI creates a stiffer layer, preventing the failure surface from extending through it. However, under higher vertical forces, there is a noticeable expansion of the bearing capacity. This expansion becomes more prominent as the loadings are also distributed to the stiffer bottom layer through the RI.

Swipe tests tend to underestimate the failure envelope at low v values. To obtain a more precise description of the failure envelope, additional swipe tests at varying v initial values are necessary. However, swipe tests offer a favourable balance between time and effort, as they delineate the admissible limit surface in a plane with just one test. In the next Section, these tests will be used to analyse how different parameters influence the failure envelope.

3.7 Influence of the geometry and of the LTP material properties

This Section focuses on the influence of the geometry and of the LTP parameters on the 3D failure envelope of RI foundations. An extensive numerical analysis is conducted to delve deeper into the system response using a statistical technique for the sampling of parameters.

The reference model is the one presented in Sec. 2.3 having a diameter of RI of d = 0.60 m, corresponding to a coverage area $\alpha = 7.0\%$, a LTP thickness of $H_{LTP} = 1.0$ m and a friction angle of $\varphi_{LTP} = 36°$. The other model parameters are listed in Tab. 2.5 and the material variation ranges in Tab. 3.2.

The used sampling technique corresponds to the Latin Hypercube Sampling (LHS) (McKay et al., 1979), used to determine a multi-dimensional parameter space more efficiently and more representative than traditional random sampling methods (Stein, 1987). Its fundamental objective is to establish a uniformly distributed sampling regimen within the expanse of the parameter space. This uniform sampling is achieved through the partitioning of the range of each parameter into equidistant intervals, followed by the stochastic selection of a single sample from each interval. The *Latin* aspect from LHS comes from the idea that the sample point is chosen in each interval such that it does not coincide with the sample points from other intervals along the same parameter, helping spread out the samples.

TABLE 3.2 : Parameters and their variations

Input parameter	Symbol	Unity	Reference model	Range
Diameter of RI	d	(m)	0.6	$0.36 - 0.6$
Coverage area	α	(%)	7.0	$2.5 - 7$
LTP thickness	H_{LTP}	(m)	1.0	$0.5 - 1$
LTP friction angle	φ_{LTP}	(°)	36	$30 - 42$

The parametric space consists of 120 scenarios. First, a first sampling space is generated by maintaining the original configuration and varying only one parameter at a time, resulting in a total of sixty linear combinations, as shown in Fig. 3.15. For instance, twenty diameters of RI (from 0.36 m to 0.6 m, corresponding to a coverage area, α, of 2.5% to 7.0% depicted as red dots) are diversified while the other two parameters from the reference model ($H_{LTP} = 1.0$ m, $\varphi_{LTP} = 36°$) remain constant. Similarly, twenty LTP thickness, H_{LTP}, (from 0.5 to 1.0 m, blue dots) and twenty LTP friction angles, φ_{LTP} (from 30° to 42°, yellow dots) are independently applied. Second, sixty other intermediate combined scenarios are employed using the LHS technique. The three parameters are generated in the combined space $H_{LTP} - \varphi_{LTP} - \alpha$, represented in grey dots, Fig. 3.15.

By following the procedure described in Sec. 3.2, a vertical bearing capacity study for each of the 120 combinations ($i = 1, 120$) is first done to evaluate the maximal vertical displacement, $w_{0,i}$ and force $V_{0,i}$ for each case. The construction of the failure envelope is then completed through numerical swipe tests. Taking advantage of the symmetry found in the failure envelope shape (see Fig. 3.6) and in order to limit the computational time, only eleven swipe tests are carried out for each case i (instead of the original sixty-two).

Calculations are made with the computer cluster "Liger"of the Centrale Nantes Super-Computing Center (a BULL/Atos DLC720 cluster of 252 compute nodes and 14 visualisation nodes with 24 cores per node and a total compute memory of 36608 GB). Adopting a node with 24 cores, the average computation time for each case is approximately 80 min for the vertical bearing capacity test and 1900 min for the complete failure envelope description. This process yields a total of 120 sets of predicted output results containing the m_0, h_0 and a_0 values to characterise the failure envelopes.

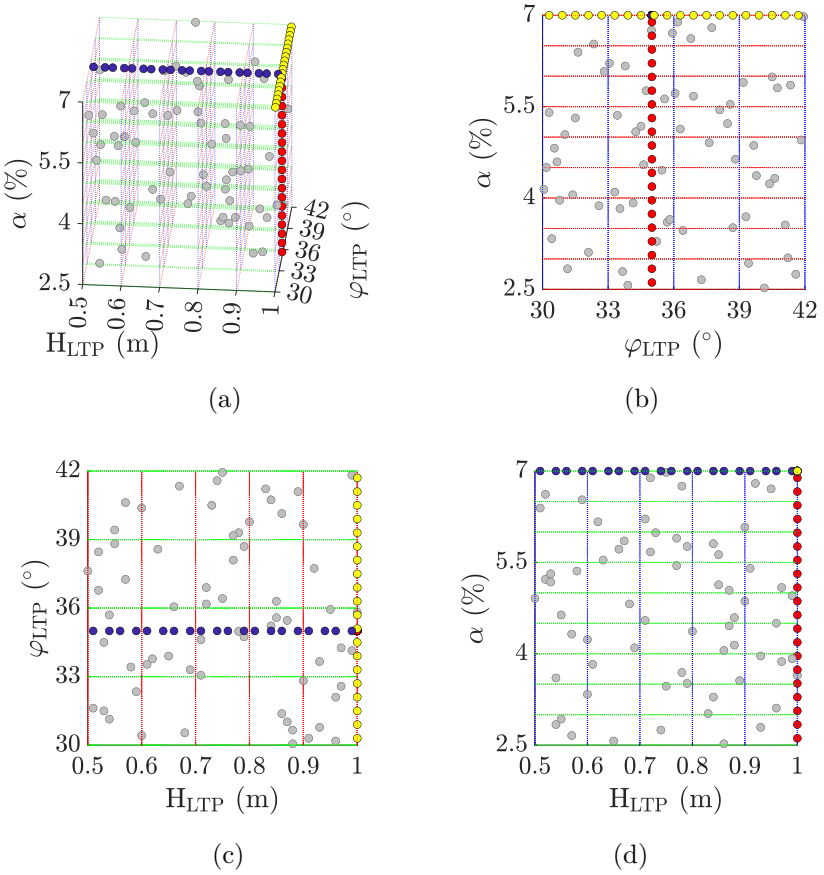

FIGURE 3.15 : Parametrical numerical study: variation of the coverage area α (red dots), the LTP thickness H_{LTP} (blue dots), the LTP friction angle φ_{LTP} (yellow dots) and combined effects (grey dots) in the (a) H_{LTP} - φ_{LTP} - α; (b) φ_{LTP} - α; (c) H_{LTP} - φ_{LTP}, and (d) H_{LTP} - α planes

The discussion of results mainly focuses on the yield locus size and inclination. The results of the simulations on the $m-h$ plane at $v=0.5$, normalised by the $V_{0,i}$ of each case, are shown in Fig. 3.16. The results from variations of the Fig. 3.16 (a) coverage area, α, are shown in red, $i=1-20$; Fig. 3.16 (b) LTP thickness, H_{LTP}, in blue, $i=21-40$; Fig. 3.16 (c) LTP friction angle, φ_{LTP}, in yellow $i=41-60$; and Fig. 3.16 (d) combined effect, in grey, $i=61-120$.

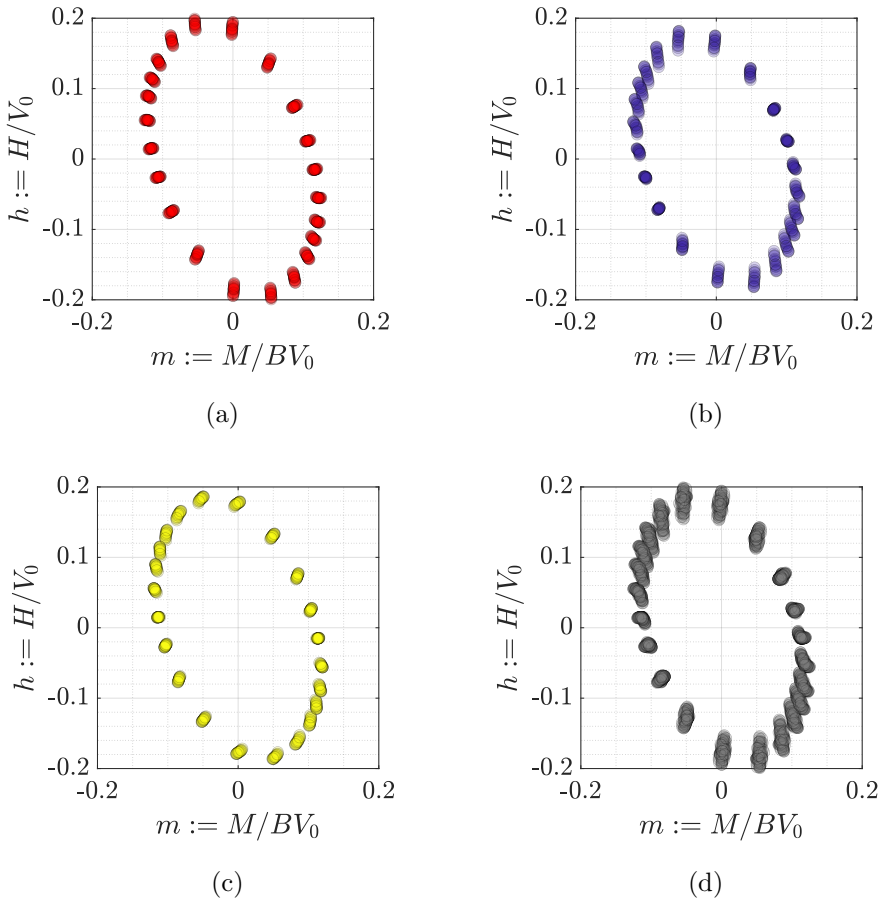

FIGURE 3.16 : Normalised failure envelopes shapes in the $h-m$ plane at v=0.5 varying the (a) coverage area, α, (b) the LTP thickness, H_{LTP}, (c) the LTP friction angle φ_{LTP} and (d) considering combined effects

The main observations are presented:

(i) The shape of the failure envelope (slightly) increases when the covering area α is reduced, Fig. 3.16 (a). The observations from Fig. 3.14 may explain this. The failure mechanisms developed with smaller RI diameters are bigger in size because the *scoop* surface, introduced in the previous Section, can be extended through the soft soil.

(ii) The shape of the failure envelope increases with increasing LTP thickness H_{LTP}. Although a higher LTP thickness does not necessarily result in a higher vertical bearing capacity, the increased normalised horizontal force, Fig. 3.16 (b), can be attributed to the expansion of the failure mechanism area in the LTP, as shown in Fig. 3.5.

(iii) Variations of the LTP friction angle φ_{LTP}, Fig. 3.16 (c), have a minor impact on the

shape of the failure envelope. Thus, the fact that in current engineering practice, this parameter is often omitted is justified (see Sec. 3.5).

(iv) Combined effects have a more significant impact on the shape of the failure envelope than each parameter alone, Fig. 3.16 (d).

(v) The inclination of the failure surface stays (almost) constant.

The influence on the vertical bearing capacity, V_0, by the parameters, can be observed in Fig. 3.17. In the figure, the failure envelope shape at v=0.5 varying the (a) LTP thickness H_{LTP} and (b) the LTP friction angle φ are shown. It is observed from Fig. 3.17 (a) that the variation of the LTP thickness does not necessarily lead to an increase in the maximal bearing capacity. This variation is more important for other parameters, for instance, the LTP friction angle; see Fig. 3.17 (b).

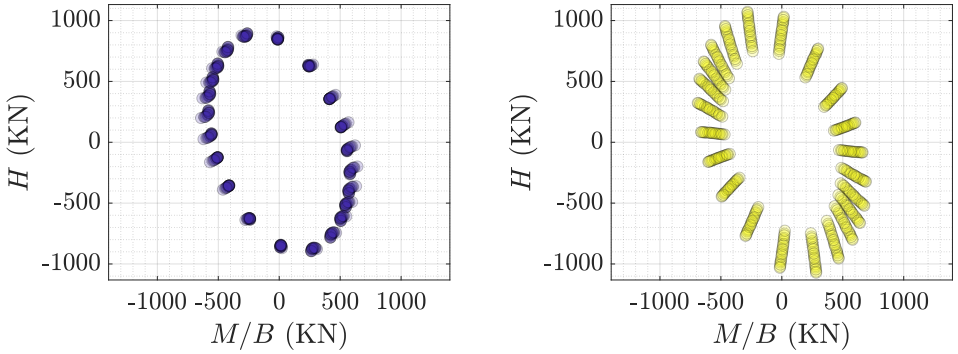

FIGURE 3.17 : Unnormalised failure envelope shapes at v=0.5 varying the (a) LTP thickness H_{LTP} and (b) the LTP friction angle φ_{LTP}

A novel analytical formula is proposed hereafter to describe the geometrical (coverage area and LTP thickness) and LTP material (friction angle) properties effects on the failure envelope:

$$c = a_1 \left[1 + a_2(\frac{\alpha}{H_{LTP}})^2 + a_3(\varphi_{LTP})^2 + a_4(\frac{\alpha}{H_{LTP}}\varphi_{LTP})\right] \tag{3.5}$$

where c represents the parameters h_0, m_0 and a_0 from Eq. 3.4; and a_1, a_2, a_3, a_4 are four constants to identify. In Eq. 3.5, the parameters α, H_{LTP} and φ_{LTP} should be used in a dimensional form, conserving their values in decimals, meters and radians respectively.

The methodology discussed in Sec. 3.4 is once again employed to obtain the parameters $h_{0,i}$, $m_{0,i}$ and $a_{0,i}$ for each case. Then, curve fitting of the numerical data is done using the

direct least square fitting of ellipses (Fitzgibbon et al., 1999; Chernov, 2023). The three parameters controlling the failure envelope shape are obtained from the eleven swipe tests (twenty-two points in the $m-h$ plane due to symmetry). The Least-Squares Fitting Method (Holland and Welsch, 1977; DuMouchel and O'Brien, 1992) in MATLAB® is used to calibrate the constants a_1, a_2, a_3, a_4 in the proposed Eq. 3.5 by employing only the first sixty results, i=1-60, corresponding to one parameter variations (red, blue and yellow dots in Figs. 3.15 and 3.16).

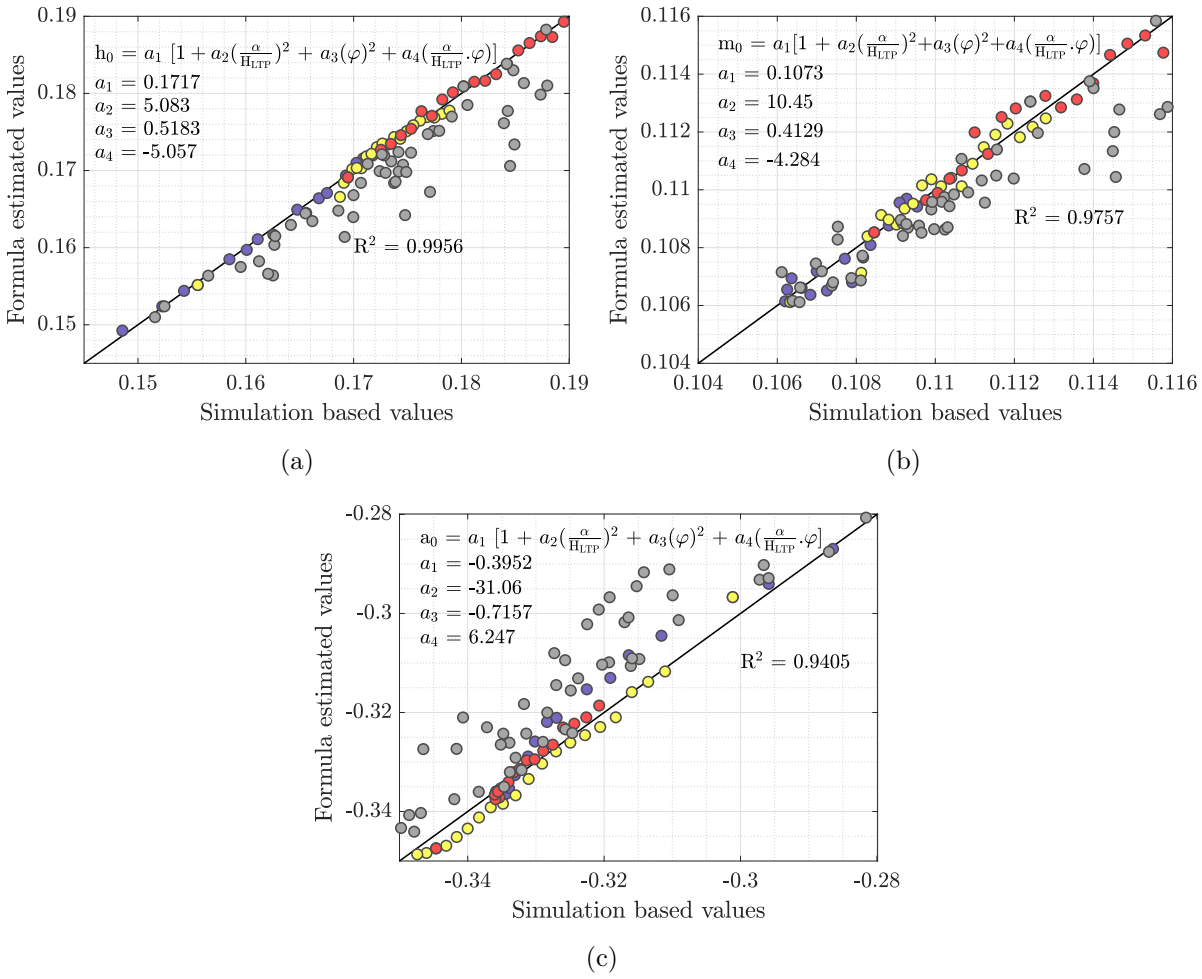

FIGURE 3.18 : Comparison between Eq. 3.5 and the numerical simulations results for: (a) h_0, (b) m_0 and (c) a_0

The comparisons between the proposed formula and the values obtained by the numerical simulations are shown in Fig. 3.18 (a), (b) and (c). The correlation factor, R^2, is estimated equal to 0.9956, 0.9757 and 0.9405 for h_0, m_0 and a_0, respectively, indicating that Eq. 3.5 reproduces the variation of properties effects on the failure envelope satis-

factorily. Fig. 3.18 shows that the formula can also reproduce the influence of combined effects on the failure envelope shape; see grey dots i=61-120. More specifically, the dots on the right side of the inclined line indicate that the proposed equation is conservative in calculating h_0 and m_0, Fig. 3.18 (a) and (b). Although correlation is not satisfactory for a_0, Fig. 3.18 (c), this parameter only affects the inclination of the failure envelope. Therefore, its impact on the failure envelope shape is minimal.

3.8 Synopsis of the proposed analytical formulas

A synopsis of the proposed analytical formulas is given hereafter.

If α is the coverage area, H_{LTP} the LTP thickness, φ_{LTP} the LTP friction angle, V_0 the maximum vertical load, V the vertical force, M the bending moment, H the horizontal force and $v := V/V_0$, $m := M/BV_0$, $h := H/V_0$, the 3D failure envelope of a rigid inclusion foundation has the form:

$$f(v,m,h) = \frac{m^2}{m_0^2} + \frac{h^2}{h_0^2} - 2a_0\frac{mh}{m_0 h_0} - [4v(1-v)]^2 = 0 \tag{3.6}$$

where the applied fitting parameters of h_0, m_0 and a_0 in Eq. (3.6) are estimated by:

$$c = a_1\left[1 + a_2(\frac{\alpha}{\mathrm{H_{LTP}}})^2 + a_3(\varphi_{\mathrm{LTP}})^2 + a_4(\frac{\alpha}{\mathrm{H_{LTP}}}\varphi_{\mathrm{LTP}})\right] \tag{3.7}$$

where α is calculated without dimensions, H_{LTP} in meters, φ_{LTP} in radians. c represents the parameters h_0, m_0 and a_0, and a_1, a_2, a_3, a_4 are summarized in Tab. 3.3:

TABLE 3.3 : Fitting parameters of h_0, m_0 and a_0

c	a_1	a_2	a_3	a_4
h_0	0.1717	5.083	0.5183	−5.057
m_0	0.1073	10.45	0.4129	−4.284
a_0	−0.3952	−31.06	−0.7157	6.247

The main hypotheses and validity domain of the formulas are summarised hereafter:

- A shallow circular rigid foundation.
- Linear elastic behaviour for the shallow foundation and the rigid inclusions.
- A three-layer stratigraphy (LTP+ soft soil + stiff soil) with specific material properties, as described in Sec. 2.3.

- A coverage area α from 2.5% to 7.0%.
- An LTP thickness H_{LTP} from 0.5 m to 1.0 m.
- An LTP friction angle φ_{LTP} from 30° to 42°.
- The maximum size ellipse is calibrated at $v = 0.5$.
- The failure surface is found for the maximum bearing capacity, V_0, defined using the tangent method. It is supposed to be the same for other force levels.

Although calculations were done for a circular foundation, the analytical formulas can be easily modified for other shapes (e.g. rectangular), as proposed in Grange et al. (2009a). For the best fitting, however, the a_1, a_2, a_3, a_4 constants of Eq. 3.5 should be recalculated.

3.9 Conclusions

In this Chapter, we investigated the behaviour of RI foundations under combined vertical (V), horizontal (H), and moment (M) loading conditions. The bearing capacity diagram is reproduced numerically by means of swipe tests. The adopted technique generates a complete yield locus with only a few numerical tests. First, the approach was validated through a simple FEM model compared with literature results. Then, it was used to describe a novel failure envelope for a RI foundation in the $V - M - H$ space.

Distinct mechanisms for foundations with and without RI were observed. In the unreinforced foundation, the failure mechanism is generated inside the soft soil with a scoop shape. For the RI foundation, the presence of RI avoids the development of failure in the stiffened soil, so the failure shape contrasts sharply. In the RI foundation, the failure mechanisms are contained almost entirely in the LTP layer. They, consequently, affect the failure envelope size. Besides, the expansion of the RI foundation bearing capacity under higher vertical forces is illustrated. However, it is not observed for small vertical values.

The analysis of parameters like covering area (α), LTP thickness (H_{LTP}), and LTP friction angle (φ_{LTP}) revealed complex interactions. Combined effects influence the failure envelope shape, offering valuable insights for predicting RI foundation behaviour. Finally, an appropriate closed-form mathematical formulation was proposed, considering the influence of geometrical and material properties on the failure envelope shape. Engineers can use the proposed analytical failure envelope to quantify the bearing capacity of RI foundations under complex 3D loading, and researchers to develop simplified approaches. In the upcoming Chapters, the proposed formula will be used to develop a macroelement for RI foundations.

Chapitre 4

A macroelement for a RI foundation

This chapter presents the plasticity-based framework to develop a macroelement (ME) that reproduces the behaviour of a RI foundation under static and seismic loadings. The elastic and plastic behaviour laws governing the model are introduced using dimensionless variables and follow the ME's formulation for shallow foundations introduced by Cremer (2001) and Grange (2008).

4.1 Introduction

The current practice in the seismic design of rigid inclusions (RI) foundations relies often on conservative methods that consider a linear elastic soil-foundation behaviour. This can be explained as a direct consequence of limited available experimental data and lack of robust simplified numerical tools. In this work, the macroelement approach is adopted to model in a simplified way the complex non-linear response of a RI foundation system.

The macroelement (ME) presented in this manuscript is based on the mathematical theory of plasticity (Hill, 1950; Borja, 2013), the ME concept introduced in geomechanics by Nova and Montrasio (1991) and the existing MEs for shallow foundations developed by Cremer (2001) and Grange (2008). Consider a rigid circular shallow foundation resting on soft soil reinforced by RI as shown in Fig. 4.1. All the nonlinear mechanisms are concentrated in the surrounding soil and the load transfer platform (LTP), while the whole system (shallow foundation, LTP, RI, surrounding soil) is presented as a single point at the footing centre.

The ME approach can be seen as a stress-resultant nonlinear constitutive relationship between the generalised force $\underline{\mathbf{F}}$ and the generalised displacement $\underline{\mathbf{u}}$ vectors. More specifically, the vertical force V, the horizontal force H and the moment M are written in function of the vertical displacement u_z, the horizontal displacement u_x and the rotation θ_y as follows:

$$\underline{\mathbf{F}} = \begin{bmatrix} v \\ h \\ m \end{bmatrix} = \frac{1}{V_0} \begin{bmatrix} V \\ H \\ M/B \end{bmatrix} \qquad \underline{\mathbf{u}} = \begin{bmatrix} w \\ u \\ \theta \end{bmatrix} = \frac{1}{B} \begin{bmatrix} u_z \\ u_x \\ B\theta_y \end{bmatrix} \tag{4.1}$$

where V_0 is the vertical bearing capacity and B the diameter of the circular foundation. v, h, m are the dimensionless forces and w, u, θ the dimensionless displacements at the centre of the footing, see Fig. 4.1. Note that with this type of normalisation, $\underline{\mathbf{F}}$ and $\underline{\mathbf{u}}$ are conjugate; the work of the external forces applied to the foundation can be expressed using these variables (Nova and Montrasio, 1991).

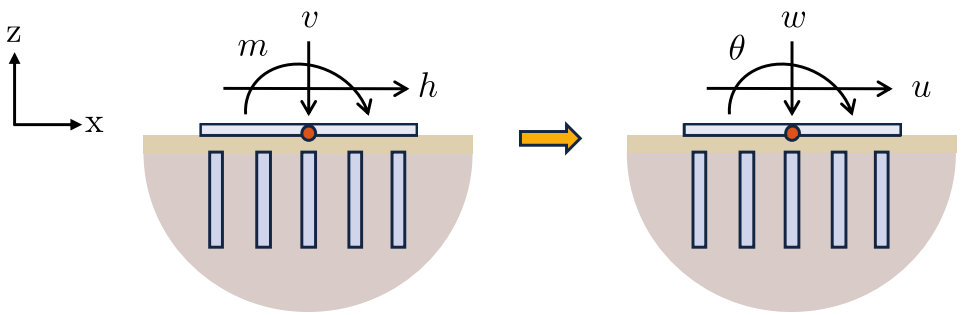

FIGURE 4.1 : Generalised forces and generalised displacements at the footing of a RI foundation

In a similar way as plastic hinges are introduced in plasticity theory the total displacement $\underline{\mathbf{u}}$ is decomposed in an elastic $\underline{\mathbf{u}}^{\text{el}}$ and a plastic part $\underline{\mathbf{u}}^{\text{pl}}$ as follows:

$$\underline{\mathbf{u}} = \underline{\mathbf{u}}^{\text{el}} + \underline{\mathbf{u}}^{\text{pl}} \tag{4.2}$$

The elastic and the plastic behaviours are detailed in Sec. 4.2 and Sec. 4.3 respectively. An extension to dynamic (seismic loadings) problems follows in Sec. 4.4, a synopsis of all the formulas in Sec. 4.5 and the way to calibrate the macroelement parameters in Sec. 4.6. The performance of the new macroelement is finally studied using experimental data in Chapter 5.

Remarks

- The generalised forces and displacements are written in the $x - z$ plane. Adapting the macroelement to a 3D loading for a circular foundation (axial symmetry) is straight forward, see for example Grange (2008).
- Equations are presented for a circular RI foundation. Extension to other foundation's shapes can be made using the approach proposed in Grange (2008).

4.2 Elastic behaviour

The relationship between the load $\underline{\mathbf{F}}$ and displacement $\underline{\mathbf{u}}^{\mathrm{el}}$ in the elastic range can be written as follows:

$$\underline{\mathbf{F}} = \underline{\underline{\mathbf{K}}}^{\mathrm{el}}\underline{\mathbf{u}}^{\mathrm{el}} = \begin{bmatrix} v \\ h \\ m \end{bmatrix} = \begin{bmatrix} k_1 & 0 & 0 \\ 0 & k_2 & 0 \\ 0 & 0 & k_3 \end{bmatrix} \begin{bmatrix} w^{\mathrm{el}} \\ u^{\mathrm{el}} \\ \theta^{\mathrm{el}} \end{bmatrix} \tag{4.3}$$

where $\underline{\underline{\mathbf{K}}}^{\mathrm{el}}$ is the elastic stiffness matrix and the diagonal terms k_1, k_2, k_3 the stiffness associated with the vertical, horizontal and rotational motion, respectively. The coupling terms in the stiffness matrix are neglected, in accordance with the literature results for shallow foundations (Crémer et al., 2001; Salciarini and Tamagnini, 2009; Chatzigogos et al., 2009; Grange, 2008; Grange et al., 2009a, among others).

The incremental form of Eq. 4.3 is written as (where the symbol $[\dot{\cdot}]$ represents the time derivative):

$$\begin{bmatrix} \dot{v} \\ \dot{h} \\ \dot{m} \end{bmatrix} = \begin{bmatrix} k_1 & 0 & 0 \\ 0 & k_2 & 0 \\ 0 & 0 & k_3 \end{bmatrix} \begin{bmatrix} \dot{w}^{\mathrm{el}} \\ \dot{u}^{\mathrm{el}} \\ \dot{\theta}^{\mathrm{el}} \end{bmatrix} \tag{4.4}$$

where the dimensionless forms of the stiffness parameters are given as:

$$\begin{cases} k_1 = \dfrac{k_z^{\mathrm{el}} B}{V_0} \\ k_2 = \dfrac{k_x^{\mathrm{el}} B}{V_0} \\ k_3 = \dfrac{k_\theta^{\mathrm{el}}}{B V_0} \end{cases} \tag{4.5}$$

The RI have a negligible effect on the horizontal static stiffness of the reinforced system (Shen et al., 2022a,b). Furthermore, the LTP thickness is sufficiently small to ignore its contribution (IREX, 2012). Hence, k_x^{el} can be approximated with known formulas for circular shallow foundations, see for example (Gazetas, 1983):

$$k_x^{\mathrm{el}} = \frac{4 G_0 B}{2 - \nu} \tag{4.6}$$

with G_0 the equivalent shear modulus of an infinite homogeneous soil and ν the Poisson modulus. Although the dimensionless form is presented for a circular RI foundation, the

analytical formulas can be easily modified for other shapes, as proposed in Grange (2008). Correction factors to consider rectangular rigid foundations are also presented in (Gazetas, 1983).

No formulas exist for the elastic stiffnesses k_z and k_θ of RI foundations. A way to identify them is with FE linear elastic static simulations (by imposing small displacements or rotations at the foundation and evaluating the corresponding reactions). They can be also estimated from dynamic impedances calculations, see Sec. 4.4, considering a frequency equal to 0.

4.3 Plastic behaviour

The essential components to formulate the plastic behaviour of the ME are:

- a failure /ultimate bearing capacity envelope
- loading surfaces
- a plastic flow rule
- hardening laws for the internal variables

Following the plasticity theory (Hill, 1950; Borja, 2013), the plastic components in a given total displacement increment are written as:

$$\begin{bmatrix} \dot{w}^{\mathrm{pl}} \\ \dot{u}^{\mathrm{pl}} \\ \dot{\theta}^{\mathrm{pl}} \end{bmatrix} = \dot{\lambda} \begin{bmatrix} \frac{\partial g}{\partial v} \\ \frac{\partial g}{\partial h} \\ \frac{\partial g}{\partial m} \end{bmatrix} \tag{4.7}$$

where $\dot{\lambda}$ denotes the plastic multiplier, which determines the magnitude of the increment of plastic displacements, while the derivatives of the plastic potential g, give its direction.

4.3.1 Failure envelope

The "rugby ball shape" failure envelope, originally attributed to Nova and Montrasio (1991) and employed by (Gottardi and Butterfield, 1993; Cassidy, 1999; Gottardi et al., 1999, among others), is adopted hereafter, see Eq. 3.4 in Chapter 3. In terms of normalised loads, the expression is written similarly to (Cremer, 2001; Grange, 2008) but considering the inclination:

$$f_\infty := \left(\frac{h}{av^c(1-v)^d}\right)^2 + \left(\frac{m}{bv^e(1-v)^f}\right)^2 + \psi\frac{hm}{abv^{(c+e)}(1-v)^{(d+f)}} - 1 = 0 \tag{4.8}$$

where a and b define the size of the ellipse and ψ its inclination in the $m-h$ space; c, d and e, f control the parabolic shape in the $v-h$ and $v-m$ plane, respectively. A notable benefit of Eq. 4.8 is its capability to designate a maximum point for any segment along the parabolic contour within the $v-h$ and $v-m$ space. This feature proves valuable for aligning the contours with the shapes outlined in the EC8 standards (EN1998-5, 2004).

4.3.2 Loading surfaces

As in (Cremer, 2001; Grange, 2008), the loading surfaces have a similar shape to the failure envelope (here Eq. 4.8), and their evolution is described by a set of hardening variables. The following equation describes the loading surfaces:

$$\begin{aligned} f_c(\underline{\mathbf{F}}, \underline{\boldsymbol{\tau}}, \rho, \gamma) \quad := \quad & \left(\frac{h}{\rho a v^c (\gamma - v)^d} - \frac{\delta}{\rho}\right)^2 + \left(\frac{m}{\rho b v^e (\gamma - v)^f} - \frac{\beta}{\rho}\right)^2 + \\ & \psi \left(\frac{h}{\rho a v^c (\gamma - v)^d} - \frac{\delta}{\rho}\right) \left(\frac{m}{\rho b v^e (\gamma - v)^f} - \frac{\beta}{\rho}\right) - 1 = 0 \end{aligned} \tag{4.9}$$

where $\underline{\boldsymbol{\tau}} = (\delta, \beta)$ is a vector containing the two kinematic variables δ and β, ρ is an isotropic hardening variable and γ is a variable described in Sec. 4.3.3. At the ultimate state, the loading surface f_c should become identical with the failure envelope f_∞. This can be achieved (for radial loadings) considering the tangency rule (Prevost, 1978), see Sec. 4.3.3.

4.3.3 Evolution of internal variables

Kinematic hardening variables δ and β

The kinematic hardening variables δ and β provide the evolution of the centre of the ellipse in the $m-h$ plane. The equations being similar, only the evolution of δ is given hereafter in detail.

As mentioned in (Grange, 2008), according to the experimental (Gottardi et al., 1999) and numerical results (Cremer, 2001) for circular shallow foundations on different soil types submitted to monotonic static loadings, the different force-displacement curves contain an exponential term and are not dependent on the vertical force. The evolution of the internal variables can be therefore obtained using 1^{st} order differential equations. For instance, the relation linking the horizontal force h and the horizontal displacement u can be written as:

$$h = h_{\infty}^{*}\left(1 - \exp\left(-\frac{k_2}{h_{\infty}^{*}}u\right)\right) \tag{4.10}$$

where h_{∞}^{*} $(0 < h_{\infty}^{*} \leq 1)$ represents the curve limit of h when u tends to infinity.

The numerical FEM results of Chapter 2 on a circular RI foundation illustrate a similar behavior and thus Eq. 4.10 can again be adopted. For example, Fig. 4.2 depicts the representation of Eq. 4.10 in green bold lines, and the FE numerical results for different normalised vertical forces ($v = 0.125, 0.25, 0.375$ and 0.5) for a circular RI foundation.

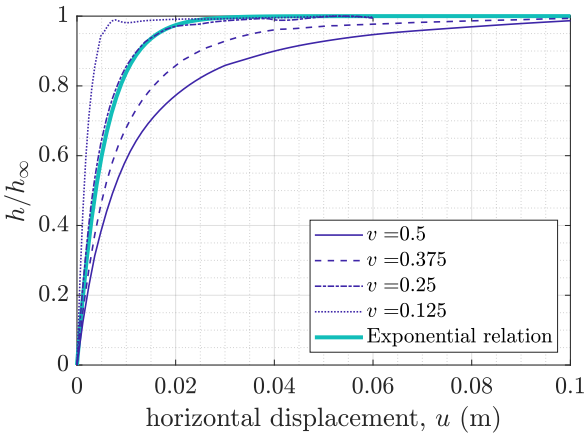

FIGURE 4.2 : Eq. 4.10 (exponential relation) and FE results for different normalised vertical forces for a circular RI foundation

The associated 1^{st} order differential equation has the following form:

$$\dot{h} = k_2\left(1 - \frac{h}{h_{\infty}^{*}}\right)\dot{u} \tag{4.11}$$

By assuming the classical partition of the total displacement into an elastic part and a plastic part (Eq. 4.2) and considering that at every step, we have $\underline{\mathbf{F}} = \underline{\underline{\mathbf{K}}}^{\mathrm{el}}\underline{\mathbf{u}}^{\mathrm{el}}$ we get:

$$\dot{h} = k_2\left(\frac{h_{\infty}^{*}}{h} - 1\right)\dot{u}^{\mathrm{pl}} \tag{4.12}$$

The evolution of the kinematic hardening variable δ is defined as follows (Grange, 2008):

$$\dot{\delta} = \frac{k_2}{2av^{c}\left(\gamma - v\right)^{d}}\left(\frac{h_{\infty}^{\star}}{\delta} - 1\right)\dot{u}^{\mathrm{pl}} \tag{4.13}$$

For cyclic (quasi-static) or seismic (dynamic) loadings, the behaviour depends on the loading direction. When the foundation undergoes a severe loading in the right direction

for example, the distribution of soil plastic strains is different below the right and the left part of the foundation. When the loading is reversed, the no symmetric distribution of stresses influences the behavior. In order to account for the influence of the loading direction, the evolution of the kinematic hardening variables can be written as (Grange, 2008):

$$\begin{cases} \dot{\delta}^{\oplus} = \dfrac{k_2}{2av^c\left(\gamma - v\right)^d}\left(\dfrac{h^*_{\infty}}{\delta^{\oplus}} - 1\right) & \left|\dot{u}^{\mathrm{pl}}\right| \\ \dot{\delta}^{\ominus} = \dfrac{k_2}{2av^c\left(\gamma - v\right)^d}\left(-\dfrac{h^*_{\infty}}{\delta^{\ominus}} - 1\right) & \left|\dot{u}^{\mathrm{pl}}\right| \end{cases} \tag{4.14}$$

where at each step, δ is computed as:

$$\delta = \delta^{\oplus} + \delta^{\ominus} \tag{4.15}$$

h^*_{∞} is calculated as:

$$\begin{cases} h^{*\infty} = \delta_{\mathrm{lim}} - \delta^{\ominus} & \text{if} \quad \dot{\delta} > 0 \\ h^{*\infty} = -\left(\delta_{\mathrm{lim}} - \delta^{\ominus}\right) & \text{if} \quad \dot{\delta} < 0 \end{cases} \tag{4.16}$$

where δ_{lim} is determined using the *tangency rule*, (Prevost, 1978; Cremer, 2001), see below. The equations describing the evolution of β are similar.

Isotropic hardening variable ρ

A relationship can be introduced between the isotropic ρ and the kinematic hardening variables $\underline{\boldsymbol{\tau}}$ (Cremer, 2001; Grange, 2008), (where the symbol $\|\|$ represents the norm and $d./dt$ the symbol for the derivative with respect to time)

$$\dot{\rho} = \left|\frac{d\|\underline{\boldsymbol{\tau}}\|}{dt}\right| = \left|\frac{\delta\dot{\delta} + \beta\dot{\beta}}{\sqrt{\delta^2 + \beta^2}}\right| \tag{4.17}$$

that translates the fact that when a plastic state is reached during a new cycle, plastic behaviour is recovered at the same state and with the same slope. The evolution is represented in Fig. 4.3 (without inclination, $\psi = 0$ in Fig. 4.3).

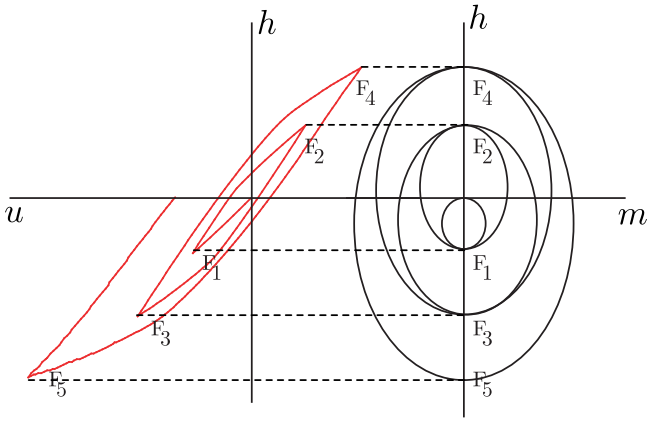

FIGURE 4.3 : Relation between the isotropic and kinematic hardening laws in the $u-h$ and $m-h$ planes for an increasing cyclic horizontal loading (points F_i) (no inclination is considered), modified from Cremer (2001)

Variable γ

The foundation is initially submitted only to the structure's self-weight ($h = m = 0$) and therefore $\gamma = v$. Then, the following empirical relationship provided by (Nova and Montrasio, 1991) is adopted:

$$\gamma = 1 - e^{(-k_1 w)} \tag{4.18}$$

Eq. 4.18 can be written as a 1^{st} order differential equation as:

$$\dot{\gamma} = k_1(1-\gamma)\dot{w} \tag{4.19}$$

or

$$\dot{\gamma} = k_1 \frac{1-\gamma}{\gamma} \dot{w}^{\mathrm{pl}} \tag{4.20}$$

When subjected to overturning moment and horizontal loads, additional plastic displacements, including horizontal displacements and rotations, can contribute to the expansion of the loading surface along the v direction. Therefore, the evolution of γ can be expressed as follows (Grange, 2008):

$$\dot{\gamma} = \left(c_1 k_1 \dot{w}^{\mathrm{pl}} + c_2 k_2 |\dot{u}^{\mathrm{pl}}| + c_3 k_3 |\dot{\theta}^{\mathrm{pl}}|\right) \frac{1-\gamma}{\gamma} \tag{4.21}$$

where c_{1-3} are constants to identify. They adjust the influence of each contribution (plastic displacements). By default, c_{1-3} are set to 1.

Tangency rule

The tangency rule (Prevost, 1978) is employed to ensure that the loading surface never crosses (or penetrates) the failure criterion. Additionally, the tangency rule helps determine the final loading point and the boundaries of the kinematic hardening variables for a non-radial loading (Grange, 2008). In order to apply the tangency rule for the ME for RI foundations, the initial loading surfaces (Eq. 4.9) are transformed in a new space $h^\dagger - m^\dagger$ where the ellipses can be reduced to circles.

$$\begin{bmatrix} m^\dagger \\ h^\dagger \end{bmatrix} = \begin{bmatrix} \cos(\theta) & \sin(\theta) \\ -\sin(\theta) & \cos(\theta) \end{bmatrix} \times \begin{bmatrix} m \\ h \end{bmatrix} \tag{4.22}$$

where θ represents the angle of rotation. In this new $h^\dagger - m^\dagger$ space, the loading surfaces take the form:

$$f_c(\underline{\mathbf{F}}, \underline{\boldsymbol{\tau}}, \rho, \gamma) = \left(\frac{h^\dagger}{\rho a v^c (\gamma - v)^d} - \frac{\delta}{\rho}\right)^2 + \left(\frac{m^\dagger}{\rho b v^e (\gamma - v)^f} - \frac{\beta}{\rho}\right)^2 - 1 = 0 \tag{4.23}$$

and the failure surface:

$$f_\infty = \left(\frac{h^\dagger}{a v^c (1 - v)^d}\right)^2 + \left(\frac{m^\dagger}{b v^e (1 - v)^f}\right)^2 - 1 = 0 \tag{4.24}$$

The following transformation (Cremer, 2001; Grange, 2008) is then applied:

$$h^* = \frac{h^\dagger}{a v^c \left(\gamma - v\right)^d} \quad \text{and} \quad m^* = \frac{m^\dagger}{b v^e \left(\gamma - v\right)^f} \tag{4.25}$$

and the elliptical shapes of the loading surfaces (Eq. 4.23) are transformed to circles in the $h^* - m^*$ plane with a radius ρ and a centre located at (δ, β):

$$f_{c_i} = \left(\frac{h^* - \delta}{\rho}\right)^2 + \left(\frac{m^* - \beta}{\rho}\right)^2 = 1 \tag{4.26}$$

while the elliptical shape of the failure surface (Eq. 4.24) is transformed to a circle in the $h^* - m^*$ plane with a radius 1 and a centre located at $(0, 0)$:

$$f_\infty = h^{*^2} + m^{*^2} = 1 \tag{4.27}$$

In Fig. 4.4, the ultimate loading point (denoted as F) is determined by projecting the current loading point (F_i) onto the failure criterion in the direction of the current force

increment ($\underline{\mathbf{dF}}_i$). Consequently, the centre of the final circle corresponds to the endpoint of the vector $\underline{\boldsymbol{\tau}}_{\text{lim}} = (\delta_{\text{lim}}, \beta_{\text{lim}})$ and it lies on the radius of the failure criterion. As proposed by (Grange, 2008; Grange et al., 2008), $\underline{\boldsymbol{\tau}}_{\text{lim}}$ is calculated using an iterative procedure: at the first iteration, the size of the loading surface is kept constant, and its centre is evaluated using the tangent rule. At the following iteration, a new position of the centre is calculated considering the increase in the size of the loading surface. The performance of the algorithm is, however, deteriorated in the case of complex loadings (i.e. no-radial or variable vertical force).

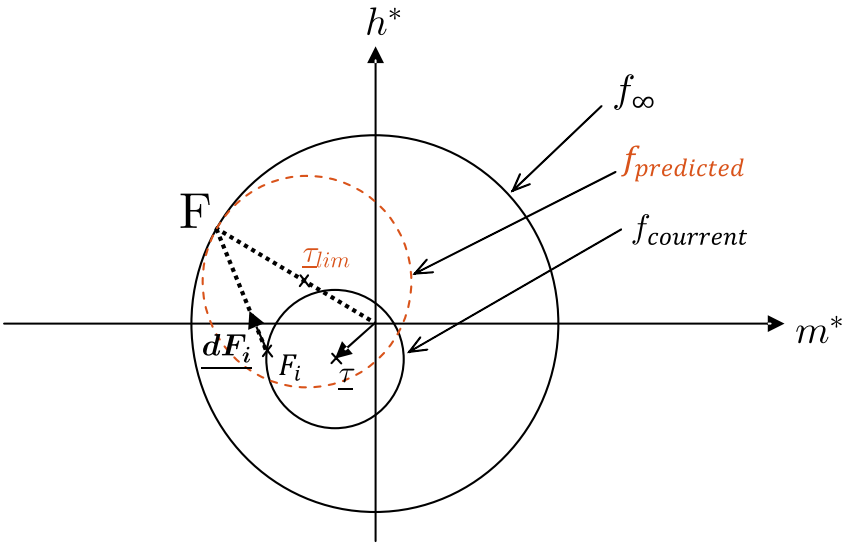

FIGURE 4.4 : Illustration of the tangent rule, modified from Crémer et al. (2001)

Flow rule

As for the macroelements introduced by Cremer (2001) and Grange (2008), an associate flow rule is used for the plane $h-m$ and a non-associate flow rule for the planes $h-v$ and $m-v$. Actually, in the region of low v values, due to the parabolic shape of the loading surfaces, the outward normal is negative regardless of the direction of the loading increment. Consequently, even as v increases, w decreases, which is counterintuitive. Opting for an ellipsoidal plastic potential centred at the origin allows increasing w^{pl} values within this zone (Le Pape et al., 1999).

The plastic potential (Grange, 2008) is given by:

$$g(\underline{\mathbf{F}}, \underline{\boldsymbol{\tau}}, \rho, v_c) := \left(\frac{h}{\rho \frac{a v_c^c}{(\kappa\gamma + v_c)^d} (\gamma - v)^d (\kappa\gamma + v)^d} - \frac{\delta}{\rho} \right)^2 + \left(\frac{m}{\rho \frac{b v_c^e}{(\xi\gamma + v_c)^f} (\gamma - v)^f (\xi\gamma + v)^f} - \frac{\beta}{\rho} \right)^2 - 1 = 0 \tag{4.28}$$

where the *current vertical force* v_c (representing the first component of the coordinates of the loading point F) is introduced. v_c ensures that the plastic potential g and the loading surface f_c intersect at the loading point F. This relationship holds in the plane $h - m$, where f_c and g have identical shapes, forming ellipses. However, in the planes $v - h$ and $v - m$, f_c and g are not associated. The parameters κ and ξ are introduced to modify the shape of the plastic potential, ensuring that it presents a horizontal tangent at a specified vertical reduced force v, which the user can choose.

In the general case, the horizontal tangent in the $m-v$ planes is positioned at $v = \frac{(1-\xi)}{2}$, while the horizontal tangent in the $v-h$ planes is located at $v = \frac{(1-\kappa)}{2}$. Fig. 4.5 illustrates the representation of g in the $v-h$ plane, where κ and ξ are set to 1 by default to achieve a horizontal tangent at v=0 consistently. Similar representations apply to the $v-m$ planes.

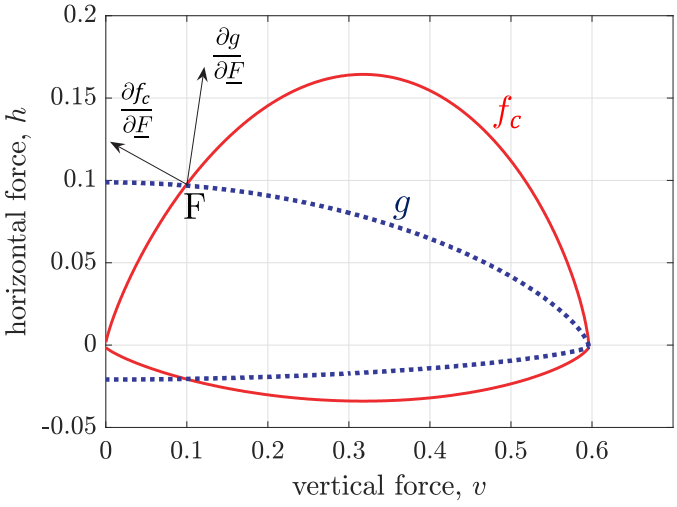

FIGURE 4.5 : Plastic potential g, the loading surface f_c, and the associated normal vectors for a specific loading point F in the $v - h$ plane, modified from Cremer (2001)

4.4 Extension to dynamics

In vibration theory, forced vibration of an n-degree-of-freedom oscillator is defined as the motion resulting from the application of a harmonic force with constant amplitude. The *impedance matrix* (sometimes called dynamic stiffness matrix) is a frequency-dependent matrix that relates the applied force amplitudes to the displacement amplitudes of the forced harmonic response (Géradin and Rixen, 2014).

In earthquake engineering, impedance functions are considered to take into account dynamic SSI (Wolf, 1989). They have the following form:

$$Z(\omega) = K(\omega) + iC(\omega) \tag{4.29}$$

with ω the excitation frequency (in practice the fundamental SSI frequency or the dominant frequency of the input motion). The real component $K(\omega)$ in impedance functions is called dynamic stiffness and represents the stiffness and inertia of the supporting soil. The imaginary component $C(\omega)$ represents the damping effect, generally due to radiation effects in the soil. The frequency dependence in impedance functions is due to frequency's impact on inertia, as soil properties remain largely unaffected by frequency variations (Gazetas, 1991).

This practice is prevalent in modern design methods, particularly in substructural methods (see, Sec. 1.4). Although relatively complex physical models can be used, see for example the *monkey tails models* (Wolf, 1989; Saitoh, 2007; Jue Wang and Wang, 2016), simple springs and dashpots calibrated with the predominant frequency of the input motion often yield satisfactory results (Saitoh, 2012; Perez-Herreros, 2020).

In order to extend the proposed macroelement to dynamics, it is suggested to calculate the impedance functions of typical RI foundation configurations and to provide analytical equations for practitioners, as the ones given by (Gazetas, 1983, 1991) for shallow foundations. The real components of the impedance functions can be used to calibrate the stiffness terms of Eq. 4.5, while the imaginary components the dashpots that can be easily added to the macroelement, as for example proposed in (Grange et al., 2009b).

To illustrate this, the real components (dynamic stiffnesses) of the impedance functions for a circular (diameter $B = 6$ m) shallow foundation on a homogeneous soil ($V_s = 200$ m/s and v=0.3) with (continuous lines) and without (non-continuous lines) RI, for the vertical, horizontal and rotational directions are provided in Fig. 4.6. The dynamic stiffnesses are calculated as described in Coronado and Gidwani (2016) with the FEM model introduced in Sec. 2.3 and are also compared to the analytical formulas for shallow foundations from (Gazetas, 1983).

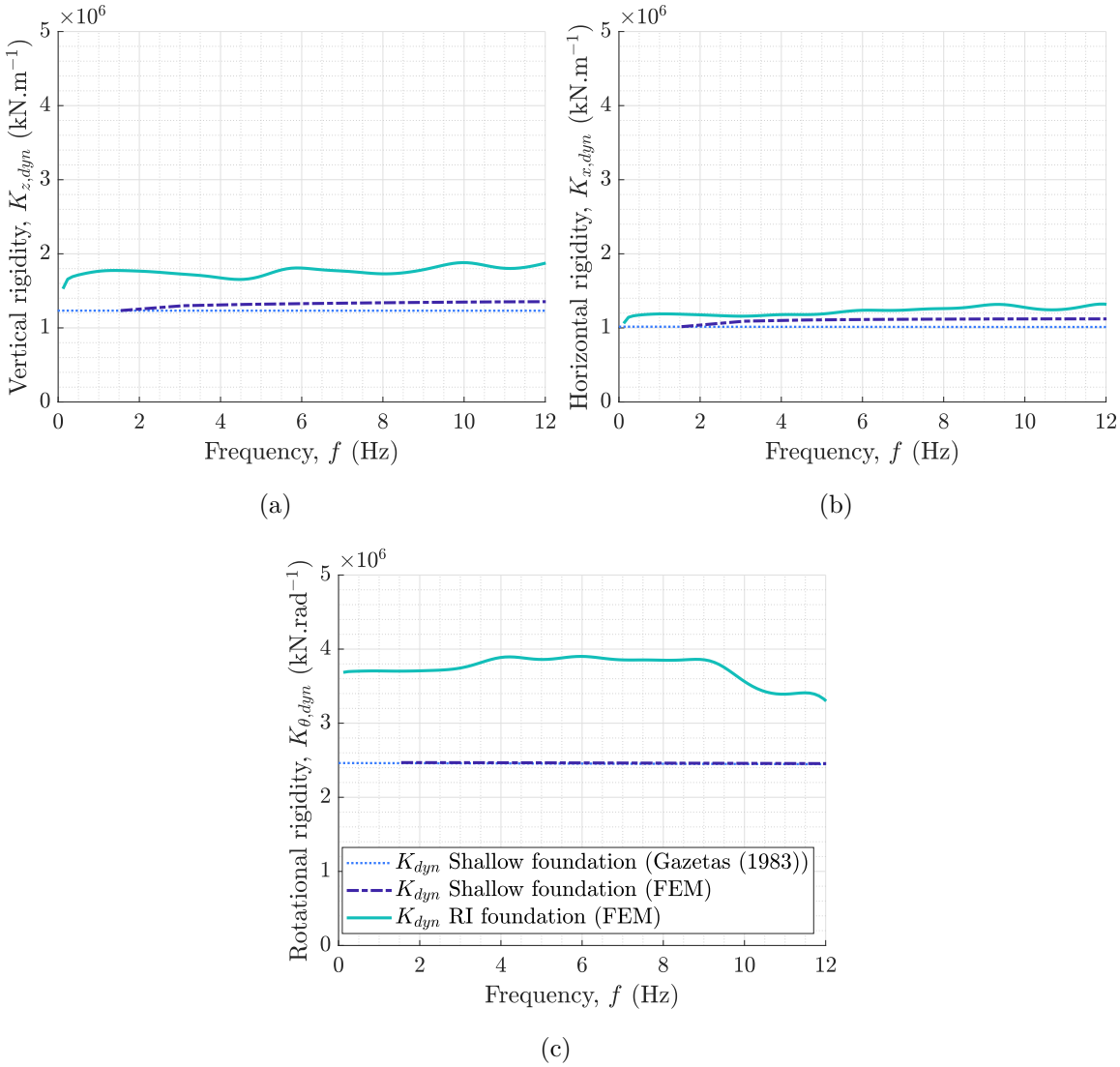

FIGURE 4.6 : The real components of the impedance functions for a circular (diameter B = 6 m) shallow foundation on a homogeneous soil (V_s = 200 m/s and v=0.3) with (continuous lines) and without (non-continuous lines) RI: (a) vertical and (b) horizontal and (c) rotational stiffness. Results are also compared with analytical formulas for shallow foundations (Gazetas, 1983). Calculations are made with the FEM of Sec. 2.3

The results presented in Fig. 4.6 do not represent a typical case because there is no LTP and there is no bottom stiff soil for the end-bearing RI. However, from this simple example, it can be observed that the influence of RI is significant in the vertical and rotational direction, where classical formulas of shallow foundations cannot be used. For this specific case and for the horizontal direction, the dynamic and the static rigidity (this latter is generally estimated at zero frequency) show that the influence of RI is negligible (see also (Shen et al., 2022b)).

4.5 Synopsis

A synopsis of the ME formulation follows:

- failure envelope:

$$f_\infty = \left(\frac{h}{av^c(1-v)^d}\right)^2 + \left(\frac{m}{bv^e(1-v)^f}\right)^2 + \psi\frac{hm}{abv^{(c+e)}(1-v)^{(d+f)}} - 1 = 0$$

- loading surface:

$$\begin{aligned} f_c(\underline{\mathbf{F}}, \underline{\boldsymbol{\tau}}, \rho, \gamma) \quad = \quad & \left(\tfrac{h}{\rho av^c(\gamma-v)^d} - \tfrac{\delta}{\rho}\right)^2 + \left(\tfrac{m}{\rho bv^e(\gamma-v)^f} - \tfrac{\beta}{\rho}\right)^2 + \\ & \psi\left(\tfrac{h}{\rho av^c(\gamma-v)^d} - \tfrac{\delta}{\rho}\right)\left(\tfrac{m}{\rho bv^e(\gamma-v)^f} - \tfrac{\beta}{\rho}\right) - 1 = 0 \end{aligned}$$

- hardening variables:

  - kinematic variables

    related to the horizontal force:

    $\delta = \delta^{\oplus} + \delta^{\ominus}$

    $\dot{\delta}^{\oplus} = \frac{k_2}{2av^c(1-v)^d}\left(\frac{h^*_\infty}{\delta^{\oplus}} - 1\right)\left|\dot{u}^{\mathrm{pl}}\right|$ and $\dot{\delta}^{\ominus} = \frac{k_2}{2av^c(1-v)^d}\left(-\frac{h^*_\infty}{\delta^{\ominus}} - 1\right)\left|\dot{u}^{\mathrm{pl}}\right|$

    $\beta = \beta^{\oplus} + \beta^{\ominus}$

    related to the moment:

    $\dot{\beta}^{\oplus} = \frac{k_3}{2bv^e(1-v)^f}\left(\frac{m^*_\infty}{\beta^{\oplus}} - 1\right)\left|\dot{\theta}^{\mathrm{pl}}\right|$ and $\dot{\beta}^{\ominus} = \frac{k_3}{2bv^e(1-v)^f}\left(-\frac{m^*_\infty}{\beta^{\ominus}} - 1\right)\left|\dot{\theta}^{\mathrm{pl}}\right|$

  - isotropic variable ρ

    $\dot{\rho} = \left|\frac{d\|\underline{\boldsymbol{\tau}}\|}{dt}\right| = \left|\frac{\delta\dot{\delta} + \beta\dot{\beta}}{\sqrt{\delta^2 + \beta^2}}\right|$

  - variable γ related to the vertical force in the self-weight initialisation:

    $\gamma = 1 - e^{(-k_1 w)}$ and

    related to the expansion of the loading surface in v direction:

    $\dot{\gamma} = \left(c_1k_1\dot{w}^{\mathrm{pl}} + c_2k_2|\dot{u}^{\mathrm{pl}}| + c_3k_3|\dot{\theta}^{\mathrm{pl}}|\right)\frac{1-\gamma}{\gamma}$

- flow rule:

  $g(\underline{\mathbf{F}}, \underline{\boldsymbol{\tau}}, \rho, v_c) := (\frac{h}{\rho\frac{av_c^c}{(\kappa+v_c)^d}v^c(1-v)^d(\kappa+v_c)^d} - \frac{\delta}{\rho})^2 + (\frac{m}{\rho\frac{bv_c^e}{(\xi+v_c)^f}v^e(1-v)^f(\xi+v_c)^f} - \frac{\beta}{\rho})^2 - 1 = 0$

The ME parameters are presented in Tab. 4.1.

TABLE 4.1 : Summary of the ME parameters

Parameter	Description	Group
B	diameter	geometry
V_0	vertical bearing capacity	elastic behaviour
k_z^{el}	vertical stiffness	
k_x^{el}	horizontal stiffness	
k_θ^{el}	rotational stiffness	
C_z	vertical dashpot	dynamics
C_x	horizontal dashpot	dynamics
C_θ	rotational dashpot	dynamics
a, b	shape in the $h-m$ plane	failure envelope
c, d and e, f	shape in the $v-h$ and $v-m$ plane	
ψ	inclination in the $h-m$ plane	
c_1, c_2, c_3	constant related to isotropic vertical variable γ	hardening laws
κ and ξ	constants controlling the flow rule	flow rule

4.6 Calibration

The calibration of the ME parameters is detailed hereafter (simple and more complex calibration methods are proposed).

(i) maximum vertical bearing capacity V_0: existing analytical solutions and methodologies are presented in IREX (2012), see Chapter 1. Additionally, Appx. C presents the V_0 calculation by a FEM model by means of the tangent method (Hirany and Kulhawy, 1988).

(ii) elastic stiffnesses: No closed-form solutions exist for RI foundations. In statics, k_x^{el} can be approximated with known formulas for circular shallow foundations, see for example Gazetas (1983). FEM can be used to solve the equivalent static problems or to calculate the impedances. For a dynamic loading case, the selection of the stiffness may be done at the frequency of the input signal. Similar to the case of shallow foundations, charts or analytical equations can be made for the practitioners.

(iii) dashpots: No closed-form solutions exist for RI foundations. FEM can be used to calculate the impedances. The selection of damping may be done at the frequency

of the input signal. Similar to the case of shallow foundations, charts or analytical equations can be made for the practitioners.

(iv) failure envelope identification: Sec. 3.8 presents a formula accounting for the shape variation for various geometrical and material configurations. They can also be calculated following the numerical procedure presented in Sec. 3.2.

(v) c_1, c_2 and c_3: they are typically set to 1. They can be adjusted if experimental or numerical data are available.

(vi) κ and ξ: set to 1 to ensure a horizontal tangent at $v = 0$. They can be adjusted if experimental or numerical data are available (see Sec. 4.3.3). For the general cases, κ and ξ are set to 1 to avoid counterintuitive vertical displacements.

The calibration of the ME parameters is summarized in Tab. 4.2.

TABLE 4.2 : Calibration of the ME parameters

Parameter	Calibration (simple)	Calibration (complex)
V_0	IREX (2012)	FEM, tangent method
k_z^{el}	charts (to be done)	FEM (static calculations or impedances)
k_x^{el}	Gazetas (1983)	FEM (static calculations or impedances)
k_θ^{el}	charts (to be done)	FEM (static calculations or impedances)
C_z	charts (to be done)	FEM (impedances)
C_x	0	FEM (impedances)
C_θ	0	FEM (impedances)
a, b	Sec. 3.8	FEM/experiments
c, d and e, f	Sec. 3.8	FEM/experiments
ψ	Sec. 3.8	FEM/experiments
c_1, c_2, c_3	1 1 1	FEM/experiments
κ and ξ	1 1	FEM/experiments

Chapitre 5

Validation of the macroelement

This chapter presents the validation of the macroelement using novel dynamic centrifuge tests results (Escoffier et al., 2023). The capacity of the macroelement to simulate the nonlinear behaviour of RI foundations is illustrated in terms of horizontal displacements, vertical displacement and moment rotation curves

5.1 Dynamic centrifuge tests

The main objective of the novel experimental centrifuge tests campaign performed by Escoffier et al. (2023) was to investigate the dynamic response of a structure resting on a RI foundation. The structure was a cylinder of diameter $6m$, height $12m$, and mass (foundation + structure) 164.7 ton. It was placed in a Laminar container to minimize the boundary effects on the three-layer soil profile presented in Chapter 2. The coverage area α was 7%, estimated from Eq. 2.1, considering 7 RI. A schematic representation of the model is presented in Fig. 5.1.

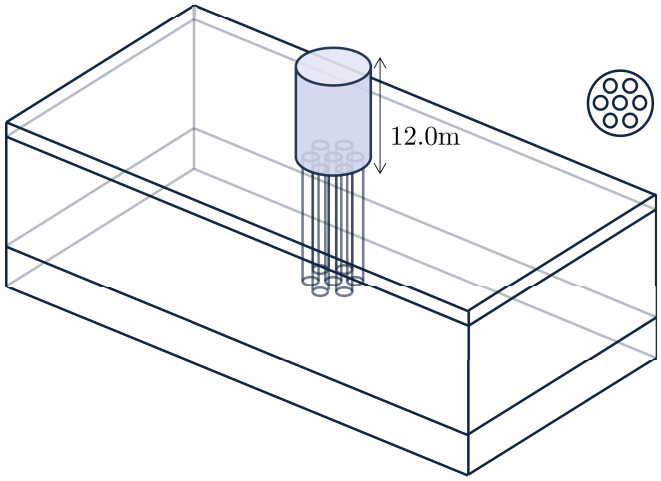

Figure 5.1 : Schematic representation of the centrifuge model, (Escoffier et al., 2023)

To assess the soil response, accelerometers (and pore pressure transducers) were positioned within the Laminar container. The structure was also equipped with accelerometers in both horizontal and vertical directions to monitor the kinematic response of the rigid

cylinder structure and laser sensors to track the displacements. The position of the sensors is shown in Fig. 5.2. For simplicity, only the sensors related to the validation of ME are labelled on the figure.

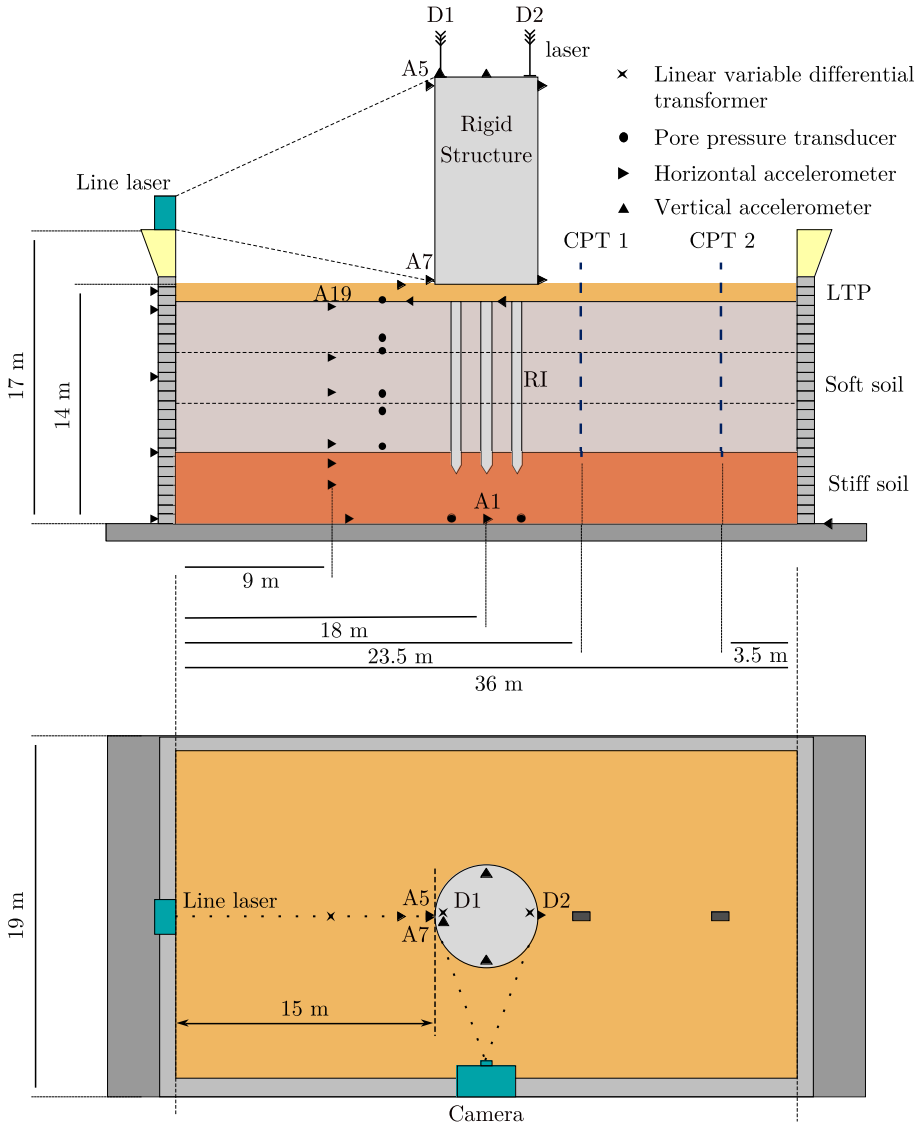

FIGURE 5.2 : Centrifuge model of the dynamic test of RI foundation, prototype scale: plane and front view, adopted from Escoffier et al. (2023)

Accelerometer A1 records the input signal at the base of the container. The overturning moment at the base of the foundation was calculated using accelerometer A5 (multiplying with the mass and the height of the structure). The rotation at the base was calculated from A5 and A7 (after a double integration to get the displacements D5 and D7, calculation of their difference and then dividing with the height of the structure). Settlement (vertical displacement) was calculated as the average between the vertical displacements

D1 and D2. The acceleration recorded by A19, positioned near the soil surface and having a considerable distance from the structure, is considered hereafter as the ground surface acceleration and the input signal to the ME.

The container with the soil and structure was placed in the centrifuge, and the gravitational force increased gradually from 0 to 50 g. After nearly two hours of consolidation in flight, the model was stabilised. Then, twenty ground motions were applied at the base of the model, see Tab. 5.1. Six of them (the ones in **bold**) are numerically reproduced hereafter with the ME.

TABLE 5.1 : Signal type and PGA of the sequence's input motions (Escoffier et al., 2023)

Signal	PGA (g)
Landers 0.05g	0.72
Northridge 0.05g	0.074
Sinus 50 Hz 0.05g	0.119
Sinus 50 Hz 0.15g	0.261
Sinus 50 Hz 0.25g	0.364
Landers 0.05g	0.079
Sinus 90 Hz 0.05g	0.086
Sinus 90 Hz 0.15g	0.275
Sinus 90 Hz 0.25g	0.397
Landers 0.05g	0.075
Sinus 120 Hz 0.05g	0.141
Sinus 120 Hz 0.15g	0.292
Sinus 120 Hz 0.25g	0.412
Landers 0.05g	**0.08**
Landers 0.15g	**0.196**
Landers 0.30g	**0.328**
Northridge 0.05g	**0.084**
Northridge 0.15g	**0.225**
Northridge 0.30g	**0.464**
Landers 0.05g	0.075

Typical experimental results are provided in Fig. 5.3, (Escoffier et al., 2023). One can observe an increase in the acceleration at the top of the structure, the development of settlement and dissipation and nonlinearities in the moment-rotation curve (results are given for Landers 0.15g).

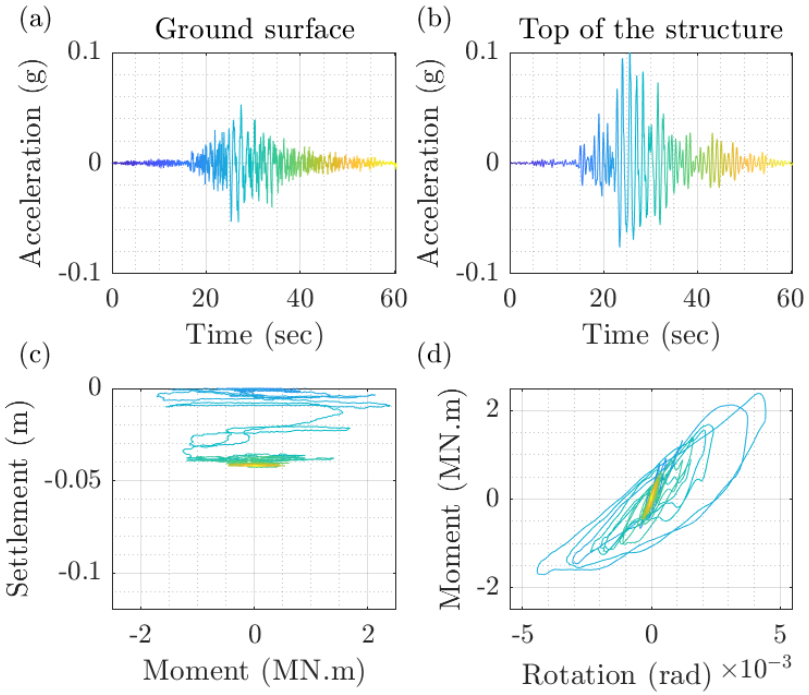

FIGURE 5.3 : Experimental results, Landers 0.15g: acceleration (a) at the ground surface, (b) at the top of the structure, (c) settlement vs. moment and (d) moment vs. rotation, (Escoffier et al., 2023)

5.2 Numerical model

The macroelement is positioned at the base of the finite element model (zero-length element) and represents the RI foundation and the surrounding soil, see Fig. 5.4.

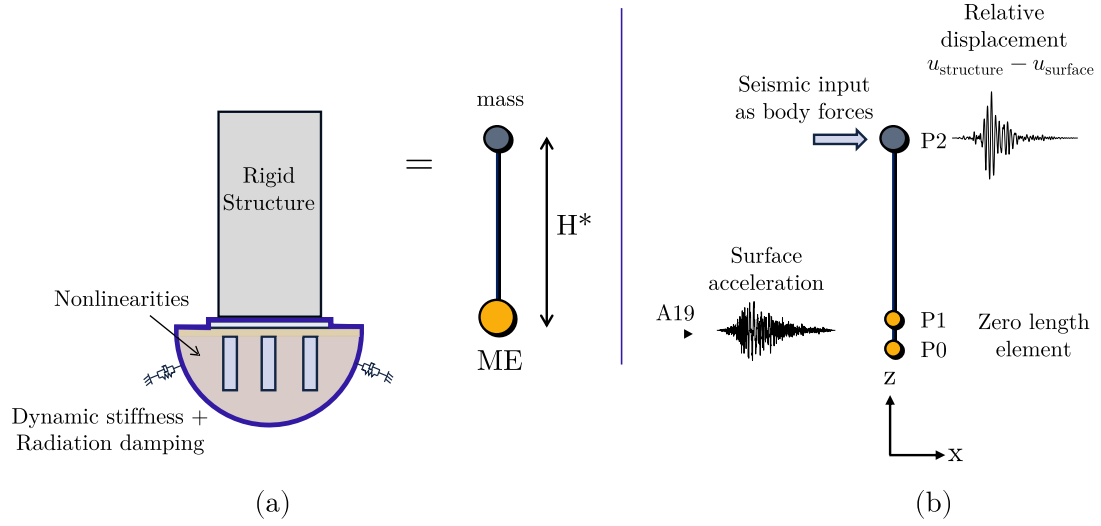

FIGURE 5.4 : Illustration of the numerical model

A beam with a concentrated mass at the top is used to represent the structure. It is important to note that the precise position of the mass was not measured; instead, it was estimated between 9 m and 12 m (Escoffier et al., 2023). The concentrated mass was set at $H = 11$ m in the numerical model. The modal analysis has shown that the first numerical eigenfrequency corresponds to the experimental fundamental frequency (7.8 Hz). In the following, calculations were done using Cast3M CEA (2001), considering a Rayleigh damping of 2% and the implicit Newmark integration scheme. The macroelement's parameters are summarised in Tab. 5.2. More specifically:

- V_0 is calculated from the FEM model, see Sec. 2.3 and Appx. C using the tangent method (Hirany and Kulhawy, 1988).
- a, b, c, d, e, f and ψ are calculated from Tab. 3.3 and Eq. 3.6, considering $\alpha = 7\%$, $\mathrm{H_{LTP}} = 1$ m and $\varphi_{\mathrm{LTP}} = 36$.
- Impedance calculations were made considering a multi-layer model, and the procedure explained in Coronado and Gidwani (2016). Fig. 5.5 shows the results for the dynamic stiffnesses. The input signal frequencies in Tab. 5.1 varying between 0.8 to 1.2 Hz, the stiffnesses at frequency equals zero are considered to identify k_z^{el}, k_x^{el} and k_θ^{el}.

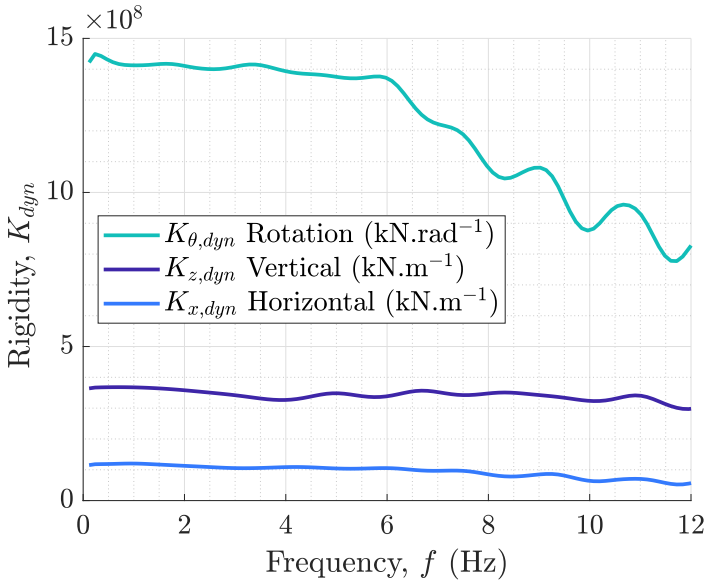

FIGURE 5.5 : Dynamic stifnesses

- No radiation damping is considered as in the dynamic centrifuge tests all the stress wave energy was enclosed in the laminar container.

TABLE 5.2 : Parameters of the macroelement

Parameter	Value	SI Unit
V_0	4593×10^3	N
k_z^{el}	3.98×10^8	N.m^{-1}
k_x^{el}	1.45×10^8	N.m^{-1}
k_θ^{el}	1.4×10^9	N.rad^{-1}
a	0.7064	-
b	0.442	-
c, d and e, f	1 1 1 1	-
ψ	-0.3325	-
c_1, c_2, c_3	1 1 1	-
κ and ξ	1 1	-

5.3 Numerical vs Experimental results

To assess the proposed ME's performance, we compare hereafter the horizontal kinematic displacement at the top of the structure[1] and the rotational behaviour and settlement at the foundation level with the dynamic experimental data provided in Escoffier et al. (2023). The calculations, completed on a personal system with an Intel Core i7 processor at 2.90 GHz, last approximately 8 minutes for each dynamic input.

The following observations can be done for the Landers input signal (Fig. 5.6, Fig. 5.7 and Fig. 5.8):

- the numerical model underestimates the displacement at the top of the structure especially for the 0.05g and 0.15g signals (Fig. 5.6 (a) and Fig. 5.7 (a)).
- the numerical model significantly underestimates the vertical displacements, (Fig. 5.6(b), Fig. 5.7(b) and Fig. 5.8(b)).
- The numerical rotation vs moment curves are comparable to the experimental results, especially for the 0.15g signal (Fig. 5.7 (c)).

1. The residual displacement can not be measured by the accelerometers, and the residual displacement of the rigid structure is not considered and compared.

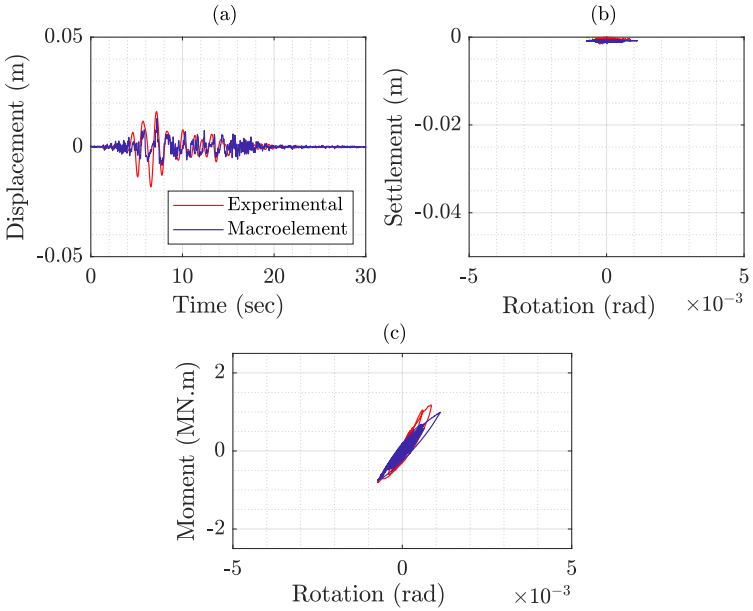

FIGURE 5.6 : Comparison between the ME numerical (blue line) and the experimental results (grey line) from Escoffier et al. (2023). Landers 0.05g (a) horizontal displacement at the top of the structure, (b) rotation vs settlement and (c) rotation vs moment

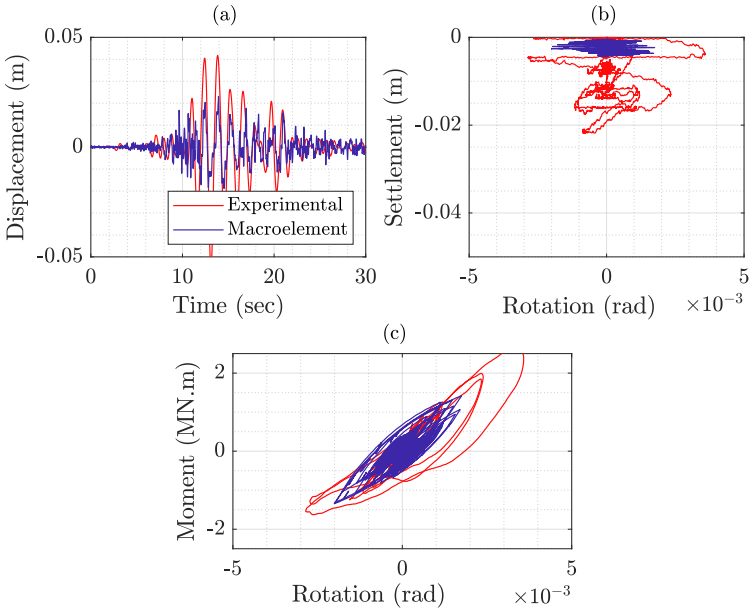

FIGURE 5.7 : Comparison between the ME numerical (blue line) and the experimental results (grey line) from Escoffier et al. (2023). Landers 0.15g (a) horizontal displacement at the top of the structure, (b) rotation vs settlement and (c) rotation vs moment

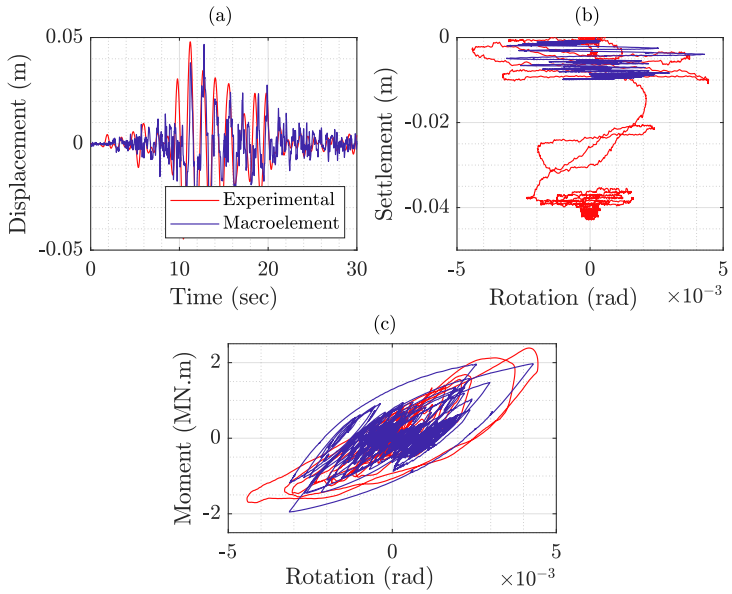

FIGURE 5.8 : Comparison between the ME numerical (blue line) and the experimental results (grey line) from Escoffier et al. (2023). Landers 0.3g (a) horizontal displacement at the top of the structure, (b) rotation vs settlement and (c) rotation vs moment

Similar trends can be observed for the Northridge input signals, see Fig. 5.9, Fig. 5.10, Fig. 5.11, although the results are better in terms of displacements at the top of the structure.

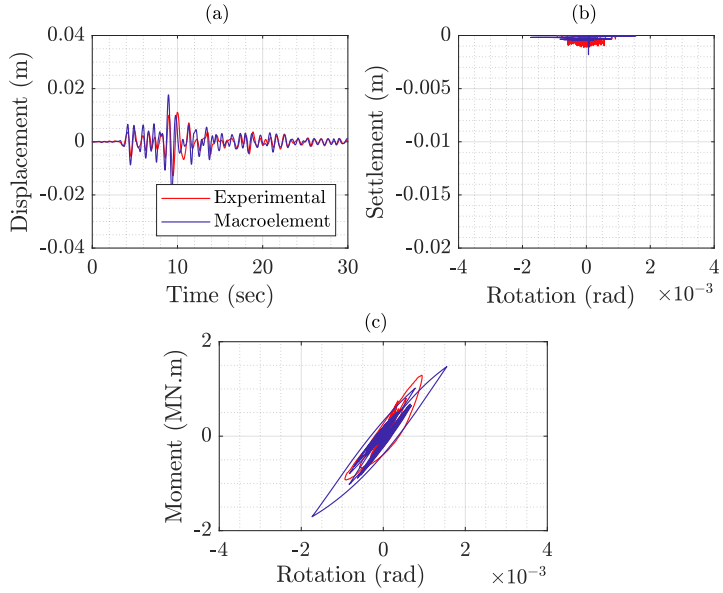

FIGURE 5.9 : Comparison between the ME numerical (blue line) and the experimental results (grey line) from Escoffier et al. (2023). Northridge 0.05g (a) horizontal displacement at the top of the structure, (b) rotation vs settlement and (c) rotation vs moment

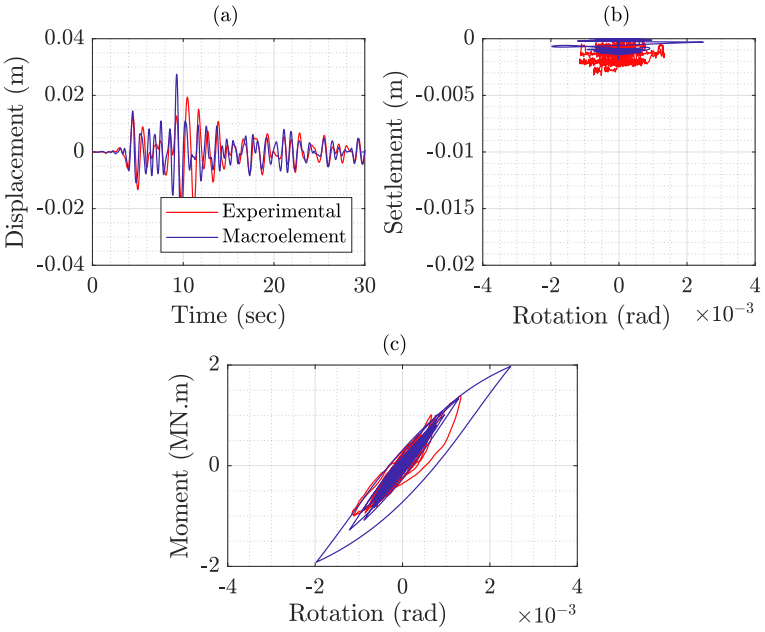

FIGURE 5.10 : Comparison between the ME numerical (blue line) and the experimental results (grey line) from Escoffier et al. (2023). Northridge 0.15g (a) horizontal displacement at the top of the structure, (b) rotation vs settlement and (c) rotation vs moment

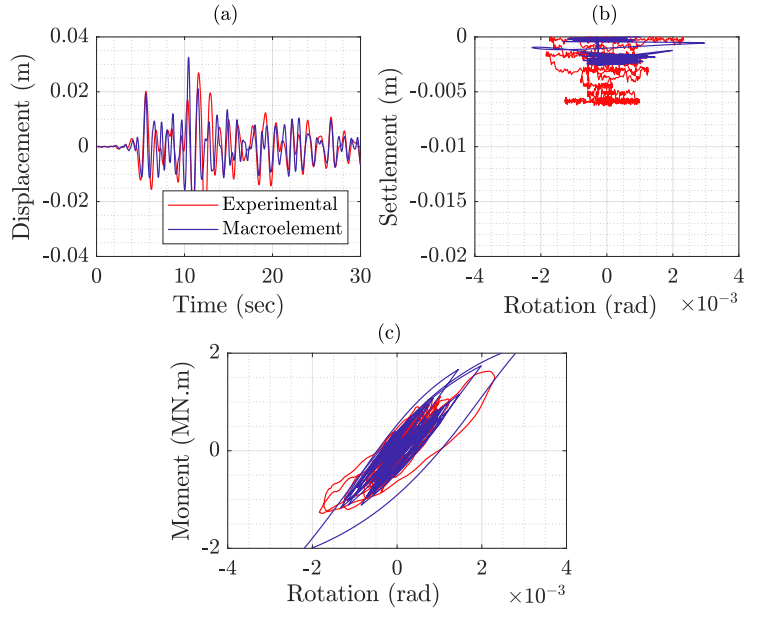

FIGURE 5.11 : Comparison between the ME numerical (blue line) and the experimental results (grey line) from Escoffier et al. (2023). Northridge 0.3g (a) horizontal displacement at the top of the structure, (b) rotation vs settlement and (c) rotation vs moment

To improve the response of the ME concerning settlement, a different value can be assigned to the parameters c_1, c_2 and c_3 (Sec. 4.3.3) based on the experimental results obtained. Since settlement is mainly influenced by the horizontal and rotational plastic displacement, c_1 is not modified, and c_2 and c_3 are set to 4.5. As the displacement at the top of the structure and the rotation vs moment results do not vary, only the settlement curves are shown. Fig. 5.12 shows that by changing these coefficients to what is observed in the experimental results, a better fit for the ME response is achieved.

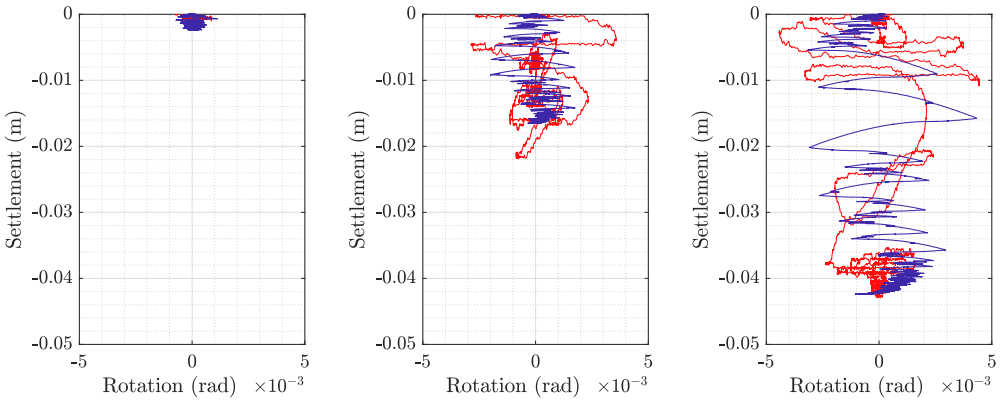

FIGURE 5.12 : Comparison between the ME numerical (blue line) and the experimental results (grey line) from Escoffier et al. (2023) with c_2 and c_3 variation. Rotation vs settlement curves (a) Landers 0.05g (b) Landers 0.15g and (c) Landers 0.3g

Similar trends can be observed for the Northridge input signals, see Fig. 5.12 and Fig. 5.11; c_2 and c_3 are set to 2.5.

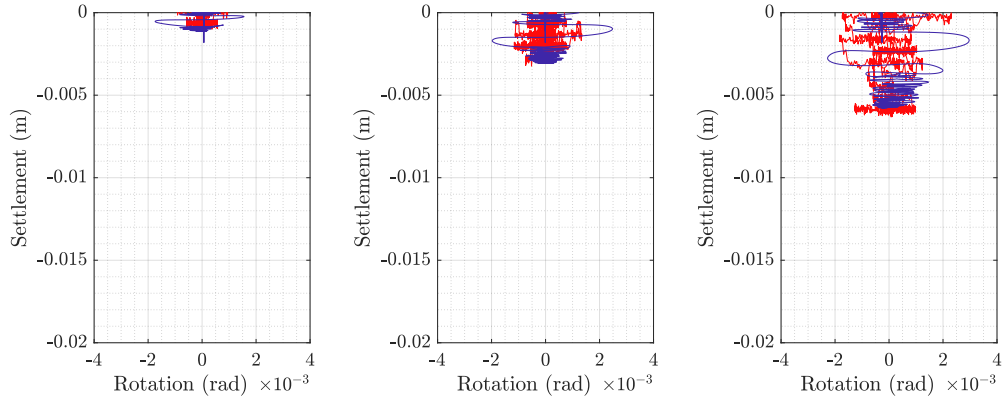

FIGURE 5.13 : Comparison between the ME numerical (blue line) and the experimental results (grey line) from Escoffier et al. (2023) with c_2 and c_3 variation. Rotation vs settlement curves (a) Northridge 0.05g (b) Northridge 0.15g and (c) Northridge 0.3g

5.4 Conclusions

The macroelement's performance under seismic loadings was tested considering novel experimental test results of a rigid structure on RI foundation (Escoffier et al., 2023). Although limited to only one experimental setup, the performance of the proposed macroelement is satisfactory. The ME model effectively captures the overall response, including cyclic behaviour and loading-reloading loops in the majority of cases. It successfully reproduces the general trends in displacement and rotational behaviour. The proposed modifications based on the plastic horizontal displacement and moment contribution to the settlement improved the maximal vertical displacement of results. However, a critical limitation of ME is still its calibration procedure. Formulas/charts are not available, so the calibration in this Chapter relied on the numerical simulations (or experimental data). This limitation may pose a significant barrier to the widespread adoption of the proposed ME in engineering practice.

This page intentionally left blank

CONCLUSION AND PERSPECTIVES

Conclusions

The main objective of this thesis was to develop a simplified and accurate numerical tool, based on the macroelement (ME) approach, to simulate the nonlinear behaviour of rigid inclusions (RI) foundations subjected to static and seismic loadings. The proposed ME takes into account the soil-structure interaction (SSI), and the global behaviour of the system is represented at the foundation level.

A comprehensive overview of the state-of-the-art research on RI was provided on the fundamental principles governing the behaviour of RI foundations, such as load transfer mechanisms, stress distribution, and stiffness modifications. These aspects were explored to elucidate the benefits of the RI in reducing the foundation's settlement and improving its bearing capacity in zones prone to seismic loadings. The most common numerical methods accounting for SSI were presented. Although robust, they often involve complex calculations and extensive computational resources. The limitations of these methods, coupled with the growing demand for efficient and accurate simulations on RI foundations under seismic loadings, elucidated the need for simplified approaches such as the ME.

The proposed plasticity-based ME approach is fast and can reproduce different 3D nonlinear behaviours, but they are valid only for given configurations (*e.g.*, specific foundation shapes and sizes, stratigraphy). Therefore, numerical finite element method (FEM) analyses using the open-source FEM code Cast3M (CEA, 2001) were done first to construct a numerical 3D model against novel centrifuge data in static cases.

Modelling of RI foundations in 3D FEM

The 3D FEM model proved to be appropriate to reproduce the bearing capacity response of a foundation with and without RI:

- the soil-RI interaction in the numerical model showed the different transfer mechanisms involving the transmission of loadings through the arching in the LTP and the frictional interaction between the inclusions and the soil, aligning with previous experimental observations;

- the vertical stress distribution to stiffer soil layers through the LTP and inclusions was observed in the model; as a consequence, the soil load-bearing capacity was significantly increased;

The results demonstrate the capability of the FEM model to simulate the complex nonlinear mechanisms of a RI foundation accurately. Consequently, the 3D FEM model was used to develop a novel failure envelope of a RI foundation.

Failure envelope of RI foundation

The validated FEM model was then used to identify the RI foundation's 3D failure envelope (in the combined $V - M - H$ space) by means of swipe tests, and an original analytical formula was provided for the failure envelope. It defines the admissible forces the soil-RI foundation system can support. The main conclusions are given hereafter:

- the increase of the RI foundation failure envelope under high vertical forces was illustrated. However, the contribution of RI was not observed for small vertical values.
- with few simulations, numerical swipe test analyses proved to be efficient at establishing the footing failure locus in the $V - M - H$. However, a lack of precision was observed for small vertical values;
- the analysis of parameters like covering area (α), LTP thickness ($\mathrm{H_{LTP}}$), and LTP friction angle (φ_{LTP}) revealed complex interactions, offering valuable insights for predicting RI foundation behaviour.

Finally, an appropriate closed-form mathematical formulation was proposed. The formula considers the influence of geometrical and material properties on the failure envelope shape. Engineers can use the proposed analytical failure envelope to quantify the bearing capacity of RI foundations under complex 3D loading. The proposed formula was used to develop a macroelement for RI foundations.

Macroelement modelling for a RI foundation

A novel plasticity-based ME for a RI foundation was proposed, in which the global behaviour of the foundation and the surrounding soil are lumped into a single constitutive equation relating the evolution of generalised forces and displacements:

- the calibration of the ME parameters was detailed, involving simple and more complex calibration methods.
- a validation of the macroelement using novel dynamic centrifuge test results was presented. The capacity of the macroelement to simulate the nonlinear behaviour was illustrated in terms of horizontal displacements, vertical displacement and moment rotation curves;
- a significant contribution of these results is the complex cyclic loading consideration of the nonlinear constitutive relationship between applied forces and deformations by only a few parameters.

Results prove the ME to be an accurate and robust simplified numerical tool. It maintains an adequate description of dynamic SSI while considering the nonlinear behaviour of a RI foundation.

Ordinary projects typically do not demand complex solutions as they depend on standards and experience for design. However, as the solution requires, practitioners must rely on a robust scientific foundation rather than blind application of formulas. Therefore, one of the main objectives of this work was to present to engineers with a strong background and knowledge of the nonlinear behaviours intended to be captured in the ME to ensure safe and accurate results, avoiding reliance on the ME as a black box. So, when the importance of the project justifies the account of SSI, the use of this simplified approach could be a feasible option to reduce computational costs while capturing the essential aspects of a RI foundation under seismic loadings.

Perspectives

This work suggests several research directions for future exploration:

- Refining analytical failure envelope parameters: further exploration on the parameter of the analytical failure envelope formula for different soil stratigraphy and foundation geometries;
- Dynamic stiffness and damping impedances: the calculation of dynamic stiffness and damping impedances in the frequency domain for various configurations. This can lead to the development of charts facilitating stiffness calculations for simplified real-case scenarios similar to those existing for shallow foundations (Gazetas, 1983);

- Enhancing macroelement approach for seismic loadings: while the macroelement approach is effective under 2D loading conditions (3 DoF), its performance under complex 3D seismic loading (5 DoF) is still a question.
- Addressing frequency-dependent response: accounting for the frequency-dependent response of the RI foundation. This could be approached as Gorini and Callisto (2023), the small-strain response is combined with the initial stiffness, accounting for the participating masses of the system;
- Exploring poromechanical behaviour: understanding how soil properties change concerning pore pressure and mechanical stress can significantly impact the design and performance of RI foundations under undrained or partial drained conditions. The modeling of these effects by macroelement is still challenging.

Appendices

Annexe A

Research report, project ASIRIplus, Benchmark No 1 "*Vertical bearing capacity under static loading*"

A.1 Introduction

This annexe is dedicated to the research report, project ASIRIplus, Benchmark No. 1 "*Vertical bearing capacity under static loading*". The benchmark concerns the prediction of vertical load transfers in the case of static loading of an isolated footing resting over a Load Transfer Platform (LTP) and a compressible soil reinforced with four rigid inclusions (RI). Two geometric configurations are modelled and studied.

The report presents the method used, the geometric and mechanical characteristics, the assumptions adopted (boundary conditions, simplifications) and all the model parameters. Results (*i.e.*, forces applied to the footing as a function of its displacement) are presented at the end.

A.2 Methodology

A.2.1 Description

Given the low permeability of the soil, the hypothesis adopted is that the test corresponds to undrained conditions. The parameters in each soil layer are varied to represent the decrease in the over-consolidation ratio (OCR) and the increase in cohesion (Su) with depth based on the shear modulus. The different details are presented in the sections below.

3D Finite Elements (FE) and the Cast3m general purpose finite element software are

used (CEA, 2001). Due to symmetry, the calculations consider only half of the domain (Fig. A.1) and the finite element mesh is given in Fig. A.1. A Drucker-Prager constitutive law, already implemented in Cast3m and calibrated on a Mohr-Coulomb model, is used for the Load Transfer Platform (LTP) (red) and the compressible soil layers (yellow). Linear elastic behaviour is adopted for the footing (white), the incompressible soil (purple) and the RI (orange in section A' - A').

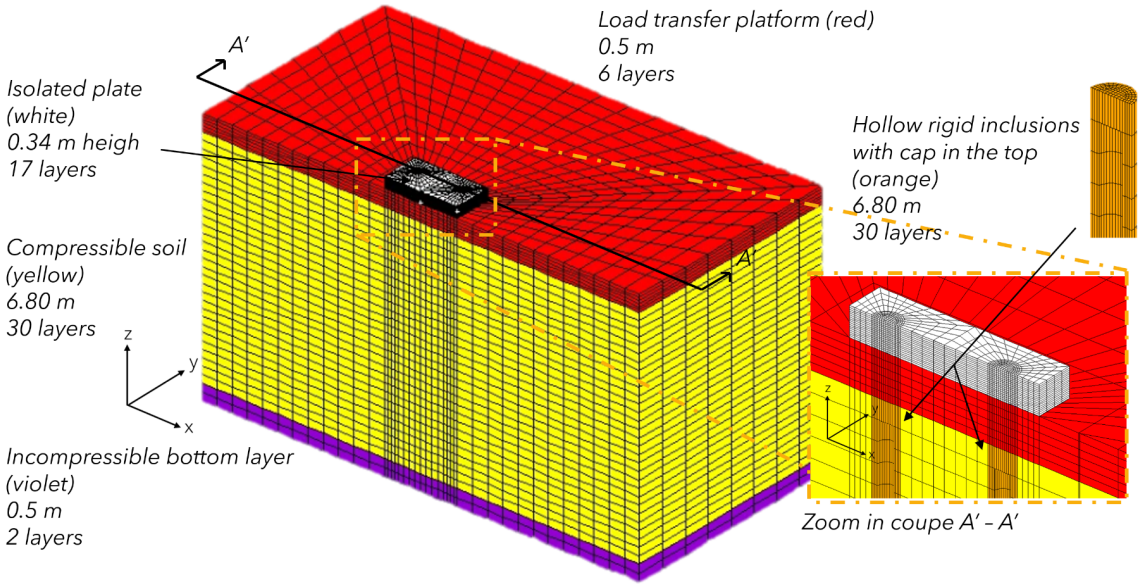

FIGURE A.1 : Finite element model

A.2.2 Geometrical characteristics

Two isolated square footings are modelled (Case A, Case B). The rigid aluminium RI have a hollow circular cross-section with an external diameter of $d = 0.34$ m and an internal diameter of 0.19 m. The end of the section at the head of the RI is considered solid (not hollow). For reasons of modelling simplicity and lack of additional information, it has been assumed that this solid part has a height of 0.2267 m. The total length of the RI corresponds to the height of the compressible soil, *i.e.*, 6.80 m. The dimensions of the RI foundation are as follows:

- Case A:
  - Length of the slab: 2.53 m
  - Thickness of the slab: 0.33 m
  - Distance between RI centres: s= 1.70 m

- Coverage area: $\alpha = \pi \frac{d^2}{4s^2} = 4.9\%$

- Case B:

  - Length of the slab: 2.21 m
  - Thickness of the slab: 0.33 m
  - Distance between RI centres: s= 1.36 m
  - Coverage area: $\alpha = \pi \frac{d^2}{4s^2} = 4.9\%$

A.2.3 Spatial discretisation

The thicknesses (vertical discretisation, according to z) of the clay layers are chosen to allow a maximum frequency ($f_{\max}$) of at least 20 Hz. The maximum layer thickness ($t_{\max}$) for a specified cut-off frequency ($f_c = f_{\max}$) is given by the following equation (Jeremić and Presig, 2005):

$$t_{\max} <= \frac{\lambda_{\min}}{n} = \frac{V_s}{n \cdot f_{\max}} \tag{A.1}$$

where $\lambda_{\min}$ is the wavelength corresponding to the cut-off frequency, V_s is the ground shear wave velocity, and n is the desired "resolution", which can be described as the number of soil layers per shortest wavelength ($\lambda_{\min}$). About ten layers per shortest wavelength seem appropriate for non-linear time-domain analysis ($n = 10$) (Jeremić and Presig, 2005).

Assuming a minimum shear wave velocity V_s between 50 - 150 m/s, which is conventional for compressible soils, the maximum thickness in the compressible soil allowing an appropriate spatial description of the passage of the wave is $t_{\max} = 0.25$ m. Therefore, 30 layers are finally chosen for the compressible soil of thickness $t_{str} = H_{str}/N_{str} = 0.2267$ m (yellow in Fig. A.1), six layers for the LTP $t_{LTP} = 0.0833$ m (red in Fig. A.1), two layers for the incompressible soil of thickness $t_{SI} = 0.25$ m (purple in Fig. A.1) and two layers for the footing of thickness $t_{sem} = 0.165$ m (white in Fig. A.1). The vertical discretisation of the hollow section RI is the same as for the compressible soil $t_{IR} = 0.2267$ m. The solid section of the inclusion considers only the first layer.

The horizontal length of the model is chosen to be five times the width of the footing, and the number of finite elements in this direction is equal to 12 in the direction X of size 0.46 m and 8 in the direction Y with a variable size of 0.138 m to 0.691 m. A finer discretisation is chosen under the footing (see Fig. A.1).

A.2.4 Boundary conditions

Symmetry conditions are considered so that half the domain can be used. More specifically, displacements according to Y are blocked in the plane of symmetry (Fig. A.2 d). In addition, the left and right sides of the model are blocked at X (Fig. A.2 a), the other side along Y (Fig. A.2 b), and the base along Z (Fig. A.2 c).

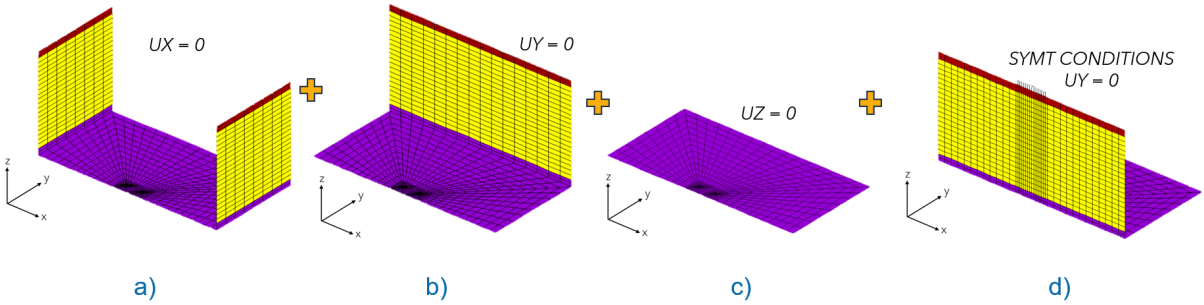

FIGURE A.2 : Boundary conditions applied to the FE model

A.2.5 Loading procedure

Experimentally, the test was controlled in displacement with a constant speed under quasi-static conditions (1mm/min). In the finite element model, the loading is applied in two phases (Fig. A.3):

- Phase 0: system subjected to its weight
- Phase 1: vertical displacement applied at a point in the middle of the footing

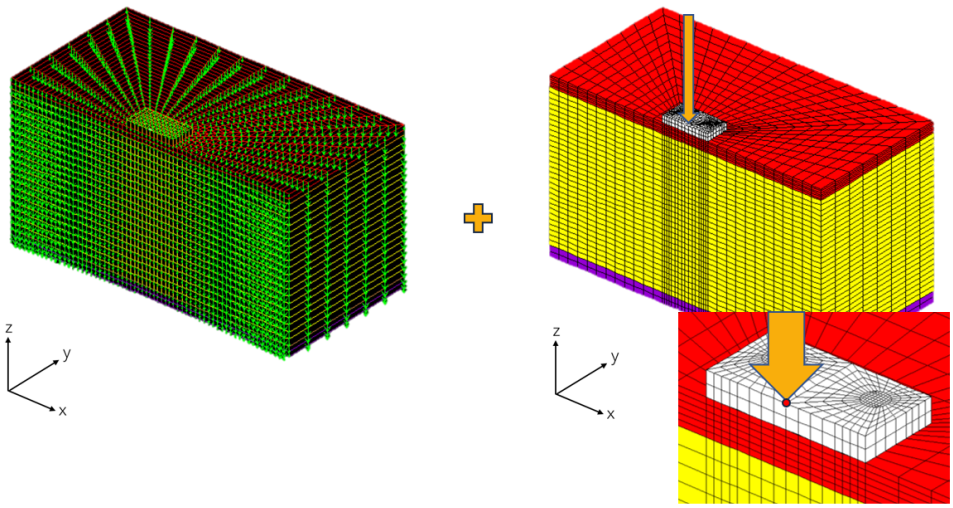

FIGURE A.3 : Finite element model: loading procedure

A.2.6 Material parameters

The materials associated with the footing and RI are supposed to be linearly elastic, and their characteristics are described in Tab. A.1

TABLE A.1 : Parameters used for the elastic materials

Parameters	Symbol	Footing	Rigid Inclusions	Unity
Mass density	ρ	2497	2497	kg/m^3
Young modulus	E	20	20	GPa
Poisson modulus	ν	0.3	0.3	-

Compressible soil

The Mohr-Coulomb criterion, used for fine soils and cohesive soils, is characterised by the following relationships:

$$F(\sigma_{ij}) = (\sigma_1 - \sigma_3) - (\sigma_1 + \sigma_3) \cdot \sin\varphi - 2 \cdot c \cdot \cos\varphi \leq 0 \tag{A.2}$$

$$G(\sigma_{ij}) = (\sigma_1 - \sigma_3) - (\sigma_1 + \sigma_3) \cdot \sin\psi + a \tag{A.3}$$

It has five parameters: E, ν, c, φ, and ψ, where E is the soil Young modulus, c the cohesion, φ the angle of internal friction and ψ the angle of expansion. σ_1 and σ_3 represent the principal stresses ($\sigma_1 \geq \sigma_2 \geq \sigma_3$). In the space of principal stresses, the surface defined by the Mohr-Coulomb criterion is a hexagonal pyramid.

The relations defining the Drucker-Prager model implemented in Cast3M are given by:

$$F(\sigma_{ij}) = \alpha I_1(\sigma_{ij}) + \beta\sqrt{3J_2(\sigma_{ij})} - k \leq 0 \tag{A.4}$$

$$G(\sigma_{ij}) = \alpha I_1(\sigma_{ij}) + \beta\sqrt{3}J_2(\sigma_{ij}) \tag{A.5}$$

Analogies between the Mohr-Coulomb and Drucker-Prager[1] criteria are possible from the relationships between the parameters (c, φ, ψ) and (α, β, k), given by:

$$\alpha = \frac{2\sin\varphi}{\sqrt{3}(3 - \sin\varphi)} \tag{A.6}$$

$$\beta = \frac{1}{\sqrt{3}} \tag{A.7}$$

1. DRUCKER _PRAGER model in Cast3m (CEA, 2001)

$$\alpha = \frac{6c\cos\varphi}{\sqrt{3}(3-\sin\varphi)} \tag{A.8}$$

The Drucker-Prager model, calibrated on the Mohr-Coulomb model, is used hereafter in order to numerical difficulties. Given the low permeability of the compressible soil, we assume that the test corresponds to undrained conditions. For this, a Poisson's modulus of $\nu = 0.45$ is adopted. Saturated fine materials in undrained conditions exhibit, for a given consolidation stress, a shear strength related solely to cohesion. The angle of internal friction is therefore taken equal to $\varphi = 0$; the Mohr-Coulomb criterion used in this case is therefore reduced to the Tresca criterion.

Expansion is measured by the dilatancy angle ψ, which reflects the amount of volumetric plastic deformation developed during plasticisation. A value of $\psi = 0°$ corresponds to no change in volume, which is typical for clay soils. The depth-varying cohesion used in the model (shown in orange on the left in Fig. A.4) was calculated from the experimentally calculated shear strength to cone resistance correlation ($S_u/Q_c = 18.5$) for two types of pure kaolinite and 20% and 30% kaolinite-mixtures (ASIRI source report 2.07.3.07 and 2.07.3.08, Fig. A.4).

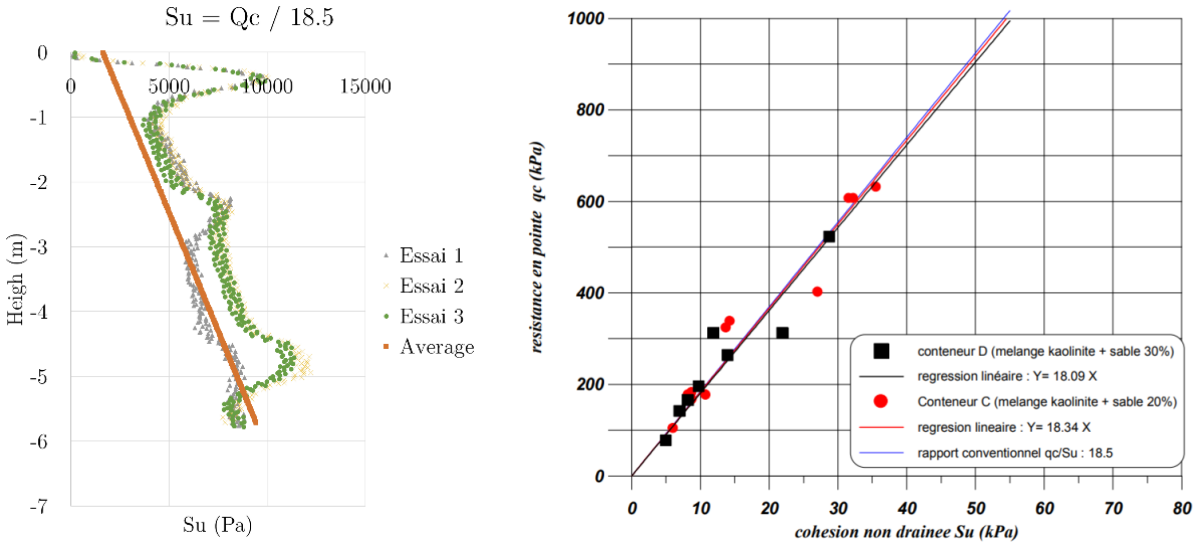

FIGURE A.4 : Left: Su obtained with correlation Su/Qc=18.5. Right: shear strength to cone resistance correlation for two types of kaolinite - sand mix at 20% and 30% (source ASIRI report 2.07.3.08)

The formula proposed by Hardin and Drnevich (1972) is used to estimate the maximum shear profile:

$$G_{\max} = 625\frac{OCR^k}{0.3+0.7e^2}\sqrt{p_a\sigma'_m} \tag{A.9}$$

where OCR is the over-consolidation rate (considered to vary linearly in depth from 2 down to 1 in the compressible layer $z = [0.5 - 6.3]m$, p_a is the atmospheric pressure (~ 100 kPa), σ'_m the mean effective stress (variation in depth calculated from the initial state (Phase 0) and $e = 1.04$ the void index (considered constant). The exponent $k = 0.21$ (considered constant) depends on the plasticity index, estimated to be equal to $Ip = 25\%$ (Khemakhem et al., 2012).

Load Transfer Platform (LTP)

The behaviour of the LTP is again modelled using the Drucker-Prager model calibrated on the Mohr-Coulomb model. The parameters adopted are described in Tab. A.2. An interface between the LTP and the base was also added. This interface consists of a thin layer 1 mm thick with the same properties as the LTP.

Incompressible soil layer

The incompressible soil model is considered to be linear elastic. Its characteristics are described in Tab. A.2.

TABLE A.2 : Parameters used for the soil elastic materials

Parameters	Symbol	Load Transfer Platform	Incompressible soil layer	Unity
Mass Density	ρ	1600	1800	kg/m^3
Young Modulus	E	20.67	421.2	GPa
Poisson Modulus	ν	0.3	0.3	-
Friction angle	φ	38	-	deg
Dilatancy angle	ψ	9	-	deg
Cohesion	c	0	-	kPa

A.3 Results

A.3.1 Calibration

The calculated force on the footing without RI versus the imposed displacement is given in Fig. A.5. A comparison is made with the experimental results.

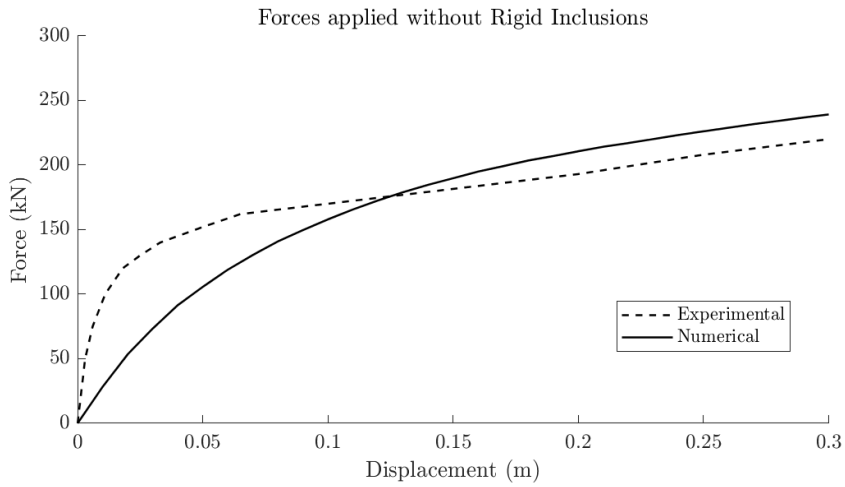

FIGURE A.5 : Force on the footing function of the imposed displacement (no RI, footing 2.53 m x 2.53 m). Experimental vs. numerical results

A.3.2 Configuration A

The calculated force on the footing with RI versus the imposed displacement is given in Fig. A.6.

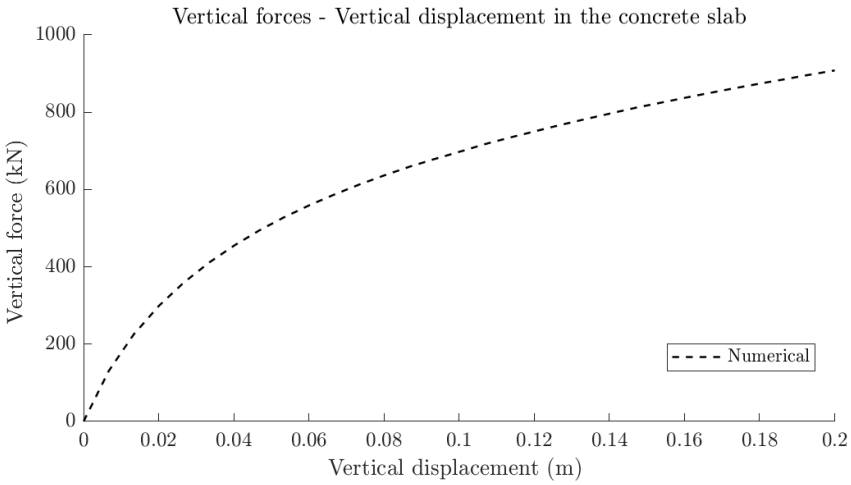

FIGURE A.6 : Force on the footing function of the imposed displacement (case A, footing 2.53 m x 2.53 m; a centre-to-centre distance of RI 1.70 m)

The forces absorbed by the RI are calculated by integrating the vertical stresses σ_{zz} in the section at the head of the RI, see Fig. A.7.

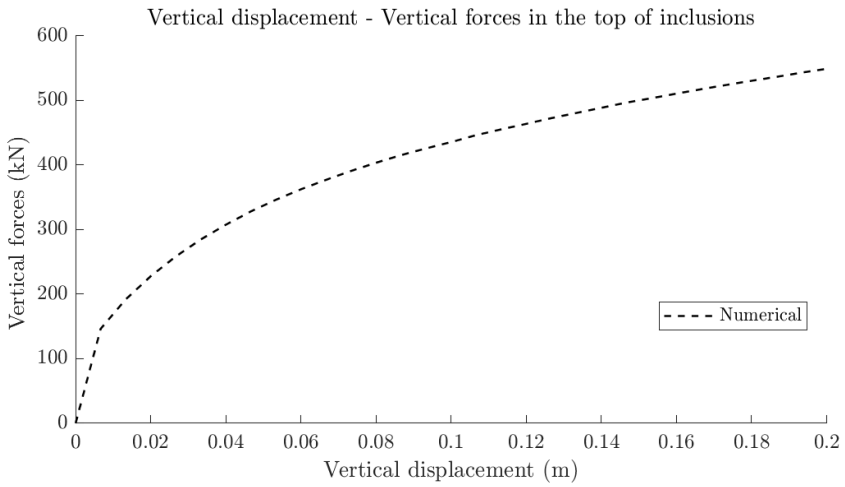

FIGURE A.7 : Vertical force at the head of the RI function of the imposed displacement (case A, footing 2.53 m x 2.53 m, centre-to-centre distance of RI 1.70 m)

A.3.3 Configuration B

The calculated force on the footing with RI with respect to the imposed displacement is given in Fig. A.8. A comparison is made with the experimental results.

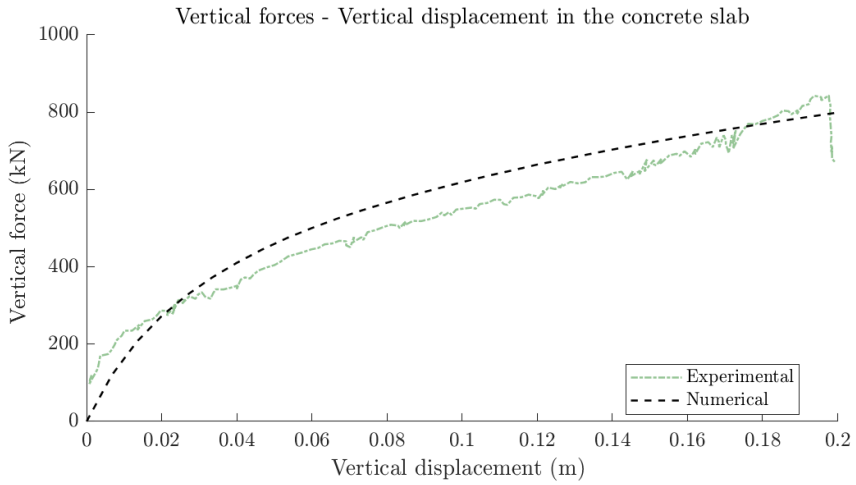

FIGURE A.8 : Force on the footing function of the imposed displacement (case B, footing 2.21 m x 2.21 m, a centre-to-centre distance of RI 1.36 m)

The forces absorbed by the RI are calculated by integrating the vertical stresses σ_{zz} in the section at the head of the RI Fig. A.9.

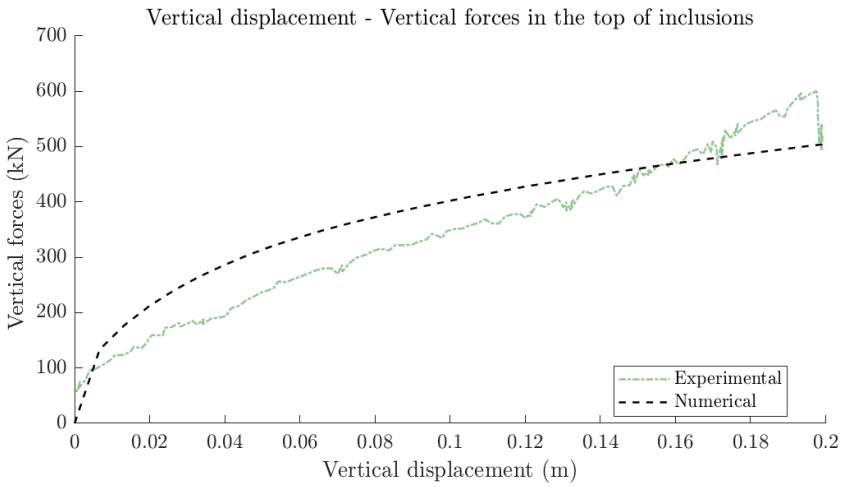

FIGURE A.9 : Vertical force at the head of the RI function of the imposed displacement (case B, footing 2.21 m x 2.21 m, a centre-to-centre distance of RI 1.36 m)

Annexe B

Research report, project ASIRIplus, Benchmark No 2 "*Response*"

B.1 Introduction

This benchmark concerns the prediction of vertical and horizontal load transfers for the case of static loading of an insulated footing on LTP and compressible soil reinforced with four RI. The following sections present only the loading procedure and the results, as the other parameters are described in annexe A.

B.2 Loading procedure

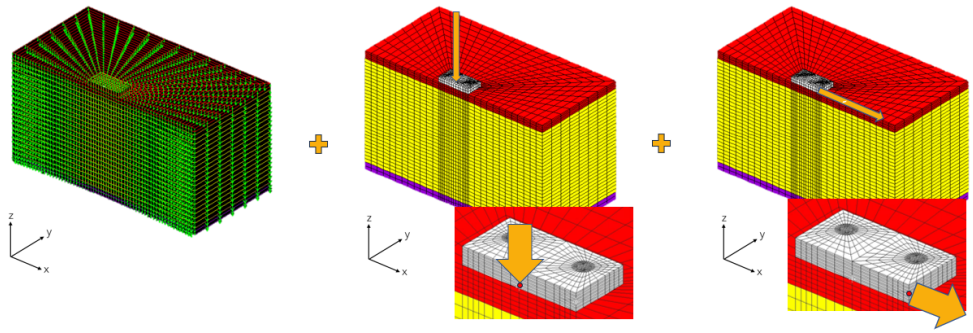

Figure B.1 : Numerical model: loading procedure

In the numerical model, the loading is applied in three phases (Fig. B.1):

- Phase 0: system subjected to its weight
- Phase 1: vertical displacement applied at a point in the middle of the footing

- Phase 2: horizontal displacement of the footing up to 200 mm while the vertical load is maintained at 715 kN. The horizontal load application point is 17.6 cm above the LTP.

B.3 Results

B.3.1 Phase 1: Vertical loading

The calculated vertical force on the footing versus the imposed displacement is given in Fig. B.2. Comparison is made with the experimental results.

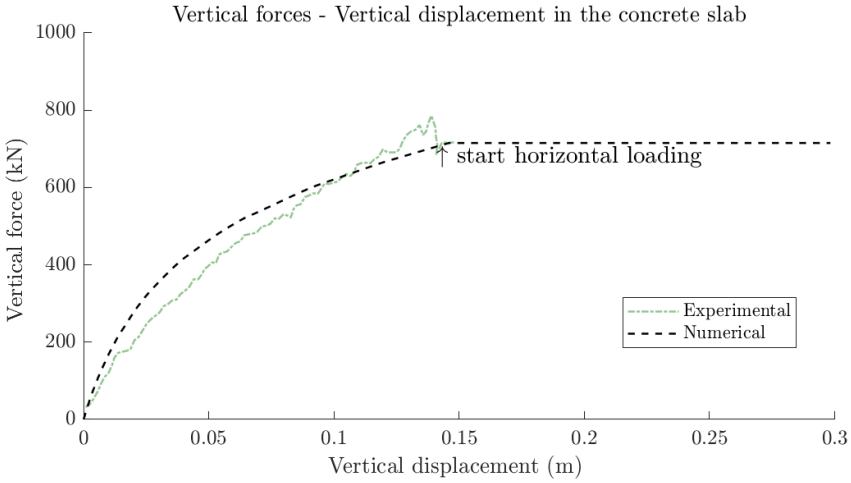

FIGURE B.2 : Force on the footing function of the imposed displacement.

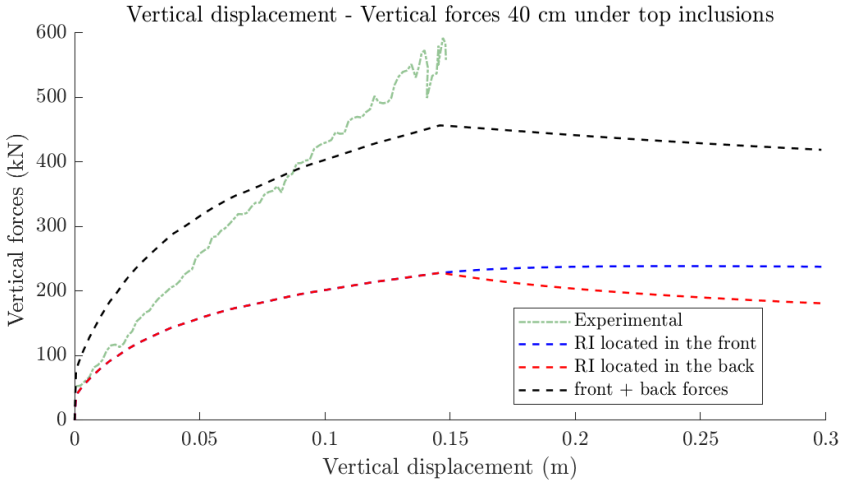

FIGURE B.3 : Vertical force at the head of the RI function of the imposed displacement

The forces taken by the RI are calculated by integrating the vertical stresses σ_{zz} in the section at the head of the RI Fig. B.3.

B.3.2 Phase 2: horizontal loading

The horizontal force on the footing with respect to the imposed displacement is given in Fig. B.4.

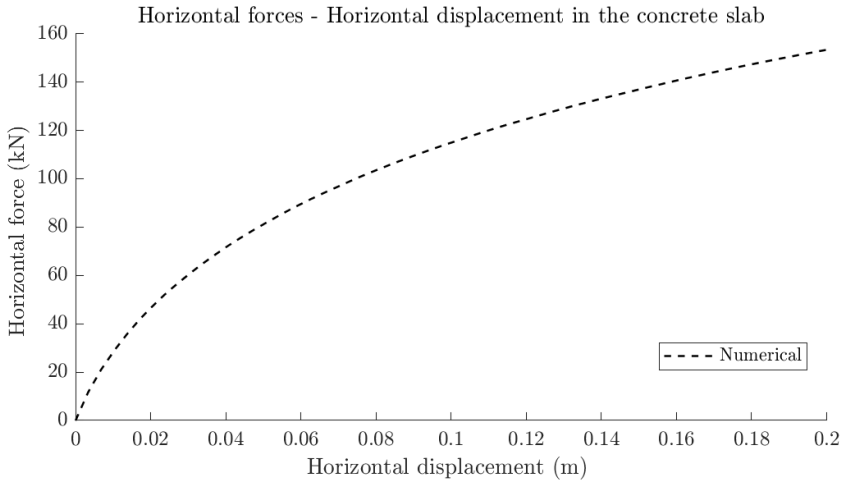

FIGURE B.4 : Horizontal force at the head of the RI function of the imposed horizontal displacement

The vertical displacement at the centre of the footing function of the horizontal displacement is given in Fig. B.5.

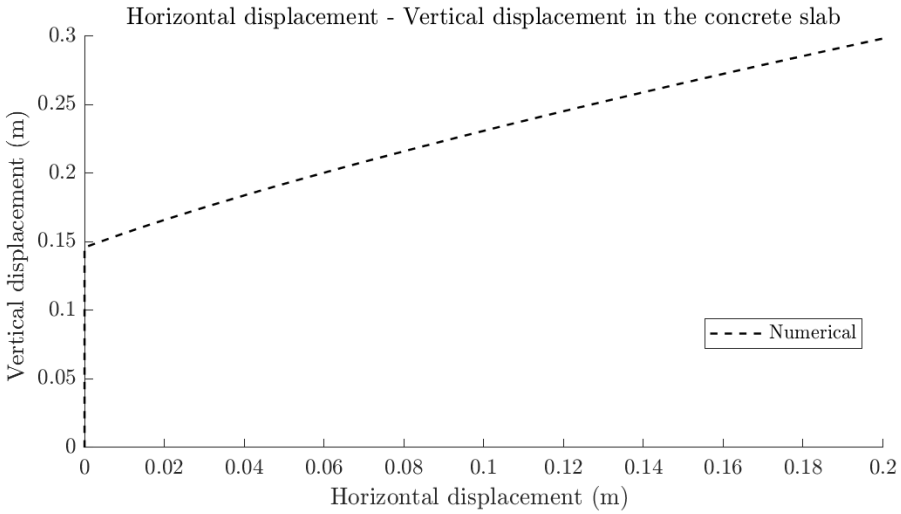

FIGURE B.5 : Vertical displacement at the centre of the footing function of the horizontal displacement

Annexe C

Vertical bearing capacity

This annexe presents the vertical load-bearing capacity calculation, *i.e.*, the maximum vertical load the foundation system can support before reaching a state of failure or excessive deformation. It is calculated hereafter for a weightless footing, for the foundation with and without RI presented in Chapter 2. This is done in order to eliminate the influence of the foundation's weight, which can impact the ultimate maximum vertical force the system can withstand.

A monotonically increasing vertical displacement is numerically applied, and the vertical displacement-load curves are presented in Fig. C.1. The weightless foundation with RI is depicted in grey, while without RI in yellow.

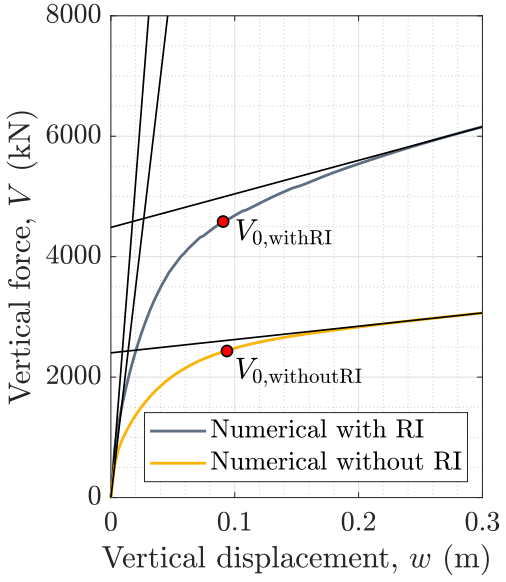

Figure C.1 : Vertical displacement vs vertical force for a foundation with (grey) and without (yellow) RI. The maximal bearing capacity, V_0 (red dots), is calculated using the tangent intersection method Hirany and Kulhawy (1988) (black lines)

Results do not exhibit a sudden failure. The tangent intersection method (Hirany and Kulhawy, 1988) is therefore employed to estimate the maximum vertical bearing capacity, denoted as V_0 (indicated by the red dots). This is done considering the intersection of two

tangents (represented by black lines): the first corresponds to the initial slope, while the second relates to the steepest section of the final part of the curve. The method is applied using MATLAB®. The vertical bearing capacity of the RI foundation is found equal to $V_{0,\text{withRI}}$ of 4593 kN, and for the foundation without RI, $V_{0,\text{withoutRI}} = 2399$ kN.

It is observed that the presence of RI has a minor impact on reducing settlement in the initial elastic linear behaviour regime. The presence of RI however, significantly increase the maximum service load for the same vertical displacement Fig. C.1, showing clearly the beneficial influence of RI.

Comparison with the simplified model MV1

The vertical bearing capacity of the RI foundation found numerically in Fig. C.1 is compared hereafter with the results of the simplified model for a purely vertical loading MV1, from Eq. 1.7, proposed in the ASIRI French recommendations (IREX, 2012).

According to the MV1 model, the limit load for a centred vertical load in the RI foundation is estimated by the interpolation between the case of the footing acting alone and a pile foundation. In our case, the LTP thickness $\mathrm{H_{LTP}}$ is smaller than the footing diameter B. According to Eq. 1.7, the vertical bearing capacity for the RI foundation (Q_{RF}) is then calculated as follows:

$$\begin{aligned} & Q_{\text{RF}} = (1-\Omega)Q_{\text{SF}} + \Omega Q_{\text{pg}} \\ \text{being} \quad & \Omega = \frac{1}{4}(2 - \frac{2 \cdot \mathrm{H_{LTP}}}{B})^2 \end{aligned} \tag{C.1}$$

where Q_{RF} is the vertical bearing capacity of the foundation with RI, Q_{SF} the vertical capacity of the footing acting alone and Q_{pg} the vertical bearing capacity of the group of piles. H_{LTP} is the LTP thickness and B the footing diameter.

The improvement of the vertical bearing capacity due to the presence of the LTP is neglected (IREX, 2012). Considering only the cohesion term, the simplified expression to estimate Q_{SF} is given by:

$$Q_{\text{SF}} = c\,\mathrm{N_c}\,\mathrm{s_c}\,\mathrm{A_{Footing}} \tag{C.2}$$

where $c = s_{\text{u}}$ for a cohesive fine soil in a short-term design, $N_c = \pi + 2$ is the bearing capacity factor for the cohesive term, $\mathrm{s_c}$ is the shape factor and $A_{\text{Footing}} = \pi B^2/4$ is the area of the circular footing. Considering $s_{\text{u,avg}} = 17.15$ kPa, Q_{SF} is found equal to 2990 kN (bigger than the numerical model value $V_{0,\text{withoutRI}} = 2399$ kN).

The bearing capacity of a single inclusion is estimated using the NF P 94-262 (AFNOR,

2013b). It is found equal to 640 kN (since $3b < d$, where b is the RI diameter and d is the center-to-center distance between RI, the group effect can be neglected). Having 7 RI, Q_{pg} is therefore equal to $640 \times 7 = 4480$ kN.

Using Eq. C.1, the estimated vertical bearing capacity of the RI foundation is finally found equal to $Q_{\text{RF}} = 4025$ kN (instead of $V_{0,\text{withRI}}$ of 4593 kN for the numerical model, Fig. C.1). As discussed in Chapter 1, MV1 is conservative as it is based on the assumption that the influence between the different components of the limit load is exclusively related to the efficiency developed by the LTP and controlled by its thickness. One can also observe that the tangent method provides a value close to $V_{0,\text{withRI}}$ of 4593 kN (although for a small vertical displacement of 1.5% w/B), something that demonstrates the efficiency of the approach in determining the vertical bearing capacity of the system.

Annexe D

Settlement efficiency

This annexe explores the influence of various geometric and material parameters on the settlement efficiency. More specifically, we investigate the influence of the coverage area (α), the thickness of the LTP (H_{LTP}) and the LTP's friction angle (φ_{LTP}) of the settlement of a RI foundation when subjected to centrally applied vertical loads.

A monotonically increasing vertical displacement is applied to two models: a RI foundation and a foundation without RI. The settlement efficiency (η_s), defined in Eq. 2.13, is computed for different load levels. Results are then normalised by the maximal vertical force of the foundation without RI ($V_{0,\text{withoutRI}}$) as estimated in Fig. C.1.

Fig. D.1 shows the values of settlement efficiency for different values of α, H_{LTP}, and φ_{LTP}. Results given in Fig. D.1 (a) and Fig. D.1 (b) indicate an increase in efficiency with increasing α and H_{LTP}. Conversely, variations of φ_{LTP} do not alter the efficiency, as illustrated in Fig. D.1 (c). Establishing direct correlations between specific nonlinearities and characteristics with only these first calculations is a challenging and risky task. However the following observations can be made, consistent in all three graphs:

- when $V/V_{0,\text{withoutRI}} \leq 0.1$, a high value of η_s is observed (close to 0.5). This is probably due to the rapid development of forces at the top of the RI;
- when $0.1 < V/V_{0,\text{withoutRI}} \leq 0.2$, as plasticity develops, the response of the RI foundation experiences a gradual stiffness reduction and the settlement efficiency decreases;
- a final increase in efficiency is observed for $0.2 < V/V_{0,\text{withoutRI}} \leq 0.2$. This is probably due to the gradual stiffness reduction of the shallow foundation without RI, as its bearing capacity is reached.
- For small values of H_{LTP} (Fig. D.1 (b)), the footing is already efficiently transmitting forces through the RI. The system is particularly efficient for small values of vertical forces.

The trends above underscore the significance of the foundation design parameters in optimising the load transmission efficiency of the entire system. These findings qualitatively align with previous research (Cao et al., 2004; Tradigo, 2015; Zhang et al., 2022, among others).

TABLE C.1 : Parametric study of the settlement efficiency

Input parameter	Symbol	Reference model	Parameter variations	Unit
Diameter of RI	d	0.6	$0.35, 0.5, 0.6$	(m)
Coverage area	α	2.5	$1.9, 2.92, 4.96$	(%)
LTP thickness	H_{LTP}	1.0	$0.25, 0.5, 0.75, 1.5$	(m)
LTP friction angle	φ_{LTP}	36	$40, 44, 48$	(°)

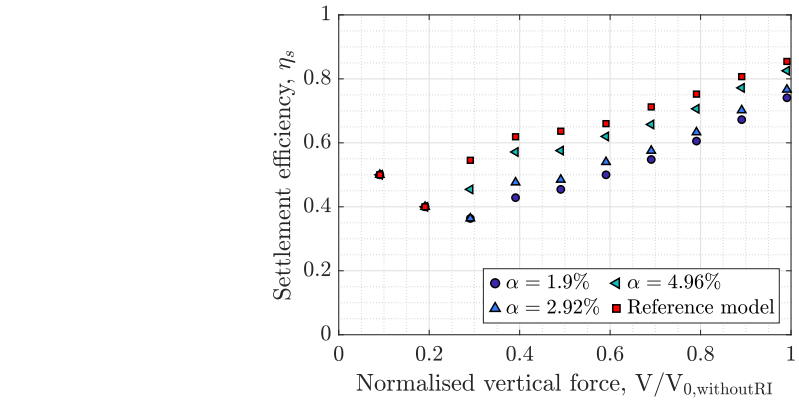

(a)

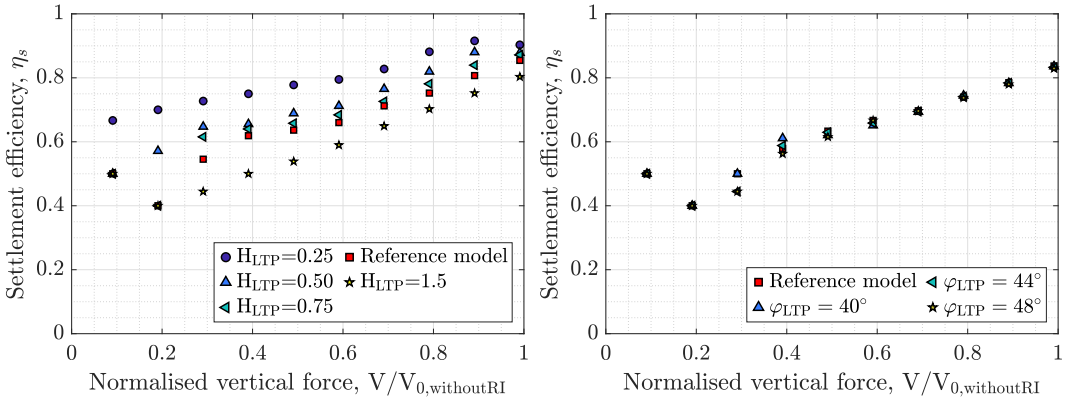

(b) (c)

FIGURE D.1 : Influence of (a) coverage area, φ_{LTP}; (b) LTP thickness,H_{LTP}, and (c) LTP friction angle, φ_{LTP}, on the settlement efficiency, η_s, in the force plane normalised by the maximal vertical force of the model without RI

This page intentionally left blank

Bibliographie

[1] Acar Y, Mollamahmutoglu M (2023) The Effect of Components' Characteristics on Rigid Inclusion System on Soft Soil. Iranian Journal of Science and Technology - Transactions of Civil Engineering 47(2):1125–1137. https://doi.org/10.1007/s40996-022-01026-1

[2] AFNOR (2013a) NF P 94-261, Justification des ouvrages géotechniques - Normes d'application nationale de l'Eurocode 7 - Fondations superficielles, juin 2013, Amendement: NF P 94-261/A1, février 2017. AFNOR

[3] AFNOR (2013b) NF P 94-262, Justification des ouvrages géotechniques - Normes d'application nationale de l'Eurocode 7 - Fondations profondes. AFNOR

[4] Akou Y (1995) Etude expérimentale et modélisation de l'élargissement des remblais sur sols compressibles. PhD thesis, Ecole Nationale des Ponts et Chaussées

[5] Alejano L, Bobet A (2012) Drucker-prager criterion. Rock Mech Rock Eng 45:995–999. https://doi.org/10.1007/s00603-012-0278-2

[6] Amalu PA, Jayalekshmi BR (2022) Analysis of cushion effects in unconnected piled raft foundation. In: Adhikari BR, Kolathayar S (eds) Geohazard Mitigation. Springer Singapore, Singapore, pp 447–458

[7] Anastasopoulos I, Loli M, Gelagoti F, et al. (2012) Nonlinear soil - foundation interaction : numerical analysis. Second international conference on Performance-Based Design in earthquake geotechnical engineering

[8] ANR (2020) Soil improvement by rigid inclusions: Seismic and dynamic loading - ASIRIplus-SDS. https://anr.fr/Project-ANR-19-CE22-0015

[9] ASCE/SEI (2017) Seismic evaluation and retrofit of existing buildings. American Society of Civil Engineers, https://doi.org/10.1061/9780784414859

[10] Baudouin G (2010) Sols renforcés par inclusions rigides : modélisation physique en centrifugeuse de remblais et de dallage. PhD thesis, Université de Nantes. Faculté des sciences et des techniques

[11] Baudouin G, Rosquoët F, Canou J, et al. (2008) Caractérisation mécanique d'un mélange de sables d'hostun. Journées nationales de géotechnique et de géologie de l'ingénieur, Nantes

[12] Bell RW (1991) The analysis of offshore foundations subjected to combined loading - master's thesis. University of Oxford

[13] Benahmed N (2001) Comportement mécanique d'un sable sous cisaillement monotone et cyclique : application aux phénomènes de liquéfaction et mobilité cyclique. PhD thesis, ENPC

[14] Bernuy C, Hor B, Kim S, et al. (2018) LNG tanks on rigid inclusions: Kuwait. Innovative Infrastructure Solutions 3:1–12. https://doi.org/10.1007/S41062-018-0186-8/METRICS

[15] Bigot G, Canepa Y (1988) Fondations de batiments. utilisation des techniques de traitement et d'amelioration des sols. Rapport inteme LPC pp 37–41

[16] Blanc M, Rault G, Thorel L, et al. (2013) Centrifuge investigation of the load transfer mechanism above rigid inclusions. Geotextiles and Geomembranes 36:92–105

[17] Blanc M, Thorel L, Girout R, et al. (2014) Geosynthetic reinforcement of a granular load transfer platform above rigid inclusions: comparison between centrifuge testing and analytical modelling. Geosynthetics International 21(1):37–52. https://doi.org/10.1680/gein.13.00033, URL https://doi.org/10.1680/gein.13.00033

[18] Borel S (2001) Comportement et dimensionnement des fondations mixtes. PhD thesis, Ecole nationale des ponts et chaussées, thèse de doctorat dirigée par Magnan, Jean-Pierre Géotechnique Marne-la-vallée, ENPC 2001

[19] Borja RI (2013) Plasticity. Springer

[20] Bransby MF, Randolph MF (1997) Shallow foundations subject to combined loadings. Proc, 9th Int Conf on Computer Methods and Advances in Geomechanics, Rotterdam, Netherlands: AA Balkema 3:1947–1952

[21] Bransby MF, Randolph MF (1998) Combined loading of skirted foundations. Geotechnique 48:637–655. https://doi.org/10.1680/GEOT.1998.48.5.637

[22] Bransby MF, Yun GJ (2009) The undrained capacity of skirted strip foundations under combined loading. https://doi.org/10.1680/GEOT.2007.00098

[23] Briançon L, Dias D, Simon C (2015) Monitoring and numerical investigation of a rigid inclusions-reinforced industrial building. Canadian Geotechnical Journal 52(10):1592–1604. https://doi.org/10.1139/cgj-2014-0262

[24] Briancon L, Simon B, Thorel L (2020) Le projet ASIRI+ : Amélioration et Renforcement des Sols par Inclusions RIgides. In: JNGG2020 (Journées Nationales de Géotechnique et de Géologie de l'Ingénieur), LYON, France, p 8 p

[25] Briançon L, Kastner R, Simon B, et al. (2004) Etat des connaissances-amélioration des sols par inclusions rigides. Proc, Int Symp on Ground Improvement pp 15–44

[26] Briançon L, Cuira F, Dias D, et al. (2019) Programme de recherche ASIRI+. https://asiriplus.fr/programme-recherche/

[27] Burtin P, Racinais J (2016) Embankment on soft soil reinforced by CMC semi-rigid inclusions for the high-speed railway SEA. Procedia Engineering 143:355–362. https://doi.org/10.1016/J.PROENG.2016.06.045

[28] Buschmeier B, Masse F, Swift S, et al. (2012) Full scale instrumented load test for support of oil tanks on deep soft clay deposits in louisiana using controlled modulus columns

[29] Butterfield R (1980) A simple analysis of the load capacity of rigid footings on granular materials. Journée de Geotechnique, ENTPE, Lyon, France pp 128–137

[30] Butterfield R, Gottardi G (1994) A complete three-dimensional failure envelope for shallow footings on sand. Géotechnique 44(1):181–184. https://doi.org/10.1680/geot.1994.44.1.181

[31] Butterfield R, Houlsby GT, Gottardi G (1997) Standardized sign conventions and notation for generally loaded foundations. Geotechnique 47:1051–1054. https://doi.org/10.1680/GEOT.1997.47.5.1051

[32] Byrne BW (2000) Investigations of suction caissons in dense sand. PhD thesis, University of Oxford, UK

[33] Cao XD, Wong IH, Chang MF (2004) Behavior of model rafts resting on pile-reinforced sand. Journal of Geotechnical and Geoenvironmental Engineering 130(2):129–138. https://doi.org/10.1061/(ASCE)1090-0241(2004)130:2(129)

[34] Cassidy MJ (1999) Non-linear analysis of jack-up structures subjected to random waves. PhD thesis, University of Oxford, UK

[35] CEA (2001) Cast3m. http://www-cast3m.cea.fr/

[36] Chanda D, Nath U, Saha R, et al. (2021) Development of lateral capacity-based envelopes of piled raft foundation under combined v-m-h loading. International Journal of Geomechanics 21(6):04021,075. https://doi.org/10.1061/(ASCE)GM.1943-5622.0002023

[37] Chatzigogos C, Pecker A, Salençon J, et al. (2007) A macro-element for dynamic soil-structure interaction analyses of shallow foundations. 4th International conference on earthquake geotechnical engineering

[38] Chatzigogos CT, Pecker A, Salençon J (2009) Macroelement modeling of shallow foundations. Soil Dynamics and Earthquake Engineering 29:765–781. https://doi.org/10.1016/j.soildyn.2008.08.009

[39] Chernov N (2023) Ellipse Fit (Direct method). MATLAB Central File Exchange, The MathWorks Inc., Natick, Massachusetts, United States

[40] Chevalier B, Villard P, Combe G (2010) Investigation of load-transfer mechanisms in geotechnical earth structures with thin fill platforms reinforced by rigid inclusions. International Journal of Geomechanics 11:239–250. https://doi.org/10.1061/(ASCE)GM.1943-5622.0000083

[41] Combarieu O (1990) Fondations superficielles sur sol ameliore par inclusions rigides verticales. Revue française de Geotechnique

[42] Combault J, Teyssandier JP (2005) The rion-antirion bridge: Concept, design and construction. Structures Congress 2005 1:1–12. https://doi.org/10.1061/40753(171)149

[43] Combault J, Pecker A, Teyssandier JP, et al. (2005) Rion-Antirion Bridge, Greece - Concept, Design, and Construction. Structural Engineering International 15(1):22–22. https://doi.org/10.2749/101686605777963387

[44] Cooke RW (1986) Piled raft foundations on stiff clays—a contribution to design philosophy. Géotechnique 36(2):169–203. https://doi.org/10.1680/geot.1986.36.2.169

[45] Coronado C, Gidwani N (2016) Calculation of dynamic impedance of foundations using finite element procedures. Bechtel Power Corporation Nuclear security & Environmental, San Francisco

[46] Correia A (2011) A pile-head macro-element approach to seismic design of monoshaft-supported bridges. Unpublished PhD thesis) European School for Advanced Studies in Reduction of Seismic Risk (ROSE School), Pavia, Italy

[47] Correia AA, Pecker A (2021) Nonlinear pile-head macro-element for the seismic analysis of structures on flexible piles. Bulletin of Earthquake Engineering 19:1815–1849. https://doi.org/10.1007/s10518-020-01034-4

[48] Correia AA, Pecker A, Kramer SL, et al. (2012) Nonlinear pile-head macro-element model: SSI effects on the seismic response of a monoshaft-supported bridge. 15 WCEE

[49] Cremer C (2001) Modelisation du comportement non lineaire des fondations superficielles sous seisme : macro-element d'interaction sol-structure. PhD thesis, École Normale Supérieure Cachan, Thèse de doctorat dirigée par Mazars, Jacky Sciences et techniques Cachan, Ecole normale supérieure 2001

[50] Crémer C, Pecker A, Davenne L (2001) Cyclic macro-element for soil-structure interaction: material and geometrical non-linearities. International Journal for Numerical and Analytical Methods in Geomechanics 25:1257–1284. https://doi.org/10.1002/NAG.175

[51] Crémer C, Pecker A, Davenne L (2002) Modelling of nonlinear dynamic behaviour of a shallow strip foundation with macro-element. Journal of Earthquake Engineering 6:175–211. https://doi.org/10.1080/13632460209350414

[52] Demkowicz L (1991) A note on symmetry boundary conditions in finite element methods. Applied Mathematics Letters 4(5):27–30. https://doi.org/https://doi.org/10.1016/0893-9659(91)90138-L

[53] di Prisco C, Pisanò F (2014) Numerical modeling and mechanical analysis of an innovative soil anchoring system. Acta Geotechnica 9:1013–1028. https://doi.org/https://doi.org/10.1007/s11440-013-0250-7

[54] Dias D, Simon B (2015) Spread foundations on rigid inclusions subjected to complex loading: Comparison of 3D numerical and simplified analytical modelling. American Journal of Applied Sciences 12:533–541. https://doi.org/10.3844/ajassp.2015.533.541

[55] Diaz-Guzman MA, Manica-Malcom MA, Ovando-S. E, et al. (2021) Respuesta sísmica de sistemas de cimentación a base de inclusiones rígidas. XXX Reunión Nacional de Ingeniería Geotécnica Respuesta sísmica de sistemas de cimentación a base de inclusiones rígidas

[56] Diaz-Segura E (2013) Assessment of the range of variation of n_γ from 60 estimation methods for footings on sand. Canadian Geotechnical Journal 50. https://doi.org/10.1139/cgj-2012-0426

[57] Doulgeroglou AA, Kotronis P, Sciarra G, et al. (2022) 3D interaction diagrams for symmetrically reinforced concrete square sections with various reinforcement ratios. Engineering Structures 262:114,272. https://doi.org/10.1016/j.engstruct.2022.114272

[58] DuMouchel W, O'Brien F (1992) Integrating a robust option into a multiple regression computing environment. Ima Volumes In Mathematics And Its Applications https://doi.org/10.1007/978-1-4613-9154-8_3

[59] EN1998-5 (2004) Eurocode 8. Design of structures for earthquake resistance Part 5: Foundations, retaining structures and geotechnical aspects, volume C. British Standards Institution

[60] Escoffier S, Li Z, Soriano C (2022) Data Report no. 2 ASIRI+ Project amélioration des sols par inclusions rigides: sollicitations dynamiques et sismiques. Tech. rep., Université Gustave Eiffel

[61] Escoffier S, Li Z, Nohra C, et al. (2023) Data Report no. 9 soil-structure interaction: Building over rigid inclusions ASIRI+ Project amélioration des sols par inclusions rigides: sollicitations dynamiques et sismiques. Tech. rep., Université Gustave Eiffel

[62] da Fagundes D, Almeida MSS, Thorel L, et al. (2017) Load transfer mechanism and deformation of reinforced piled embankments. Geotextiles and Geomembranes 45:1–10

[63] Fan Q, Meng X (2011) Failure envelope of pipe pile foundation under combined loading. Advances in Pile Foundations, Geosynthetics, Geoinvestigations, and Foundation Failure Analysis and Repairs, GeoHunan International Conference 2011 June 9-11 pp 109–116. https://doi.org/10.1061/47631(410)13

[64] Filz G, Sloan J, McGuire MP, et al. (2012) Column-Supported Embankments: Settlement and Load Transfer, American Society of Civil Engineers, pp 54–77.

https://doi.org/10.1061/9780784412138.0003, URL https://ascelibrary.org/doi/pdf/10.1061/9780784412138.0003

[65] Filz GM, Sloan JA, McGuire MP, et al. (2019) Settlement and Vertical Load Transfer in Column-Supported Embankments. Journal of Geotechnical and Geoenvironmental Engineering 145(10). https://doi.org/10.1061/(asce)gt.1943-5606.0002130

[66] Fioravante V, Giretti D (2010) Contact versus noncontact piled raft foundations. Canadian Geotechnical Journal 47(11):1271–1287. https://doi.org/10.1139/T10-021

[67] Fitzgibbon A, Pilu M, Fisher RB (1999) Direct least square fitting of ellipses. IEEE Trans Pattern Analysis and Machine Intelligence 21:987–996. https://doi.org/10.1109/34.765658

[68] Fok N, Qiu TZ, de Vincent PP, et al. (2012) A case study of ground improvement using semi-Rigid Inclusions for Breakwater Road Bridge. In: International Conference on Graphics and Interaction, pp 629–643, https://doi.org/10.3850/978-981-07-3559-3_02-0028

[69] Frattini N, Cuira F, Hor B (2017) Simplified approach for the design of rigid inclusions under spread footing using semi-analytical calculations. Proceedings of the 19th International Conference on Soil Mechanics and Geotechnical Engineering pp 737–740

[70] Garnier J (2001) Modèles physiques en géotechnique i - Évolution des techniques expérimentales et des domaines d'application. Revue Française de Géotechnique 97:3–29

[71] Gazetas G (1983) Analysis of machine foundation vibrations: state of the art. International Journal of soil dynamics and earthquake engineering 2(1):2–42

[72] Gazetas G (1991) Formulas and charts for impedances of surface and embedded foundations. Journal of Geotechnical Engineering 117(9):1363–1381. https://doi.org/10.1061/(ASCE)0733-9410(1991)117:9(1363)

[73] Géradin M, Rixen DJ (2014) Mechanical vibrations: theory and application to structural dynamics. John Wiley & Sons

[74] Ghannad M, Ahmadnia A (2006) The effect of soil-structure interaction on inelastic structural demands. European Earthquake Engineering 20(1):23

[75] Girout R, Blanc M, Dias D, et al. (2014) Numerical analysis of a geosynthetic-reinforced piled load transfer platform - validation on centrifuge test. Geotextiles and Geomembranes 42(5):525–539. https://doi.org/10.1016/j.geotexmem.2014.07.012

[76] Gorini DN, Callisto L (2023) A multiaxial inertial macroelement for deep foundations. Computers and Geotechnics 155. https://doi.org/10.1016/j.compgeo.2022.105222

[77] Gottardi G (1992) Modellazione del comportamento di fondazioni superficiali su sabbia soggette a diverse condizioni di carico : dottorato di ricerca in ingegneria geotecnica. Theses, Universita di Padova, Padova

[78] Gottardi G, Butterfield R (1993) On the bearing capacity of surface footings on sand under general planar loads. Soils and Foundations 33(3):68–79. https://doi.org/https://doi.org/10.3208/sandf1972.33.3_68

[79] Gottardi G, Houlsby GT, Butterfield R (1999) Plastic response of circular footings on sand under general planar loading. https://doi.org/10.1680/GEOT.1999.49.4.453

[80] Gourvenec S (2007) Failure envelopes for offshore shallow foundations under general loading. Géotechnique 57(9):715–728

[81] Gourvenec S, Barnett S (2011) Undrained failure envelope for skirted foundations under general loading. Geotechnique 61:263–270. https://doi.org/10.1680/GEOT.9.T.027

[82] Gourvenec S, Randolph M (2003) Effect of strength non-homogeneity on the shape of failure envelopes for combined loading of strip and circular foundations on clay. https://doi.org/10.1680/GEOT.2003.53.6.575

[83] Grange S (2008) Modélisation simplifiée 3D de l'interaction sol-structure: application au génie parasismique. Theses, Institut National Polytechnique de Grenoble - INPG

[84] Grange S, Kotronis P, Mazars J (2008) A macro-element for a circular foundation to simulate 3d soil-structure interaction. International Journal for Numerical and Analytical Methods in Geomechanics 32(10):1205–1227. https://doi.org/https://doi.org/10.1002/nag.664

[85] Grange S, Kotronis P, Mazars J (2009a) A macro-element to simulate 3d soil-structure interaction considering plasticity and uplift. International Journal of Solids and Structures 46(20):3651–3663. https://doi.org/10.1016/j.ijsolstr.2009.06.015

[86] Grange S, Kotronis P, Mazars J (2009b) A macro-element to simulate dynamic soil-structure interaction. Engineering Structures 31(12):3034–3046

[87] Guo X, Nian T, Zhao W, et al. (2022) Centrifuge experiment on the penetration test for evaluating undrained strength of deep-sea surface soils. International Journal of Mining Science and Technology 32(2):363–373. https://doi.org/10.1016/j.ijmst.2021.12.005

[88] Hamdan AJS, Mashhour IM, Akl SA, et al. (2023) Effectiveness of concrete rigid inclusions for coastal reclaimed liquefiable soils. Ain Shams Engineering Journal 14. https://doi.org/10.1016/j.asej.2022.101857

[89] Hamidi B, Masse F, Racinais J, et al. (2016) The boundary between deep foundations and ground improvement. Proceedings of the Institution of Civil Engineers - Geotechnical Engineering 169(2):201–213. https://doi.org/10.1680/jgeen.15.00062

[90] Hansen JB (1970) A revised and extended formula for bearing capacity. Danish Geotechnical Institute, Bull No 28 pp 5–11

[91] Hardin B, Drnevich V (1972) Shear modulus and damping in soils: Design equations and curves. J Soil Mech Found Div 98. https://doi.org/10.1061/JSFEAQ.0001760

[92] Hashemi A, Malushte S, Saini J, et al. (2014) Improved two-step method for seismic analysis of structures. Proceedings of the 10th National Conference in Earthquake Engineering, Earthquake Engineering Research Institute, Anchorage, AK

[93] Hatem A (2009) Comportement en zone sismique des inclusions rigides : Analyse de l'interaction sol-inclusion-matelas de répartition - structure. PhD thesis, Lille 1, thèse de doctorat dirigée par Shahrour, Isam Génie civil Lille 1 2009

[94] Hill R (1950) The mathematical theory of plasticity. Clarendon Press

[95] Hirany A, Kulhawy FH (1988) Conduct and interpretation of load tests on drilled shaft foundations: Volume 1, Detailed guidelines: Final report. Cornell University

[96] Holland P, Welsch RE (1977) Robust regression using iteratively reweighted least-squares. Communications in Statistics-theory and Methods 6:813–827

[97] Houlsby GT, Cassidy MJ (2002) A plasticity model for the behaviour of footings on sand under combined loading. Géotechnique 52:117–129

[98] Ikbarieh A, Izadifar MA, Abu-Farsakh MY, et al. (2023) A parametric study of embankment supported by geosynthetic reinforced load transfer platform and timber piles tip on sand. Transportation Geotechnics 38(November 2022):100,901. https://doi.org/10.1016/j.trgeo.2022.100901

[99] IREX (2012) Institute for Applied Research and Experimentation in Civil Engineering. ASIRi national project: Recommandations pour la conception, le calcul, l'exécution et le contrôle des ouvrages sur sols améliorés par inclusions rigides verticales. Presses des Ponts, ISBN 978-2-85978-462-1

[100] Isorna R, Blanc M, Thorel L, et al. (2017) Axial behaviour of jacket piles for offshore wind turbines. International Journal of Physical Modelling in Geotechnics 17(4):229–245. https://doi.org/10.1680/jphmg.15.00044

[101] Javelaud E, Serratrice JF (2018) La liquéfaction des sols sous l'effet de séismes. Ref : TIP541WEB - "Mécanique des sols et géotechnique" https://doi.org/10.51257/A-V1-C261

[102] Jawad HS, Mashhour IM, Akl SA, et al. (2022) Effectiveness of concrete rigid inclusions for coastal reclaimed liquefiable soils. Ain Shams Engineering Journal https://doi.org/10.1016/J.ASEJ.2022.101857

[103] Jeanjean P, Watson P, Kolk H, et al. (2011) The new API recommended practice for geotechnical engineering: RP 2GEO. In: Frontiers in Offshore Geotechnics II - Proceedings of the 2nd International Symposium on Frontiers in Offshore Geotechnics. CRC Press, pp 903–908

[104] Jenck O, Dias D, Kastner R (2005) Soft ground improvement by vertical rigid piles two-dimensional physical modelling and comparison with current design methods. Soils and Foundations 45(6):15–30. https://doi.org/10.3208/sandf.45.15

[105] Jeremic B, Yang Z, Cheng Z, et al. (2023) Nonlinear Finite Elements: Modeling and Simulation of Earthquakes, Soils, Structures and their Interaction. University of California, Davis, CA, USA and Lawrence Berkeley National Laboratory, Berkeley, CA, USA 1989-2023

[106] Jeremić B, Presig M (2005) Seismic soil foundation structure interaction: Numerical modelling issues. EI Structures Congress, New York, 20-24 April

[107] Jie G, Preisig M, Jeremić B (2007) Dynamic response and soil properties - benefits and detriments of soil foundation structure interaction. American Society of Civil Engineers Geo-Denver 2007 - Denver, Colorado, United States (February 18-21, 2007) pp 1–10. https://doi.org/10.1061/40904(223)10

[108] Jin Z, Yin ZY, Kotronis P, et al. (2019) Advanced numerical modelling of caisson foundations in sand to investigate the failure envelope in the H-M-V space. Ocean Engineering 190. https://doi.org/10.1016/j.oceaneng.2019.106394

[109] Jin Z, Li Z, Yin ZY, et al. (2021) Numerical modeling of soil-pipe interaction of single pipeline at shallow embedment in clay by hypoplastic macroelement. Ocean Engineering p 110017. https://doi.org/10.1016/j.oceaneng.2021.110017

[110] Jue Wang WLDing Zhou, Wang S (2016) Nested lumped-parameter model for foundation with strongly frequency-dependent impedance. Journal of Earthquake Engineering 20(6):975–991. https://doi.org/10.1080/13632469.2015.1109568

[111] Katzenbach R, Arslan U, Moormann C (2000) Piled raft foundation projects in germany. In: Design applications of raft foundations. Thomas Telford Publishing, p 323–391

[112] Kausel E, Whitman RV, Morray JP, et al. (1978) The spring method for embedded foundations. Nuclear Engineering and Design 48(2):377–392. https://doi.org/https://doi.org/10.1016/0029-5493(78)90085-7

[113] Kaynia A, Kausel E (1982) Dynamic stiffness and seismic response of pile groups. NASA STI/Recon Technical Report N pp 16,586–

[114] Khemakhem M (2012) Etude experimentale de la réponse aux charges latérales monotones et cycliques d'un pieu fore dans l'argile. PhD thesis, Université de Nantes

[115] Khemakhem M, Chenaf N, Garnier J, et al. (2012) Development of degradation laws for describing the cyclic lateral response of piles in clay. In: SUT Offshore Site Investigation and Geotechnics, SUT, pp SUT–OSIG

[116] Khosravikia F, Mahsuli M, Ghannad MA (2018) Soil-structure interaction in seismic design code: Risk-based evaluation. ASCE-ASME Journal of Risk and Uncertainty in Engineering Systems, Part A: Civil Engineering 4(4):04018,033. https://doi.org/10.1061/AJRUA6.0000984

[117] Ko J, Seo H, Lee JK (2022) Failure envelopes for circular foundations on two-layered clay under combined loading. International Journal of Geomechanics 22(7):04022,085. https://doi.org/10.1061/(ASCE)GM.1943-5622.0002395

[118] Kramer S (1996) Geotechnical earthquake engineering. Prentice Hall

[119] Ladd CC, Foott R (1974) New design procedure for stability of soft clays. Journal of Geotechnical and Geoenvironmental Engineering 100

[120] Lai HJ, Zheng JJ, Zhang RJ, et al. (2018) Classification and characteristics of soil arching structures in pile-supported embankments. Computers and Geotechnics 98(November 2017):153–171. https://doi.org/10.1016/j.compgeo.2018.02.007

[121] Larisch M, Kelly R, Muttuvel T (2015) Chapter 21 - improvement of soft soil formations by drilled displacement columns. In: Indraratna B, Chu J, Rujikiatkamjorn C (eds) Ground Improvement Case Histories. Butterworth-Heinemann, p 573–622, https://doi.org/https://doi.org/10.1016/B978-0-08-100192-9.00021-1

[122] Lau BH (2015) Cyclic behaviour of monopile foundations for offshore wind turbines in clay. PhD thesis, University of Cambridge, https://doi.org/10.17863/CAM.14093

[123] Le Cor T, Breugnot A, Ginisty G, et al. (2022) Travaux de renforcement du Quai Joannès Couvert au Havre – Renforcement par inclusions rigides. In: 11èmes journées nationales de géotechnique et de géologie de l'ingénieur, Institut National des Sciences Appliquées de Lyon [INSA Lyon], CFMS, CFMR, CFGI, Lyon, France

[124] Le Hello B, Villard P (2009) Embankments reinforced by piles and geosynthetics-Numerical and experimental studies dealing with the transfer of load on the soil embankment. Engineering Geology 106(1-2):78–91. https://doi.org/10.1016/j.enggeo.2009.03.001

[125] Le Pape Y, Sieffert JG, Harlicot P (1999) Analyse non linéaire par macro-éléments du comportement des fondations superficielles sous action sismique. 5ème Colloque National AFPS Cachan, France, 19 - 21 Octobre pp 207–214

[126] Lee J, Park D, Choi K (2014) Analysis of load sharing behavior for piled rafts using normalized load response model. Computers and Geotechnics 57:65–74. https://doi.org/https://doi.org/10.1016/j.compgeo.2014.01.003

[127] Lesny K (2009) Safety of shallow foundations - Limit State Design according to Eurocode 7 vs. alternative design concepts. https://doi.org/10.1080/17499510802552877

[128] Li Z (2014) Etude expérimentale et numérique de fondations profondes sous sollicitations sismiques : pieux verticaux et pieux inclinés. PhD thesis, École Centrale de Nantes, thèse de doctorat dirigée par Kotronis, Panagiotis Génie civil Ecole Centrale de Nantes 2014

[129] Li Z, Kotronis P, Escoffier S (2014) Numerical study of the 3D failure envelope of a single pile in sand. Computers and Geotechnics 62. https://doi.org/10.1016/j.compgeo.2014.06.004Ãŕ

[130] Li Z, Kotronis P, Escoffier S, et al. (2015) A hypoplastic macroelement for single vertical piles in sand subject to three-dimensional loading conditions. Acta Geotechnica 11. https://doi.org/10.1007/s11440-015-0415-7

[131] Li Z, Kotronis P, Escoffier S, et al. (2018) A hypoplastic macroelement formulation for single batter piles in sand. International Journal for Numerical and Analytical Methods in Geomechanics 42(12):1346–1365. https://doi.org/https://doi.org/10.1002/nag.2794, https://arxiv.org/abs/https://onlinelibrary.wiley.com/doi/pdf/10.1002/nag.2794

[132] Liang FY, Chen LZ, Shi XG (2003) Numerical analysis of composite piled raft with cushion subjected to vertical load. Computers and Geotechnics 30(6):443–453. https://doi.org/10.1016/S0266-352X(03)00057-0

[133] Liu J, Yuan Z, Zhang K (1985) Cap-pile-soil interaction of bored pile groups. In: International conference on soil mechanics and foundation engineering. 11, pp 1433–1436

[134] Long PD (1993) Footings with settlement-reducing piles in non-cohesive soil. PhD thesis, Chalmers University of Technology Gothenburg, Sweden

[135] Loukidis D, Salgado R (2009) Bearing capacity of strip and circular footings in sand using finite elements. Computers and Geotechnics 36:871–879. https://doi.org/10.1016/J.COMPGEO.2009.01.012

[136] Loukidis D, Chakraborty T, Salgado R (2008) Bearing capacity of strip footings on purely frictional soil under eccentric and inclined loads. Canadian Geotechnical Journal 45:768–787. https://doi.org/10.1139/T08-015

[137] Low BK, Tang SK, Choa V (1994) Arching in piled embankments. Journal of Geotechnical Engineering 120(11):1917–1938. https://doi.org/10.1061/(ASCE)0733-9410(1994)120:11(1917)

[138] López-Jiménez GA (2019) Static and Dynamic behaviour of pile supported structures in soft soil. Theses, Université Grenoble Alpes

[139] López-Jiménez GA, Dias D (2022) Dynamic soil-structure interaction effects in buildings founded on vertical reinforcement elements. CivilEng 3:573–593. https://doi.org/10.3390/civileng3030034

[140] López-Jiménez GA, Dias D, Jenck O (2019a) Effect of layered liquefiable deposits on the seismic response of soil-foundations-structure systems. Soil Dynamics and Earthquake Engineering 124:1–15. https://doi.org/10.1016/j.soildyn.2019.05.026

[141] López-Jiménez GA, Dias D, Jenck O (2019b) Effect of the soil-pile-structure interaction in seismic analysis: case of liquefiable soils. Acta Geotechnica 14:1509–1525. https://doi.org/10.1007/s11440-018-0746-2

[142] Malcom MAM (2013) Dynamic behavior of rigid inclusions. Master thesis

[143] Malekkhani M, Bazaz J (2021) An analytical model to study the behavior of non-connected piled rafts with granular cushion subjected to vertical load. Int J Civ Eng 19:941–956. https://doi.org/10.1007/s40999-021-00611-1

[144] Mandolini A, Di Laora R, Mascarucci Y (2013) Rational design of piled raft. Procedia Engineering 57:45–52. https://doi.org/https://doi.org/10.1016/j.proeng.2013.04.008, modern Building Materials, Structures and Techniques

[145] Martin CM (1994) Physical and numerical modelling of offshore foundations under combined loads. PhD thesis, Oxford University, UK

[146] Martin CM, Houlsby GT (2000) Combined loading of spudcan foundations on clay: laboratory tests. https://doi.org/10.1680/GEOT.2000.50.4.325

[147] Mayoral J, Romo M, Cirion A, et al. (2006) Effect of layered clay deposits on the seismic behavior of a rigid inclusion. Proceedings of the symposium on rigid inclusions in difficult subsoil conditions pp 11–12

[148] McKay MD, Beckman RJ, Conover WJ (1979) Comparison of three methods for selecting values of input variables in the analysis of output from a computer code. Technometrics 21:239–245. https://doi.org/10.1080/00401706.1979.10489755

[149] Mehravar M, Harireche O, Faramarzi A (2016) Evaluation of undrained failure envelopes of caisson foundations under combined loading. Applied Ocean Research 59:129–137. https://doi.org/10.1016/j.apor.2016.05.001

[150] Meyerhof G (1953) The bearing capacity of foundations under eccentric and inclined loads. Proc of 3rd ICSMFE 1:440–445

[151] Muhammed RD (2015) Etude en chambre d'étalonnage du frottement sol-pieu sous grands nombres de cycles. Application au calcul des fondations profondes dans les sols fins saturés. Theses, Université Pierre et Marie Curie - Paris VI

[152] Mylonakis G, Gazetas G (2000) Seismic soil-structure interaction: Beneficial or detrimental? Journal of Earthquake Engineering 4(3):277–301. https://doi.org/10.1080/13632460009350372

[153] Ángel Mánica Malcom M, Ovando-Shelley E, Jaramillo EB (2015) Numerical study of the seismic behavior of rigid inclusions in soft mexico city clay. Journal of Earthquake Engineering 20:447–475. https://doi.org/10.1080/13632469.2015.1085462

[154] Nadimi S, Fonseca J, Barreto D, et al. (2016) A new approach to investigate the particle size effects in centrifuge modelling. EUROFUGE 2016 (Nantes, France) 1

[155] Neagoe IV (2013) Soft soils reinforced by rigid vertical inclusions. Constructii: Journal of Civil Engineering Research 14:48–55

[156] Niemunis A, Herle I (1997) Hypoplastic model for cohesionless soils with elastic strain range. Mechanics of Cohesive-frictional Materials 2(4):279–299. https://doi.org/https://doi.org/10.1002/(SICI)1099-1484(199710)2:4<279::AID-CFM29>3.0.CO;2-8

[157] Nova R, Montrasio L (1991) Settlements of shallow foundations on sand. Géotechnique 41:243–256

[158] Ohmachi T, Kawamura M, Yasuda S, et al. (1988) Damage due to the 1985 Mexico earthquake and the ground conditions. SOILS AND FOUNDATIONS 28(3):149–159. https://doi.org/10.3208/sandf1972.28.3_149

[159] Ohsaki Y (1966) Niigata earthquakes, 1964 building damage and soil condition. Soils and Foundations 6(2):14–37. https://doi.org/https://doi.org/10.3208/sandf1960.6.2_14

[160] Okyay US, Dias D, Thorel L, et al. (2014) Centrifuge modeling of a pile-supported granular earth-platform. Journal of Geotechnical and Geoenvironmental Engineering 140(2):04013,015. https://doi.org/10.1061/(ASCE)GT.1943-5606.0001004

[161] Ovesen NK (1979) The scaling law relationship. Proc, 7th European Conf in Soil Mechanics and Foundation Engineering 4:319–323

[162] Paikowsky SG, Canniff MC, Lesny K, et al. (eds) (2010) Report 651: LRFD Design and Construction of Shallow Foundations for Highway Bridge Structures. National Cooperative Highway Research Program. Transportation Research Board. National Academies Press, https://doi.org/10.17226/14381

[163] Paolucci R, Pecker A (1997) Seismic bearing capacity of shallow strip foundations on dry soils. Soils and Foundations 37:95–105. https://doi.org/10.3208/SANDF.37.3_95

[164] Pecker A (2023) Interrelationships between practice, standardisation and innovation in geotechnical earthquake engineering. Bulletin of Earthquake Engineering 21(6):3091–3132. https://doi.org/10.1007/s10518-023-01669-z

[165] Pecker A, Teyssandier J (1998) Seismic desing for the foundations of the Rion Antirion bridge. Proceedings of the Institution of Civil Engineers - Geotechnical Engineering 131(1):4–11. https://doi.org/10.1680/igeng.1998.30001

[166] Pecker A, Paolucci R, Chatzigogos C, et al. (2014) The role of non-linear dynamic soil-foundation interaction on the seismic response of structures. Bulletin of Earthquake Engineering 12(3):1157–1176. https://doi.org/10.1007/s10518-013-9457-0

[167] Perez-Herreros J (2020) Dynamic soil-structure interaction of pile foundations : experimental and numerical study. PhD thesis, École Centrale de Nantes

[168] Pham HV, Briançon L, Dias D, et al. (2019) Investigation of behavior of footings over rigid inclusion-reinforced soft soil: Experimental and numerical approaches. Canadian Geotechnical Journal 56(12):1940–1952. https://doi.org/10.1139/cgj-2018-0495

[169] Pitilakis D, Dietz M, Muir Wood D, et al. (2008) Numerical simulation of dynamic soil-structure interaction in shaking table testing. Soil Dynamics and Earthquake Engineering 28(6):453–467. https://doi.org/10.1016/j.soildyn.2007.07.011

[170] Plumelle C (1985) Renforcement d'un sol lache par inclusions de micropieux. Revue française de geotechnique 30:47–57

[171] Poulos GS (2001) Method of analysis of piled raft foundations. a report prepared on behalf of Technical Committee TC18 on pile foundations. International Society of Soil Mechanics and Geotechnical Engineering

[172] Poulos H (2000) Practical design procedures for piled raft foundations. Design applications of raft foundations pp 425–467

[173] Prandtl L (1920) Uber die harte plastischer korper. Nachr Ges Wissensch, Gottingen, math-phys Klasse, 1920 pp 74–85

[174] Prevost J (1978) Anisotropic undrained stress-strain behavior of clays. ASCE J Geotech Eng Div 104(8):1075–1090

[175] Rangel J, Gomez-Bernal A, González J, et al. (2008) Dynamic response of soft soil deposits improved with rigid inclusions. The 14th World Conference on Earthquake Engineering October 12-17, 2008, Beijing, China

[176] Roscoe K (1956) The stability of short pier foundations in sand. British Welding J pp 343–354

[177] Saitoh M (2007) Simple model of frequency-dependent impedance functions in soil-structure interaction using frequency-independent elements. Journal of Engineering Mechanics 133(10):1101–1114

[178] Saitoh M (2012) On the performance of lumped parameter models with gyro-mass elements for the impedance function of a pile-group supporting a single-degree-of-freedom system. Earthquake engineering & structural dynamics 41(4):623–641

[179] Sakellariadis L (2021) Physical and numerical modelling of pile foundations under combined loading. PhD thesis, ETH Zurich, https://doi.org/10.3929/ETHZ-B-000515693

[180] Salciarini D, Tamagnini C (2009) A hypoplastic macroelement model for shallow foundations under monotonic and cyclic loads. Acta Geotechnica 4:163–176. https://doi.org/10.1007/s11440-009-0087-2

[181] Salencon J (1990) Introduction to the yield design theory and its applications to soil mechanics. European Journal of Mechanics, A/Solids 9(5):477–500

[182] Salençon J, Pecker A, Ukritchon B, et al. (1999) Undrained limit analyses for combined loading of strip footings on clay. Journal of Geotechnical and Geoenvironmental Engineering 125(11):1028–1029. https://doi.org/10.1061/(ASCE)1090-0241(1999)125:11(1028.2)

[183] de Sanctis L, Mandolini A (2006) Bearing capacity of piled rafts on soft clay soils. Journal of Geotechnical and Geoenvironmental Engineering 132. https://doi.org/10.1061/(ASCE)1090-0241(2006)132:12(1600)

[184] Sawwaf ME (2010) Experimental study of eccentrically loaded raft with connected and unconnected short piles. Journal of Geotechnical and Geoenvironmental Engineering 136:1394–1402. https://doi.org/10.1061/(asce)gt.1943-5606.0000341

[185] Schofield A, Wroth P (1968) Critical State Soil Mechanics. European civil engineering series, McGraw-Hill

[186] Schotman G (1989) The effects of displacements on the stability of jackup spud-can foundations. OTC Offshore Technology Conference All Days:OTC–6026–MS. https://doi.org/10.4043/6026-MS, URL https://onepetro.org/OTCONF/proceedings-pdf/89OTC/All-89OTC/OTC-6026-MS/2016459/otc-6026-ms.pdf

[187] Schotman G, Stork F (1987) Pipe-soil interaction: A model for laterally loaded pipelines in clay. OTC Offshore Technology Conference All Days:OTC–5588–MS. https://doi.org/10.4043/5588-MS, URL https://onepetro.org/OTCONF/proceedings-pdf/87OTC/All-87OTC/OTC-5588-MS/2017577/otc-5588-ms.pdf

[188] Shen Y, Pérez-Herreros J, Cuira F, et al. (2022a) Interaction cinématique sol-structure d'un massif renforcé par inclusions rigides sous séisme. 11èmes journées nationales de géotechnique et de géologie de l'ingénieur, Institut National des Sciences Appliquées de Lyon [INSA Lyon], CFMS, CFMR, CFGI

[189] Shen Y, Pérez-Herreros J, Cuira F, et al. (2022b) Interaction inertielle sol-structure d'un massif renforcé par inclusions rigides. 11èmes journées nationales de géotechnique et de géologie de l'ingénieur

[190] Shen Z, Bie S, Guo L (2017) Undrained capacity of a surface circular foundation under fully three-dimensional loading. Computers and Geotechnics 92:57–67. https://doi.org/https://doi.org/10.1016/j.compgeo.2017.07.018

[191] Sieffert JG, Bay-Gress C, Houlsby GT, et al. (2001) Discussion: Comparison of european bearing capacity calculation methods for shallow foundations. Proceedings of the Institution of Civil Engineers - Geotechnical Engineering 149:63–64. https://doi.org/10.1680/GENG.2001.149.1.63

[192] da Silva AP, Diambra A, Karamitros D (2019) Macro-element modelling of suction-embedded plate anchors for floating offshore structures. E3S Web of Conferences 92. https://doi.org/10.1051/E3SCONF/20199216009

[193] Simon B (2012) General report S5 Rigid Inclusions and Stone Columns. ISSMGE - TC 211 International Symposium on Ground Improvement IS-GI Brussels 1

[194] Skempton A (1948) The $\varphi = 0$ analysis of stability and its theoretical basis. Proceedings pp 72–77

[195] Stein M (1987) Large sample properties of simulations using latin hypercube sampling. Technometrics 29(2):143–151. https://doi.org/10.1080/00401706.1987.10488205

[196] Suryasentana SK, Dunne HP, Martin CM, et al. (2020) Assessment of numerical procedures for determining shallow foundation failure envelopes. Geotechnique 70:60–70. https://doi.org/10.1680/JGEOT.18.P.055

[197] Sánchez-Sesma FJ, Chávez-Pérez S, Suárez M, et al. (1988) The mexico earthquake of september 19, 1985—on the seismic response of the valley of mexico. Earthquake Spectra https://doi.org/10.1193/1.1585491

[198] Taiebat HA, Carter JP (2000) Numerical studies of the bearing capacity of shallow foundations on cohesive soil subjected to combined loading. Géotechnique 50(4):409–418. https://doi.org/10.1680/geot.2000.50.4.409

[199] Taiebat HA, Carter JP (2002) Bearing capacity of strip and circular foundations on undrained clay subjected to eccentric loads. Geotechnique 52:61–64. https://doi.org/10.1680/geot.2002.52.1.61

[200] Tan F (1990) Centrifuge and theoretical modelling of conical footings on sand. PhD thesis, University of Cambridge, Cambridge, UK

[201] Taylor D (1948) Fundamentals of Soil Mechanics. J. Wiley

[202] Terzaghi K (1943a) Arching in Ideal Soils, John Wiley & Sons, Ltd, chap 5, pp 66–76. https://doi.org/https://doi.org/10.1002/9780470172766.ch5, URL https://onlinelibrary.wiley.com/doi/pdf/10.1002/9780470172766.ch5

[203] Terzaghi K (1943b) Bearing Capacity, John Wiley & Sons, Ltd, chap 8, pp 118–143. https://doi.org/https://doi.org/10.1002/9780470172766.ch8, URL https://onlinelibrary.wiley.com/doi/pdf/10.1002/9780470172766.ch8

[204] Teyssandier JP, Combault J, Morand P (2003) The rion-antirion bridge, design and construction. Structures Congress 2005: Metropolis and Beyond https://doi.org/10.1061/40753(171)149

[205] Tian Y, Zheng T, Zhou T, et al. (2016) A new method to investigate the failure envelopes of offshore foundations. Proceedings of the International Conference on Offshore Mechanics and Arctic Engineering - OMAE 1. https://doi.org/10.1115/OMAE2016-54513

[206] Ticof J (1978) Surface footings on sand under general planar loads. PhD thesis, University of Southampton

[207] Tistel J, Grimstad G, Eiksund G (2020) A macro model for shallow foundations on granular soils describing non-linear foundation behavior. Computers and Structures 232:105,816. https://doi.org/https://doi.org/10.1016/j.compstruc.2017.07.018, mechanics and Modelling of Materials and Structures

[208] Tradigo F (2015) Geotechnical and modeling issues in the design of settlement reducing piles for high-rise buildings. PhD thesis, Politecnico di Milano

[209] Tradigo F, Pisanò F, di Prisco C, et al. (2015) Non-linear soil-structure interaction in disconnected piled raft foundations. Computers and Geotechnics 63:121–134. https://doi.org/10.1016/j.compgeo.2014.08.014

[210] Ukritchon B, Whittle AJ, Sloan SW (1998) Undrained limit analyses for combined loading of strip footings on clay. Journal of Geotechnical and Geoenvironmental Engineering 124(3):265–276. https://doi.org/10.1061/(ASCE)1090-0241(1998)124:3(265)

[211] Van Baars S (2014) The inclination and shape factors for the bearing capacity of footings. Soils and Foundations 54(5):985–992. https://doi.org/10.1016/j.sandf.2014.09.004

[212] Veletsos S, Verbic B (1974) Dynamics of elastic and yielding structure-foundation systems. World Conference on Earthquake Engineering, Rom 5

[213] Vesic AS (1973) Analysis of ultimate loads of shallow foundations. Journal of the Soil Mechanics and Foundations Division 99:45–73. https://doi.org/10.1061/JSFEAQ.0001846

[214] Vulpe C, Gourvenec S, Power M (2015) A generalised failure envelope for undrained capacity of circular shallow foundations under general loading. https://doi.org/10.1680/GEOLETT.14.00010

[215] Wang D, Sánchez M, Briaud JL (2019) Numerical study on the effect of rigid inclusions on existing railroads. International Journal for Numerical and Analytical Methods in Geomechanics 43(18):2772–2796. https://doi.org/10.1002/nag.3001

[216] Wang Y (2021) A macro-element model for spudcan foundations in clay overlying sand. PhD thesis, University of Western Australia

[217] Wolf JP (1989) Soil-structure-interaction analysis in time domain. Nuclear Engineering and Design 111(3):381–393

[218] Xu R, Fatahi B (2018) Geosynthetic-reinforced cushioned piles with controlled rocking for seismic safeguarding. Geosynthetics International 25(6):561–581. https://doi.org/10.1680/jgein.18.00018

[219] Zhang J, Jenck O, Dias D (2022) 3D numerical analysis of a single footing on soft soil reinforced by rigid inclusions. International Journal of Geomechanics 22:04022,113. https://doi.org/10.1061/(ASCE)GM.1943-5622.0002412

[220] Zhu Xj, Fei K, Wang Sw (2018) Horizontal loading tests on disconnected piled rafts and a simplified method to evaluate the horizontal bearing capacity. Advances in Civil Engineering, Article ID 3956509 2018:12. https://doi.org/10.1155/2018/3956509

COLLEGE SCIENCES
DOCTORAL DE L'INGENIERIE
PAYS DE LA LOIRE ET DES SYSTEMES

CENTRALE NANTES

Titre : Modélisation numérique des fondations avec des inclusions rigides sous sollicitations sismiques

Mot clés : Inclusions rigides ; modélisation par macro-éléments ; enveloppe de rupture

Résumé : Les inclusions rigides (IR) sont l'une des techniques d'amélioration des sols disponibles pour les structures fondées sur des sols compressibles. Outre les avantages évidents de la réduction des tassements et de l'amélioration de la capacité portante du sol, la conception appropriée des fondations sur inclusions rigides réduit le risque d'effondrement, renforce la stabilité de la fondation et améliore la réponse structurale. L'objectif principal de cette thèse est de développer un outil numérique simplifié, basé sur l'approche du macro-élément (ME), pour simuler le comportement non linéaire des fondations sur inclusions rigides soumises à des charges statiques et sismiques. Un modèle de méthode des éléments finis (MEF) tridimensionnel est d'abord validé par rapport à de nouvelles données expérimentales, puis utilisé pour définir l'enveloppe de rupture de la fondation sur IR. Cette dernière définit l'espace sûr autorisé, c'est-à-dire les forces limites que la fondation peut supporter sous des charges combinées. Une formule analytique originale est fournie pour l'enveloppe de rupture et un ME basé sur la plasticité est proposé, où le comportement global de la fondation et du sol environnant est regroupé dans une équation constitutive unique reliant l'évolution des forces généralisées et des déplacements. La calibration et la validation basés sur des analyses FEM et des résultats expérimentaux de tests centrifuges dynamiques sont finalement présentés. Les résultats prouvent que le nouveau ME est un outil numérique simplifié précis et robuste pour prendre en compte l'interaction sol-structure dans le cas des fondations sur IR.

Title: Numerical modelling of rigid inclusions foundations subjected to seismic loading

Keywords: Rigid inclusions; macroelement modelling; failure envelope

Abstract: Rigid inclusions (RI) are one of the available soil improvement techniques for structures founded on compressible soils. Apart from the obvious advantages of reducing settlement and improving the soil-bearing capacity, proper design of RI foundations reduces the collapse risk, enhances the foundation's stability and improves the structural response. The main objective of this thesis is to develop a simplified numerical tool, based on the macroelement (ME) approach, to simulate the non-linear behavior of RI foundations subjected to static and seismic loadings. A 3D finite element method (FEM) model is first validated against novel experimental data and then used to identify the RI foundation's failure envelope. This latter defines the allowable safe space, i.e., the limit forces that the foundation can endure under combined loadings. An original analytical formula is provided for the failure envelop and a novel plasticity-based ME is proposed where the global behaviour of the foundation and the surrounding soil is lumped into a single constitutive equation relating the evolution of generalized forces and displacements. Calibration and validation based on FEM analyses and experimental results on dynamic centrifuge tests are finally presented. Results prove that the novel ME is an accurate and robust simplified numerical tool to account for soil-structure interaction for the case of RI foundations.